Organic/Inorganic Hybrid Nanostructures for Chemical Plasmonic Sensors

A Dissertation

Presented to

The Academic Faculty

by

Sehoon Chang

In Partial Fulfillment

of the Requirements for the Degree

Doctor of Philosophy in the

School of Materials Science and Engineering

Georgia Institute of Technology

May, 2011

Organic/Inorganic Hybrid Nanostructures for Chemical Plasmonic Sensors

Approved by:

Dr. Vladimir V. Tsukruk, Advisor
School of Materials Science and Engineering
Georgia Institute of Technology

Dr. Mostafa A. El-Sayed
School of Chemistry and Biochemistry
Georgia Institute of Technology

Dr. Satish Kumar
School of Materials Science and Engineering
Georgia Institute of Technology

Dr. Valeria Milam
School of Materials Science and Engineering
Georgia Institute of Technology

Dr. Yonathan Thio
School of Materials Science and Engineering
Georgia Institute of Technology

Date Approved: March 16, 2011

To my lovely family

Acknowledgements

Professor Vladimir, V. Tsukruk gave me the valuable opportunity when I join his research group as a fresh graduate student right after finishing undergraduate study. He inspired me how to conduct the scientific research by educating me from writing academic journal and report with the logical way of thinking. His advice, 'Be the diligent researcher, and be honest on the result' sincerely inspires me to be a doctor of philosophy in the materials science and engineering during my Ph.D. study. With his great guidance, advice, and encouragement for me, this work has been progressed.

I would like to thank to the committee members, Prof. Mostafa A. El-Sayed, Prof. Satish Kumar, Prof. Valeria Milam, and Prof. Yonathan Thio for the valuable advice and suggestions on this research.

This work would not be possible to be completed without support by the former SEMA lab members, Prof. Hyunhyub Ko, Prof. Srikanth Singamaneni, Dr. Sergy Pelechanko, Prof. Eugenia Kharlampieva, Prof. Valeriy Shevchenko, Dr. Veronika Kozlovskaya, Dr. Ray Gunawidjaja, Dr. Michael McConney, Dr. Yenhsi Lin, and current SEMA lab members, Maneesh K. Gupta, Zachary A. Combs, Dhaval Kulkarni, Ikjun Choi, Dr. Rajesh Kodiyath, Whitney Davis, and Seth Young. We also thank Prof. Mohan Srinivasarao, and Minsang Park for providing access to some Raman instrument and Dr. Joe Slocik for XPS measurement (AFOR). Thanks to Benjamin Weintaub for great collaboration. I also would like to thank our collaborators Prof. E. L. Thomas, Prof. M. C. Boyce, Prof. J.-H. Jang, Prof. K. Bertoldi from MIT. I am grateful for the financial support from ARMY Research Office (ARO), Department of Homeland Security (DHS) through Agiltron Inc., Defense

Advanced Research Projects Agency (DARPA) through EngeniusMicro LLC, and National Science Foundation (NSF).

Special thanks are due to my lovely family, Hun Chang, Kyongok Moon, Junghoon Chang, Sunro Hong, Inyoung Chang, Hwanghoon Lee, Sookhee Han, and Kyeore Lee. Norberto Cintron and Mercy Cintron gave me valuable support. Without their support, this work could not have been achieved. Also my friends Beumjin Yoon, Dr. Hangi Chse, Dr. Namtae Jo, Changguen Yoo, Changmin Jung, Minseok Ji, Minsung Choi, Minguk Kim who gave me valuable discussions during this study.

List of Tables

List of Figures

Summary

The work presented in this dissertation suggests novel design of chemical plasmonic sensors which have been developed based on Localized Surface Plasmon Resonance (LSPR), and Surface-enhanced Raman scattering (SERS) phenomena. The goal of the study is to understand the SERS phenomena for 3D hybrid (organic/inorganic) templates and to design of the templates for trace-level detection of selected chemical analytes relevant to liquid explosives and hazardous chemicals. The key design criteria for the development of the SERS templates are utilizing selective polymeric nanocoatings within cylindrical nanopores for promoting selective adsorption of chemical analyte molecules, maximizing specific surface area, and optimizing concentration of hot spots with efficient light interaction inside nanochannels. The organic/inorganic hybrid templates are optimized through a comprehensive understanding of the LSPR properties of the gold nanoparticles, gold nanorods, interaction of light with highly porous alumina template, and the choice of physical and chemical attributes of the selective coating.

Furthermore, novel method to assemble silver nanoparticles in 3D as the active SERS-active substrate has been demonstrated by uniform, in situ growth of silver nanoparticles from electroless deposited silver seeds excluding any adhesive polymer layer on template. This approach can be the optimal for SERS sensing applications because it is not necessary to separate the Raman bands of the polyelectrolyte binding layer from those of the desired analyte. The fabrication method is an efficient, simple and fast way to assemble nanoparticles into 3D nanostructures.

Addressable Raman markers from silver nanowire crossbars with silver nanoparticles are also introduced and studied. Assembly of silver nanowire crossbar structure is achieved by

simple, double-step capillary transfer lithography. The on/off SERS properties can be observed on silver nanowire crossbars with silver nanoparticles depending on the exact location and orientation of decorated silver nanoparticles nearby silver nanowire crossbars.

As an alternative approach for the template-assisted nanostructure design, porous alumina membrane (PAM) can be utilized as a sacrificial template for the fabrication of the nanotube structure. The study seeks to investigate the design aspects of polymeric/inorganic hybrid nanotube structures with plasmonic properties, which can be dynamically tuned by external stimuli such as pH.

This research suggests several different organic/inorganic nanostructure assemblies by various template-assisted techniques. The polymeric/inorganic hybrid nanostructures including SERS property, pH responsive characteristics, and large surface area will enable us to understand and design the novel chemical plasmonic sensors.

Chapter 1. Introduction

1.1. Background

Surface plasmon resonance (SPR) is caused by the collective oscillations of conduction electrons on the metal surface when the electrons interact with the electromagnetic field of the incident light.[1,2] This light-metal interaction known as plasmonics has received much attention with recent advances in nanofabrication techniques and due to its potential applications in chemical and biological sensors, optical devices, and photonic circuits.[2,3] Plasmonic sensors have been developed based on Localized Surface Plasmon Resonance (LSPR) and Surface-enhanced Raman scattering (SERS). SPR is usually excited on thin metal film interface and propagates along the metal surface, which decays rapidly further away from the metal surface reaching only several hundred nanometers.[4] When the analytes are adsorbed on the surface, the changes of the refractive index on the metal surface lead to the shifts of the plasmon resonance condition. SPR based sensing application has been developed utilizing prism and grating to detect the shifts of wavelength or angle.[5]

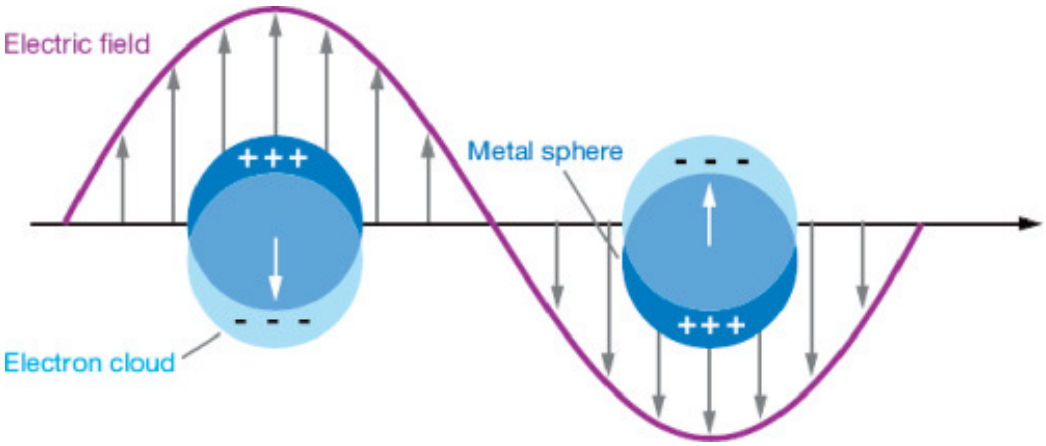

Figure 1.1. Schematic illustration of a localized surface plasmon of a metal sphere showing the displacement of the electron charge cloud relative to the nuclei.[2]

LSPR is nonpropagating plasmon excitation which occurs when the photons are confined within metal nanostructures such as nanoparticles and around nanoholes or nanowells of thin metal films.[6] In an electromagnetic viewpoint, metals can be considered as a plasma of electrons, which is composed of polarizable, mobile free electrons, and a immobile positive ion core. Interaction of the electromagnetic wave with a metal causes the free electrons to coherently oscillate at the plasmon frequency (ω_p) against the immobile positive ion lattice.

When the electrons are confined in a finite system such as nanoparticles, where the surface effects dominate the bulk contribution, the plasmon resonance frequency is altered compared to the bulk metal. For example, the plasmon resonance frequency of the spherical metal nanoparticle in vacuum is given by $\frac{\omega_p}{\sqrt{3}}$, where ω_p is the plasmon resonance of the bulk metal in vacuum.[7] When the frequency of the incident light is in resonance with the metal nanoparticles which are much smaller than the incident wavelength, the conduction electrons of nanoparticles are excited. The polarization of the conduction electrons in the nanoparticles by the electromagnetic radiation results in a strong induced electric field at the surface (Figure 1). The field induced at the surface of the nanoparticles is given by equation (1). [8]

$$E_{induced} = \left[\frac{\varepsilon_1(\omega) - \varepsilon_2}{\varepsilon_1(\omega) + 2\varepsilon_2} \right] E_{incident} \qquad 1.1.$$

where, $\varepsilon_1(\omega)$ is the complex dielectric function of the metal structure and $\varepsilon_2(\omega)$ is the relative permittivity of the surrounding medium. When the exciting electromagnetic

radiation is in resonance with the dipolar plasmon of the nanoparticle ($\mathrm{Re}(\varepsilon_1) = -2(\varepsilon_2)$), the nanoparticle radiates light with characteristic parameters for the dipolar plasmon.

The spectral position and intensity of the LSPR band depend on the size, shape, composition of metal nanostructures and local dielectric environment. Various metal nanostructures with well controlled shape, size such as nanorods, nanoprisms, nanotubes, and nanowires have been synthesized and studied due to their unique optical properties.[2] For example, plasmon resonance of metal nanorods splits into two peaks, longitudinal mode and transverse mode and these two peaks are separated more as the aspect ratio is increases. Nanoprisms have even more different plasmon resonances which show large field enhancement at the tip.[2] Various metal nanostructured materials have been fabricated into arrays for LSPR based plasmonic sensing application via lithographic techniques such as nanosphere lithography, colloidal lithography, and soft lithography well ordered metal nanostructure arrays.

When the spherical metal nanoparticles are interacting with each other or assembled into arrays, the resulting LSPRs are split or shifted due to the coupling effect. The distances between adjacent nanoparticles are important because the level of aggregation of nanoparticles causes the electromagnetic interactions and distinct color changes (LSPR peak shifts), which can be utilized for the colorimetric detection.[9] Besides, LSPR is sensitive to the changes in the local dielectric constant of the surrounding medium, thus, LSPR has been exploited for label-free optical sensing. When analytes are adsorbed onto the metal nanostructure, refractive index changes on plasmonic nanostructures can be used to monitor the real time anlaytes adsorption.[2,10] LSPR based plasmonic sensor has been employed to detect analytes utilizing even single nanoparticles showing better sensitivity than thin metal films of SPR based sensor and requires simpler instrumentation.[11,12]

1.2. SERS based sensing

Since SERS is firstly discovered on roughened noble metal surface, it has been emerged as a powerful analytical technique for the trace level detection (down to a single molecule) of chemical analytes due to high sensitivity, selectivity, rapid response, and portability.[13,14] Inelastic scattering of photon is the physical phenomenon behind Raman spectroscopy.[15] The LSPR on metal nanostructure is accompanied with electromagnetic field enhancement leading huge enhancement of inelastically scattered light intensity which is the source for SERS. Due to the extremely small Raman scattering cross section for most molecules resulting in the weak inelastically scattered signal, Raman scattering had been considered not the best choice for the sensing application compared to the other analytical tools such as Fourier-transform infrared (FTIR) or UV/Vis spectroscopy.

However, when the analyte molecules are adsorbed onto the roughened metal nanostucture, the vibration spectrum intensity of the analytes is dramatically enhanced, and the phenomenon is so called SERS (Figure 2). SERS enhancement is caused by both electromagnetic enhancement and chemical enhancement.[13, 16] While electromagnetic enhancement occurs when the incident light is in resonance with the surface plasmon of metal nanostructures, chemical enhancement is caused by the electronic state shift of analyte molecules due to the interaction with metal.[8,17] Electromagnetic enhancement contributes several orders of magnitude higher enhancement than chemical enhancements. The large electromagnetic enhancement in close interstices (few nm) of metal nanostructures, termed as '*hot spots*', is responsible for the huge enhancement of Raman scattering cross sections of the molecules.

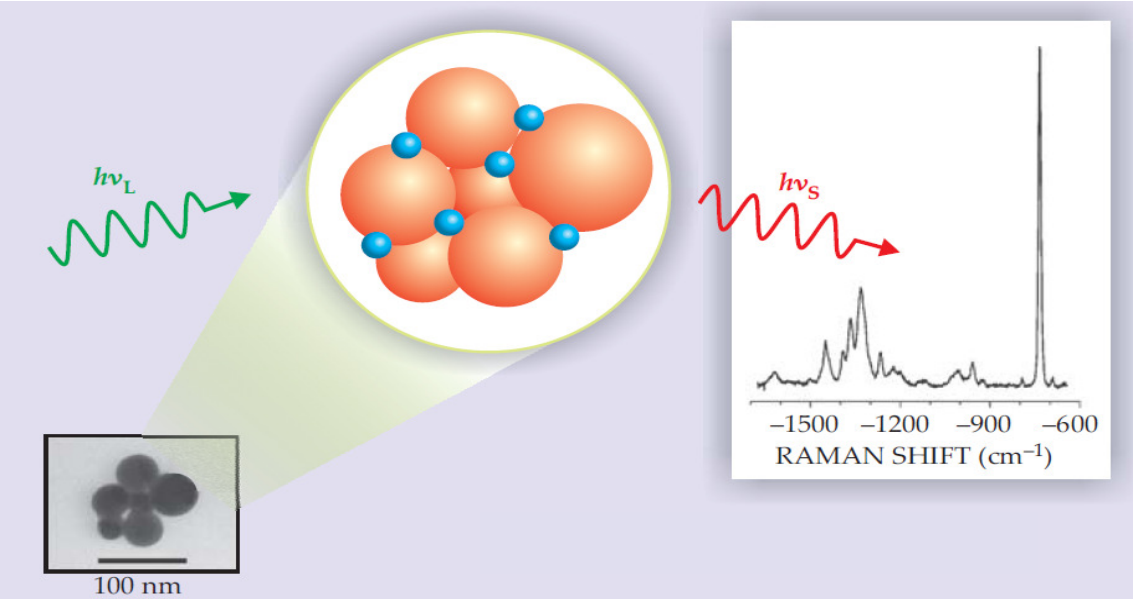

Figure 1.2. Surface-enhanced Raman Scattering. Metal nanoparticles (orange) and adsorbed molecules (blue) on a surface. SERS spectrum shows molecular vibration energies from the frequency shift between incident light (green) and scattered light (red).[16]

In order to detect trace amount of chemicals, it is important to maximize the SERS enhancement by optimizing the noble metal (Au, Ag, Cu) nanoparticles arrays. Because LSPR of noble metal nanoparitcles are in visible regime, they have been studied for the novel design of SERS substrate for chemical sensing applications, and medical diagnostics.[1,18] When the metal nanoparticles are close to each other, the plasmons of nanoparticles interact and the absorbed analyte molecules in the gap experience large capacitive field from opposite charges separated by small distance.[8] The precise control and tuning of the inter-particle gaps of the metal nanoparticle arrays will result in different condition of collective plasmon coupling, which can affect the SERS with a broad range of excitation from UV-Vis to near IR region. Therefore, tuning surface plasmons of metal nanoparticle arrays is the key factor to design SERS based sensors.

1.2.1. SERS based chemical sensing

Trace level detection of explosives and hazardous chemicals is high demand with increasing threat from terrorism and harmful environments. The key requirements for designing sensor for the chemical warfare agents and toxic environmental pollutants are the selectivity and sensitivity. The chemical sensors are usually engineered to sense only one specific analyte, thus it is not practical to monitor the analyte when there are various analytes in real-life application. It is even more challenging to integrate each specific response from each analyte into one system.

For example, chemical sensing applications require a single sensor that can reliably sense several different gases and chemicals simultaneously and provide selective response. It is useless if a sensor reads "all clear" to VX nerve gas because it does not sense the thiolate group, but the user drops dead to mustard gas because the sulfonium salt that attacks the skin could not be detected. Although the typical chemical sensors such as chemresistors and cantilever sensors show impressive sensitivity, they are useful if one specific type of response is determined. Clearly, sensors must be designed and fabricated to be more practical, dynamic, and capable of responding to diverse environmental analytes.[19]

SERS based chemical sensors have been applied for the trace level detection of various hazardous chemicals such as pesticides,[20] toxins,[21] nuclear waste,[22] and explosives.[23] SERS based sensor has been investigated and developed for the detection of trace-level of analytes due to its high sensitivity and selectivity. Several characteristic Raman bands from the analyte molecules can be monitored to identify the specific molecules, SERS based sensor is considered as dynamic optical chemical sensor design. Utilizing colloidal Ag and Au, Kneipp et al. successfully demonstrated SERS based sensing for trinitrotoluene (TNT)

explosive down to 1 pg level.[24] Even though the outstanding SERS based chemical sensors have been demonstrated, the facile fabrication of robust, stable SERS substrates for hazardous chemicals with huge enhancement is still challenging because the stability of aggregated nanoparticles is the main obstacle for assembled structures, and the fabrication of complex nanostructures is labor- and cost-intensive and sometimes hard to extend to large dimensions.

1.2.2. Design of Nanostructured SERS-active Substrates

To date, a variety of metal nanostructured SERS-active substrates for chemical sensors to detect explosives and hazardous chemicals have been suggested to enhance Raman scattering utilizing roughened metal surfaces, 1D nanoparticles array, nanodisk array, and 2D nanoislands, nanohole arrays as discussed in a number of recent reviews and original publications (Figure 3).[2,10,25,26,27,28] Even though 1D and 2D SERS substrates can provide modest SERS enhancement,[18,29] these substrates have showed inconsistent and low Raman signal because of poor control of aggregates or surface structures.[16] The ability of traditional SERS chemical sensors with these traditional designs to detect small, non-resonant organic molecules such as those belonging to important hazardous chemicals and explosives is still very limited. An outstanding challenge of SERS-based detection in practical applications is the lack of developing selective coatings which have weak Raman spectra for robust SERS-active substrates with hot spots. Fabrication of intrinsically clean SERS substrates and removal of adsorbing impurities are also challenging. For practical applications, the sensitivity of 2D metal structures remains modest due to a limited concentration of hot spots. Therefore, the highly-ordered, robust, reproducible SERS substrate is needed for the detection of trace-level of chemicals. 3D porous metallic

substrates are promising but have not been utilized fully to enhance the SERS effect because of limited light propagation.

Sensitive SERS substrates can be fabricated by depositing metal nanoparticles inside the pores of synthetic nanoporous semiconductors such as silicon[30] and gallium nitride.[31] The nanoporous semiconductors are favored as SERS substrates due to their easy fabrication, uniform pore size, and vertical alignment of the nanopores over large area with precise control of pore depth. However, uniform metal coating deeper into the nanopores is not easily achievable with immersion plating or electrochemical deposition.[31]

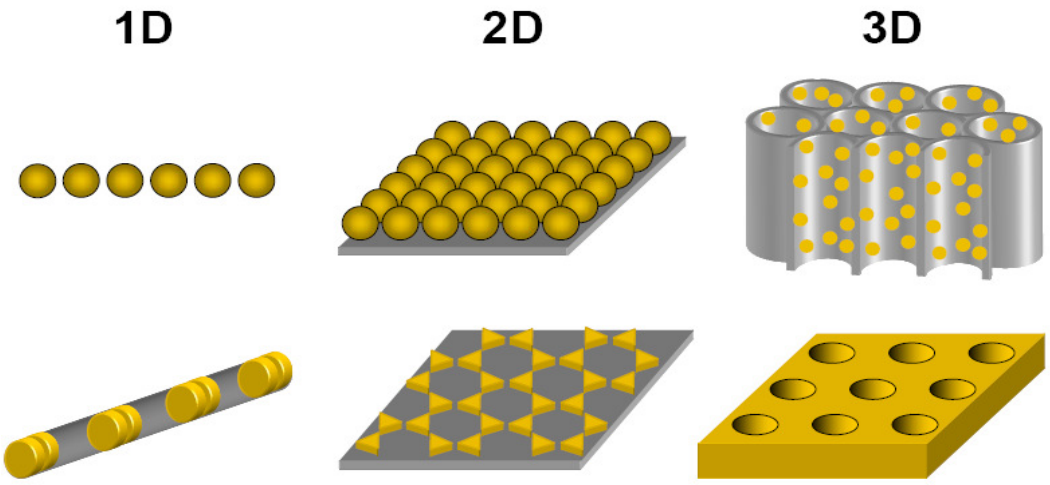

Figure 1.3. Examples of 1D, 2D, and 3D arrays of nanostructures for SERS substrates.[8]

Anodic alumina membranes with highly ordered cylindrical nanopore arrays have been used as templates to prepare metallic nanostructures for SERS applications.[32,33,34,35] Unlike the other SERS substrates with limited light propagation, porous alumina membranes with vertical, though nanocanals are beneficial for the efficient light interaction because of optical transparency and waveguide properties.[36,37] Recently, anodic alumina membranes with hexagonally close-packed nanopores have been used as templates to fabricate 2D metal

arrays.[35] The dependence of Raman intensity on the gap-to-diameter ratio showed exponential increase above 2 nm, in accordance with the theoretical prediction.[38]

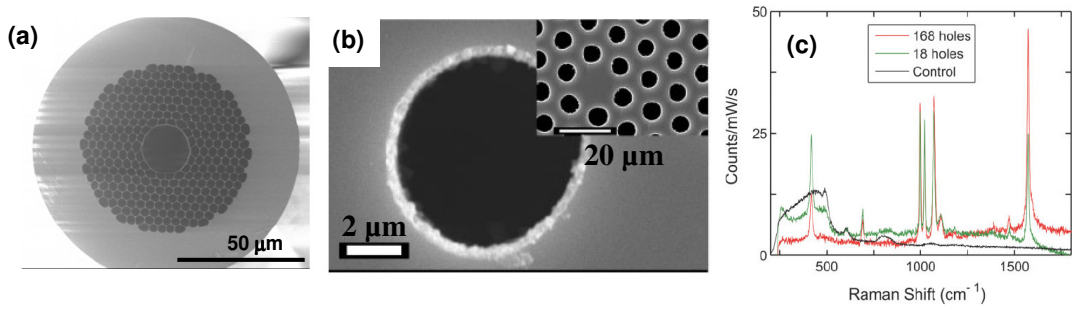

Figure 1.4. SERS optical fibers with microchannels and SERS spectra.[39,40]

The combination of micro- and nanoporous structures is advantageous for SERS-based sensors due to efficient through transport of analytes and high surface area (Figure 4).[39,40] Furthermore, the long-range ordering of the periodic metal nanostructures provides additional field enhancement. Compared to the conventional planar SERS substrates or 3D SERS substrates without any optical guiding, the 3D substrates with waveguiding ability causes the excitation of large number metal nanostructures and the efficient collection of the scattered Raman photons. The critical challenge of using porous optical fibers for SERS detection is the difficulty in filling the long hollow fiber with metal nanoparticles without pore clogging. The limited mass transport throughout the continuous microscopic channels compels a channel diameter of several micrometers that decreases their efficiency tremendously.[41,42]

1.2.3. Design of Nanostructured combined with Raman markers

One dimensional metal nanostructures with the capability of guiding electromagnetic energy are attractive for nanoscale optical devices and circuits.[43,44] These nanostructures can be also combined with Raman markers to exploit SERS phenomena.[8,25,45,46,47,48,49] One-dimensional nanostructures show promising capabilities for guiding and confining the exciting light in nanogaps ("hot spots") provides dramatically enhanced local electromagnetic field and coupling of localized surface plasmon resonances. To explore this important phenomenon, a number of different noble metal nanostructures have been fabricated, assembled, synthesized, and some have been suggested and integrated with prospective Raman markers for chemical and biological detection.[10,118,27,50,51,52,53] Figure 1.5 shows several representative nanostructures which have been fabricated from metal nanostructures integrated with Raman markers.[54,55,56]

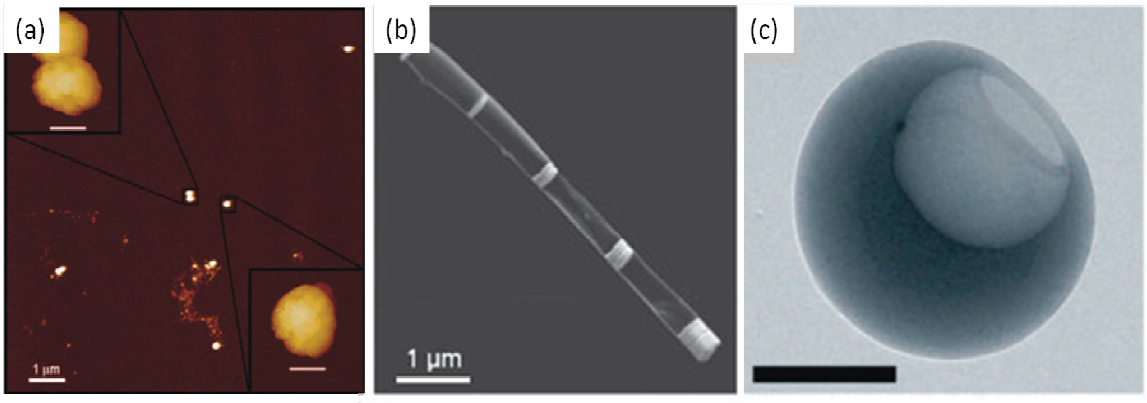

Figure 1.5. Examples of nanostructures which can be combined with Raman markers, (a) nanoparticle dimers (b) OWL-Generated nanodisk arrays (c) composite magnetic

1.3. LSPR Responsive Organic/Inorganic Hybrid Nanostructure

Responsive polymeric materials and structures which can readily change their properties (optical, electrical, mechanical) or shape sensitive to external stimuli (pH, moisture, temperature) are extremely important for a wide variety of applications such as sensors,

actuators, adaptive surfaces and interfaces, and drug delivery.[57,58,59,60] When the responsive polymer is incorporated with noble-metal nanoparticles, an external stimuli such as pH, temperature can turn into optical response for sensing application.[61] The structural changes in a responsive polymeric/metal nanoparticles hybrid 1D nanostructure to external stimuli can be translated to readable optical signal.[62] Responsive organic/inorganic composite nanostructures haves been studied to design LSPR based sensor utilizing reversible aggregation of nanoparticles which causes distinct LSPR peak shifts.[63] The strategy of this approach is to reversibly control the spatial distribution of nanoparticles within responsive polymeric matrix. Xu et. al demonstrated polymeric micelle structure of polyamide core with temperature responsive poly (*N*-isopropylacrylamide) (PNIPAM) outer shell which covalently decorated with Au nanoparticles. As the temperature changes, PNIPAM domain is swollen and collapsed reversibly, which leads the interparticle distance changes resulting in shift of UV-vis absorption bands.[63]

Yet, another promising choice of responsive polymeric material can be block copolymers. Block copolymers are comprised of two or more chemically distinct, and often immiscible, polymer chains covalently bound together.[64,65] In the simplest case of diblock copolymer, thermodynamic incompatibility between two blocks drives the system to self-organize by microphase separation to minimize the interfacial energy between the dissimilar blocks. The organized phase separation in diblock copolymer results in a variety of periodic structures such as spherical, cylindrical, double gyroid, and lamellar with the individual domains on the order of few tens of nanometers.[66,67] Block copolymer/metal nanoparticles composite material has been studied as a promising LSPR based responsive hybrid nanostructure. When metal nanoparticles are selectively in situ reduced in one polymer domain of diblock copolymer self-organized microphase separation results in various well

ordered periodic metal nanostructure arrays. In situ reduction of metal nanoparticles in polymeric domain is advantageous in stability and reproducibility.[68,69] Reversible changes of surface morphology of diblock copolymer thin film of which one domain can selectively be swelling or collapsed by the exposure to solvent vapors and the other domain remains as same state has been studied.[68]

Chapter 2. Goals, Technical Objectives, and Overview

2.1 Goals of the study

The goal of this study is to understand the SERS phenomena for 3D hybrid (organic/inorganic) templates in order to design SERS-active templates for trace-level detection of selected chemical analytes relevant to liquid explosives and hazardous chemicals. The key design criteria for the development of the SERS templates suggested here are utilizing selective polymeric nanocoatings within cylindrical nanopores for promoting selective adsorption of chemical analyte molecules, maximizing specific surface area, and optimizing concentration of hot spots with efficient light interaction inside nanochannels.

The organic/inorganic hybrid templates are optimized through a comprehensive understanding of the optical properties of the individual noble metal nanoparticles and their aggregates, and nanorods, interaction of light with highly porous alumina template, and the choice of physical and chemical attributes of the selective coating. Polymer coatings for chosen chemical analytes (relevant to practical needs) are investigated on their ability to selectively binding. The study also seeks to investigate the design aspects of polymeric/inorganic hybrid nanostructures with plasmonic properties, which can be dynamically tuned by external stimuli. Various general approaches in design and fabrication aspects of the proposed study are summarized in Scheme 1.

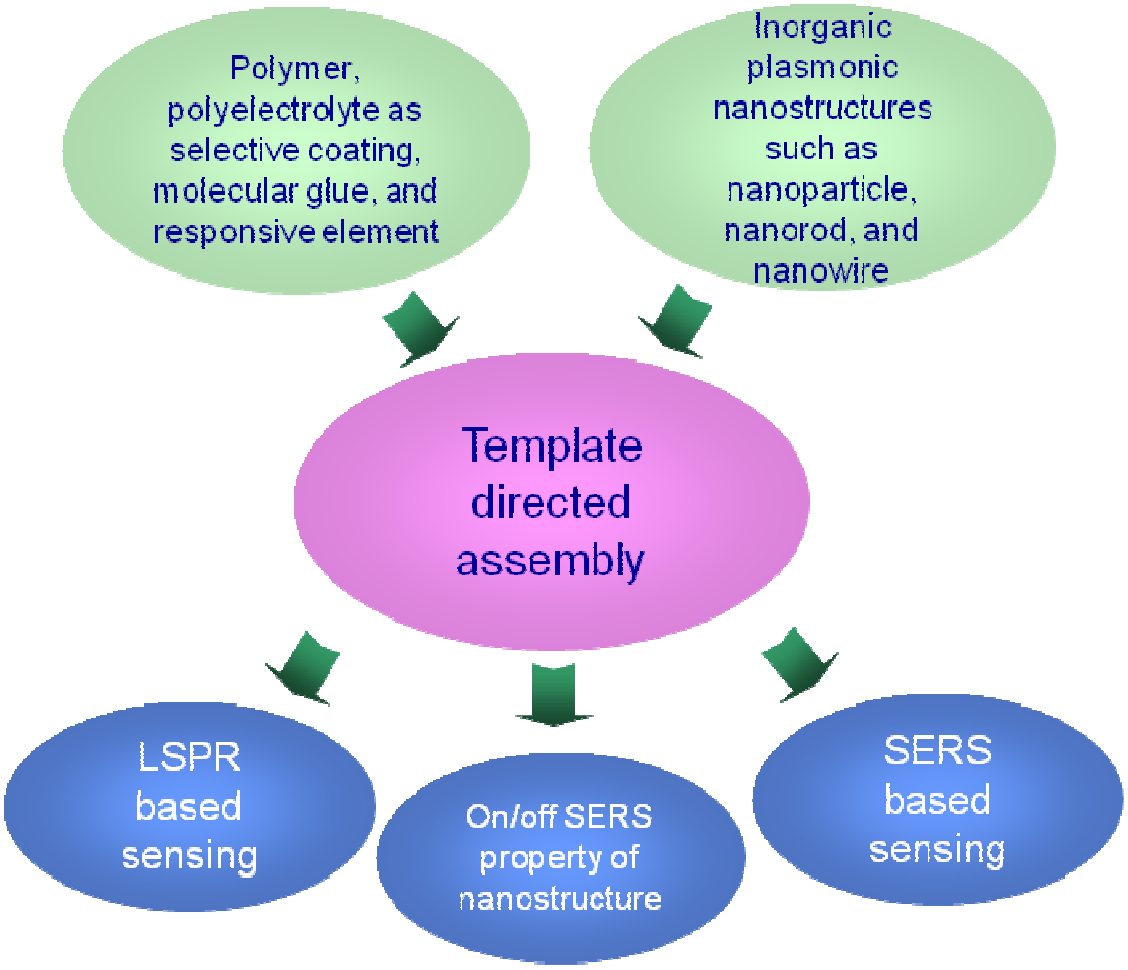

Scheme 2.1. Summary of proposed study of organic/inorganic hybrid nanostructures by template assisted methods for SERS and LSPR-based sensing applications.

2.2. Specific Technical objectives

- Understanding the optical properties of organic/inorganic hybrid templates fabricated with a wide range of noble metal nanoparticles such as gold/silver nanoparticles and gold nanorods with dimensions and composition suitable for SERS phenomena
- Investigating proper candidates of polymeric selective coating of 3D organic/inorganic hybrid templates for effective binding of selected chemicals from liquid phase

- Study interactions of organic/inorganic hybrid templates with selected chemicals such as hazardous chemical (perchlorate), and peroxide based liquid explosives (HMTD) establishing detection routines, lowest detectable limits, and selectivity of the label-free sensing
- Fabricate silver nanowire crossbars partially decorated with silver nanoparticles via double-step transversal capillary transfer microprinting approach and demonstrate their polarization-dependent SERS properties
- esign polymeric/inorganic hybrid nanostructures with the plasmonic properties, which can be dynamically tuned by external stimuli, and probe the optical response (absorption, scattering, SERS intensity)

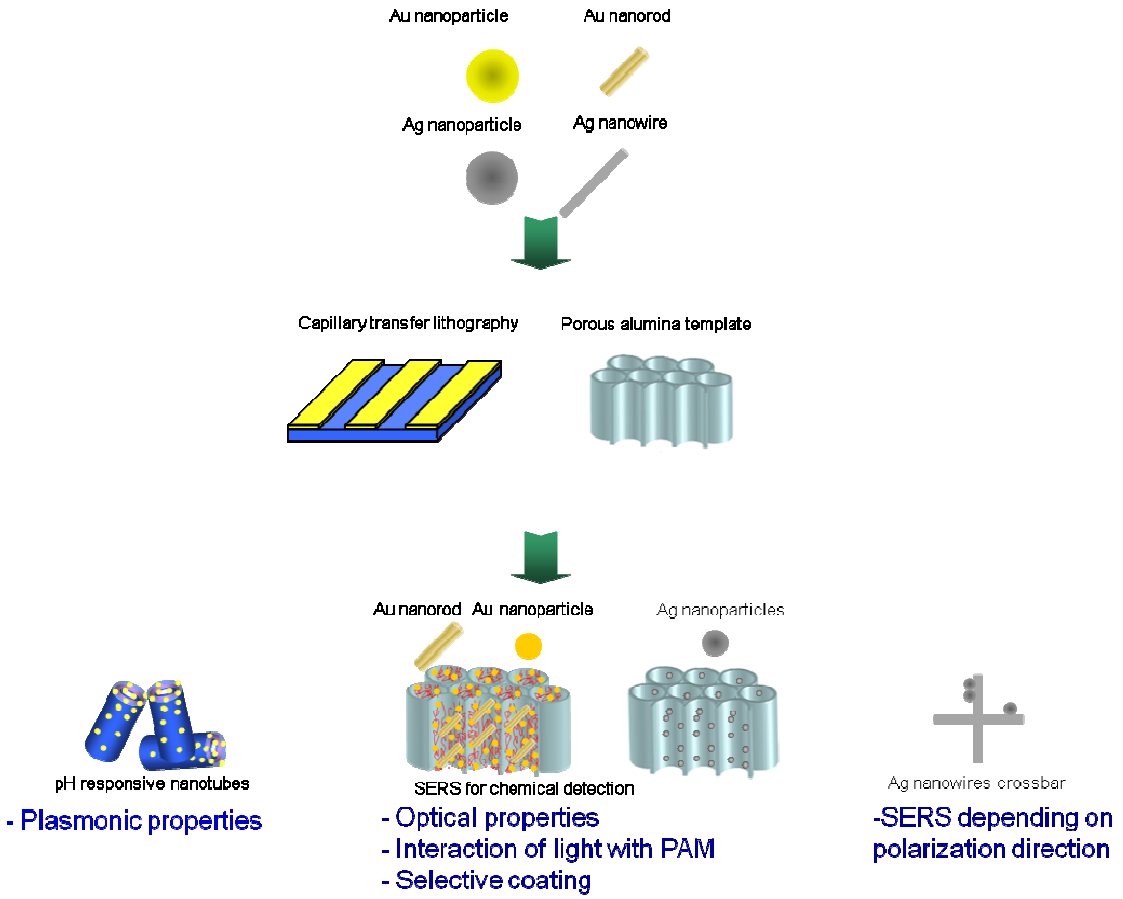

Scheme 2.2. Summary of materials for organic/inorganic hybrid nanostructures via templates assisted methods

2.3. Overview and Summary of Each Chapter

This dissertation presents the novel design of organic/inorganic nanostructure assembly for plasmonic sensing applications. In this study, we primarily focused on the assembly of nanostructures as the active SERS template for trace-level detection of selected chemical analytes relevant to liquid explosives, nanowires crossbar structure incorporated with nanoparticles which can be combined with addressable Raman markers, and LSPR based pH sensing organic/inorganic hybrid nanotube structure.

Table 2.1. Summary of the nanostructures for plasmonic sensing application.

Metal nanostructures	Assembly	Method of assembly	Method of detection
Au NP 	Integrated into PAM for 3D assembly	Vacuum infiltration	SERS based sensing
AuNP and AuNR 	Integrated into PAM for 3D assembly	Vacuum infiltration	SERS based sensing
Ag NP 	Integrated into PAM for 3D assembly	In situ growth from electroless deposited seed	SERS based sensing
AgNP and AgNW 	Nanowire crossbar with nanoparticles	Two-step transversal capillary transfer microprinting	On/off SERS property with Raman makers
AuNP and PS-P2VP nanotube 	Integrated into polymeric nanostube structure	Filled in into template(PAM) and released from PAM, in situ reduction of nanoparticles	LSPR based sensing

Table 2.1 summarizes the various nanostructures for plasmonic sensing application demonstrated in this study. The table illustrates that the various metal nanostructures are assembled into different geometries by specific fabrication methods. Each nanostructure was applicable for SERS based sensing by detecting the trace level of analytes (explosives,

hazardous chemicals) or LSPR based sensing at specific environmental condition (polarization direction of incident light, pH).

Chapter 1 presents comprehensive and critical reviews about the research related to nanostructure assembly for plasmonic sensing application and LSPR based responsive organic/inorganic hybrid nanostructures. This chapter introduces the current issues about the topic which need further investigation and development.

The goals and specific technical objectives of the study are addressed in **Chapter 2**. The brief overview of the entire dissertation is also included in this chapter.

In **chaper 3**, the experimental techniques employed for the synthesis and assembly of organic/inorganic nanostructures are introduced. This chapter also describes the characterization techniques for measuring optical properties, morphology, and SERS phenomenon of the organic/inorganic nanostructures such as UV-vis spectroscopy, confocal Raman spectroscopy, transmission electron microscopy, scanning electron microscopy, and atomic force microscopy. Besides, each chapter in afterward includes an experimental detail on each topic.

Chapter 4 demonstrates a novel design of SERS-active nanoporous substrate based on porous alumina membranes (PAMs) decorated with mixed nanoclusters composed of gold nanorods and nanoparticles. Monitoring trace-amounts of peroxide-based molecules is challenging due to the lack of common optical signatures (fluorescence, absorption in UV-vis range) or chemical functionality easily detectable with common experimental techniques.

To overcome this issue, we suggest a photochemical decomposition approach followed by the analysis of chemical fragments by fast, sensitive, reliable Raman spectroscopic method.

For 3D mixed gold nanorods and gold nanoparticles assembly with PAMs, vacuum infiltration method is utilized. We adopt polyacrylonitrile (PAN) as the selective coating for HMTD molecules and the detectable amount of HMTD below 2 pg demonstrated here is about three orders of magnitude lower than the current limit of detection. Table 2.2 summarizes our differen metal nanostructure assemblies with PAMs for the trace level detection of various analytes using proper selective coating. We have reported the design of SERS-active gold nanoparticles assembly with PAMs allowing for a trace level of detection of explosive compounds, 2,4-dinitrotoluene (DNT) and trinitrotoulene (TNT), down to 0.1-0.05 ppt which is more than four orders of magnitude better than that previously reported (1 ppb).[70]

Table 2.2. Summary of the analytes investigated, technique, materials employed and limits of detection.

Analytes	Metal nanostructures	Method of detection	Selective coating
DNT	Au NP	Direct*	PEI
TNT	Au NP	Direct*	PEI
HMTD	AuNP and AuNR	Indirect** (by dissociation)	PAN
Perchlorates	Ag NP	Direct*	N/A
*"Direct" detection of the analyte bound to a selective layer **"indirect" detection of the analyte by reacting with a reagent or by dissociation into detectable fragments.			

The overall intensity of Raman spectra (peak assignment are discussed later) from PAM substrates loaded with mixed gold nanorods and gold nanoparticles is an order of magnitude higher compared to the PAM loaded with gold nanoparticles alone or gold nanorods alone to develop the previous research. The enhanced SERS performance of the organic/inorganic hybrid template with mixed gold nanorods and gold nanoparticles is demonstrated with the supporting evidences such as UV-vis data.

During trace level detection of HMTD molecules utilizing Raman spectroscopy, the laser-induced photocatalytic decomposition is observed. To clarify the decomposed fragments of HMTD, we perform X-ray photoelectron spectroscopy (XPS) of HMTD on gold nanoclusters before and after laser irradiation. The XPS spectrum clearly shows the chemical composition of the fragments of the HMTD molecules.

The key design criteria for the development of the SERS templates demonstrated in this study are utilizing selective polymeric nanocoatings within cylindrical pores for promoting selective adsorption of chemical analyte molecules, maximizing specific surface area, and optimizing concentration of hot spots. The SERS templates was optimized through a comprehensive understanding of the optical properties of the individual noble metal nanoparticles and their aggregates, and nanorods, interaction of light with highly porous alumina template, and the choice of physical and chemical attributes of the selective coating. Polymer coatings for chosen chemical analytes (relevant to practical needs) are investigated on their ability to selectively binding. Therefore, tailored selective polymer coating, mixed nanoclusters, and laser-induced photocatalytic decomposition are all critical for achieving

label-free detection of unstable and non-resonant organic molecules so that these aspects are addressed in this chapter.

Chapter 5 demonstrates the in situ growth of silver nanoparticles in PAMs for use as a SERS active substrate. The critical challenge of using these porous membrane substrates or the long hollow microfibers for efficient SERS detection is the difficulty of filling nanosized cylindrical pores with large amount of metal nanoparticles without clogging these nanostructures. However, the fabrication method in this study is simple, cost effective, and fast, while providing control over the size of silver nanoparticles through the entire length of the cylindrical nanopores with uniform particle density inside the pores un-achievable by the traditional infiltration technique. The in situ growth of silver nanoparticles from electroless-deposited seeds on the interior of the PAM resulted in the formation of numerous hot spots which facilitated significantly higher SERS enhancement compared with previously reported porous substrates.

The silver nanoparticles size is controlled by the particle growth time at a fixed concentration of growth media. The changes in size and density of the nanoparticles inside the PAMs were monitored by SEM to understand the kinetics of nanoparticle growth under confined pore conditions. The grown silver nanoparticles (about 40 nm) are uniformly formed on the wall of PAMs about 30 minutes of growth. At beyond this time, the size of nanoparticles increased above the useful limit for SERS and these larger (>70 nm) nanoparticles clogged the pores with the average diameter of PAMs (240 nm). After comparison of the SERS activity of silver nanoparticles decorating the PAMs at various in situ growth times utilizing Rhodamine 6G (R6G), SERS substrates with about 28 minutes growth time provides

strongest SERS enhancement because the coupled plasmon resonance of the aggregated silver nanoparticles nearly overlaps with the wavelength of the excitation laser (514 nm).

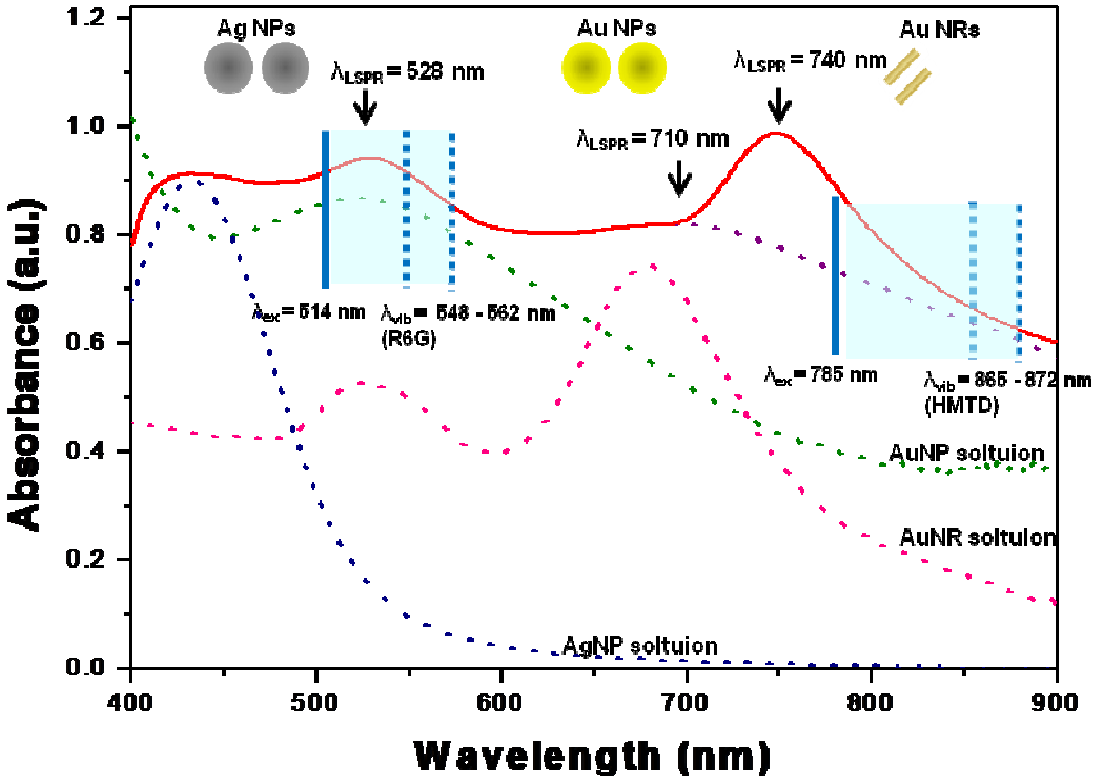

Figure 2.1. Representative UV-vis absorption data showing a shift in the absorbance of the silver, gold nanoparticles, gold nanorods following aggregation in PAMs. The blue lines indicate the spectral range which will allow for the highest intensity SERS spectrum of R6G using a 514 nm laser, HMTD using a 785 nm laser.

We were able to find the relationship among the λ_{LSPR} of nanostructure, wavelength associated with the Raman peak of the analyte, and excitation wavelength for maximum SERS enhancement based on previous experimental results of our group as well as literature values, which show that the λ_{LSPR} of nanostructure would be located approximately 1/3 of the distance between the excitation wavelength and the wavelength associated with the Raman peak of the analyte.[71]

This provides the important information needed to guide experiments to achieve optimal SERS enhancement for the specific analyte. The in situ grown silver nanoparticles from electroless deposited seeds inside PAMs were assembled to provide the optimal size of the nanoparticles necessary for large SERS enhancement. This fabrication method is simple and fast providing uniformly-controlled size of silver nanoparticles over the large surface area of the interior pore walls of the PAMs.

We demonstrated 10 ppb level detection of hazardous chemical such as perchlorate by simple and direct exposure to liquid analytes with the silver nanoparticle-decorated porous structures.

In **chapter 6**, fabrication of the silver nanowire crossbars partially decorated with silver nanoparticles is introduced via double-step transversal capillary transfer microprinting approach and demonstrated their polarization-dependent SERS properties. SERS intensity of various hot spots (nanowire junctions and nanowire-nanoparticle junctions) can be turn on/off on demand by the rotation of the polarization plane which excites specific transversal plasmon resonances and initiates selective excitation/suppression of central and auxiliary SERS hot spots.

To prepare crossbar arrays of silver nanowires, the sacrificial polystyrene micropatterns were used as guided templates for the deposition of silver nanowires. The PS pattern was lifted off by toluene leaving patterned stripe arrays of silver nanowires after tilted dry of the nanowire solution. After repetition of the process of PS micropatterns perpendicular to the first layer of silver nanowire arrays, the crossed arrays of silver nanowires were generated. The silver nanoparticles formed during synthesis of silver nanowires were located nearby the

nanowire crossbars. The SERS at the junction of nanowire and spherical nanoparticles shows the polarization-dependent characteristics.

In Chapter 7, the study of organic/inorganic hybrid nanostructures for LSPR-based sensing is introduced. The facile fabrication of high aspect ratio nanotubes from responsive block copolymer, polystyrene-block-poly (2-vinylpyridine) (PS-b-P2VP) and in situ grown gold nanoparticles are introduced. PS-b-P2VP nanotubes are fabricated by template assisted assembly. Nanotubes were formed by infiltration of PS-b-PVP into cylindrical pores of porous alumina membranes using spin assisted method and released by dissolving templates.

Solvent annealing was employed to facilitate ordered phase separation of the block copolymer within the nanotube structure, followed by in situ formation of gold nanoparticles in the P2VP domains occupying the inner and outer shell of the nanotubes. By exposing PS-b-P2VP nanotubes to the gold salt solution, $HAuCl_4^-$ ions bind to the protonated pyridine units of the P2VP resulting in pyridinium salt. Subsequently nanotubes are immersed into aqueous solution of reducing agent resulting in the formation of about 15 ± 2 nm in diameter of gold nanoparticles in P2VP domains

Owing to the pH sensitive nature of P2VP block which has a coil to globule transition property above pH 3.6, the PS-b-P2VP-gold nanoparticles nanotubes show reversible changes in topology, size (up to 25%), and collective plasmon resonance appearance. Due to the protonation of nitrogen in pyridine group which causes electrostatic repulsion leading to swelling of the polymer chains when the P2VP is exposed to pH2 solution resulting in grainy morphology of nanotubes. Upon this morphology change, the mechanical integrity of nanotubes is preserved by the glassy PS block in nanotube structure. When PS-b-P2VP

porous nanotubes were exposed to the neutral condition (pH 7 solution), the highly grainy morphology of nanotubes is apparently recovered almost back to the initial smooth surface.

The morphology changes of PS-b-P2VP nanotubes in pH 2 solution resulted in red shift of the plasmon resonance of the encapsulated gold nanoparticles. We suggest that the swelling of the P2VP blocks causes the aggregation of the gold nanoparticles at the outer surface. The exposure of nanotubes to neutral solution (pH 7) results in the gold nanoparticles rearrangement due to topology recovery resulting in a blue shift of the plasmon peak. The pH responsive nanotubes composed of PS-b-P2VP-gold nanoparticle exhibit a reversible change in the plasmon resonance position.

Finally, the general discussions of this study, future directions, and issues are discussed in **chapter 8**.

Chapter 3. Experimental Techniques

3.1. Gold Nanoparticles, Silver nanoparticles, Gold Nanorods, and Silver nanowires Synthesis

Gold nanoparticles about 30 nm in diameter capped with cetyltrimethylammonium bromide (CTAB) are synthesized by seed growth technique.[72] 20 mL aqueous solution containing 2.5 x 10^{-4} M HAuCl4 and 2.5 x 10^{-4} M trisodium citrate is prepared. 0.6 mL of ice cold 0.1 M NaBH4 is added to this solution with stirring. The solution immediately turned into orange-red color, indicating formation of gold nanoparticles seed solution. Three 20 mL vials (labeled A and B) are prepared. 9.0 mL of growth solution containing a mixture of 2.5 x 10^{-4} M HAuCl4 and 0.10 M CTAB solutions is added to these vials. 50 μL of 0.10 M ascorbic acid is added to these solutions and the resulting solutions are stirred gently. 50 μL of 0.10 M ascorbic acid is added to 90 mL of stock solution (C) containing a mixture of 2.5 x 10^{-4} M HAuCl4 and 0.10 M CTAB solutions. Then, 1.0 mL of the seed solution is mixed with vial A. After 10 sec, 1.0 mL of solution A is added to solution B. After 10 s, 1.0 mL of solution B is added to stock solution C. After the solution is kept at 25 °C for 24 h, the excess CTAB is removed by centrifugation 5000 rpm for one hour.

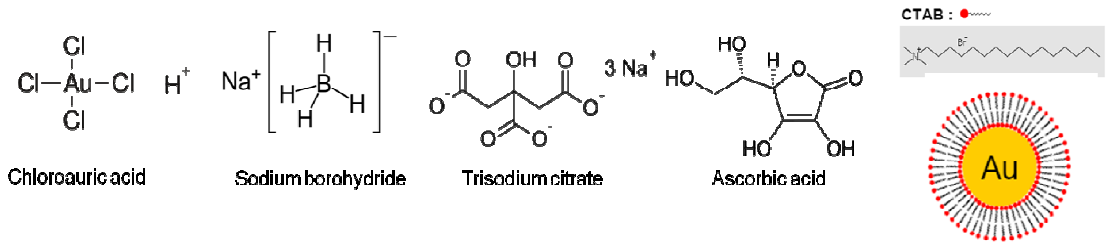

Scheme 3.1. Chemical compounds utilized for synthesis of gold nanoparticles.

Silver nanoparticles are synthesized by photoreduction of $AgNO_3$ in presence of sodium citrate by irradiation with UV light at room temperature.[73] 42.5 mg of $AgNO_3$ and 73.5 mg of sodium citrate are dissolved in 250 ml of Nanopure water (18 MΩ cm) and UV lamp (λ = 365 nm) is used as light source to the reduction process for 8 hrs. The size of the resulting silver nanoparticles are about 40 nm.

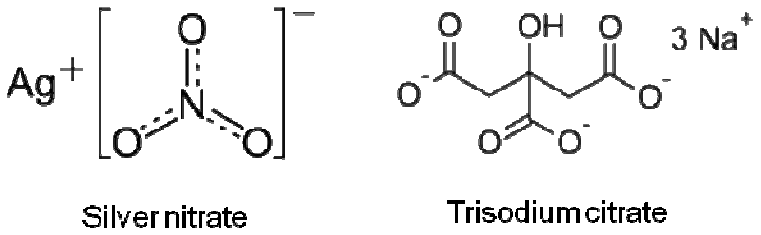

Silver nitrate Trisodium citrate

Scheme 3.2. Chemical compounds utilized for synthesis of silver nanoparticles.

Gold nanorods with the length of 80 ± 8 nm and the width of 19 ± 4 nm are synthesized using seed-mediated growth technique introduced by Murphy et al.[74] and El-Sayed et al.[75] Gold nanoparticle seed solution is prepared by addition of 0.6 ml of an ice-cold solution of 10 mM sodium borohydride into 10 ml of 2.5×10^{-4} M $HAuCl_4$ aqueous solution. It is worth noting that the gold chloride solution containing HCl did not produce desired seeds. 0.1 M of cetyltrimethylammonium (CTAB) is added under 10 min stirring. Color of the seed solution changed from yellow to brown. For making growth solution, 95 ml of 0.1 M CTAB solution, 1 ml of 10 mM silver nitrate solution, 5 ml of 10 mM $HAuCl_4$ solution are mixed and 0.55 ml of 0.1 M of ascorbic acid is added. Finally, 0.12 ml of seed solution is added into growth solution. The final solution is left overnight and the color turned into orange-brown. Gold nanorod solution is centrifuged two times at 5000 rpm for one hour each to remove excess of CTAB.

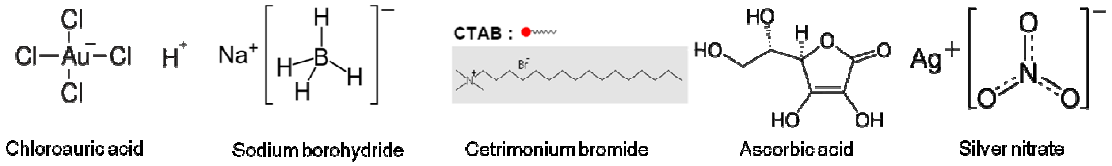

Scheme 3.3. Chemical compounds utilized for synthesis of gold nanorods

Silver nanowires are synthesized according to the well-known procedure. [76,77,78] All glassware are washed with soap, *aqua regia*, and rinsed thoroughly with de-ionized water. A 60 mL solution of 0.36 M poly(vinylpyrrolidone) (PVP, M_n = 1,300,000 g/mol) in ethylene glycol is heated at 160 ºC under constant stirring for one hour to remove water from the solution. A separate 30 mL solution of 0.12 M of silver nitrate ($AgNO_3$) in ethylene glycol is prepared at room temperature by vigorous vortexing. Sonication or heating was avoided, since it could lead to the unwanted formation of silver nanoparticles. Next, 50 µg of $Fe(acac)_3$ in 0.5 mL ethylene glycol solution is added into the hot PVP solution, followed by dropwise addition of the homogeneous silver nitrate solution. The dropwise addition is conducted manually using pipette. The solution mixture is allowed to stir for a minimum of one hour, or until the solution turns silhouette opaque-gray. The formation of silver nanowires is confirmed from optical microscope with 50x objectives in the dark field mode.

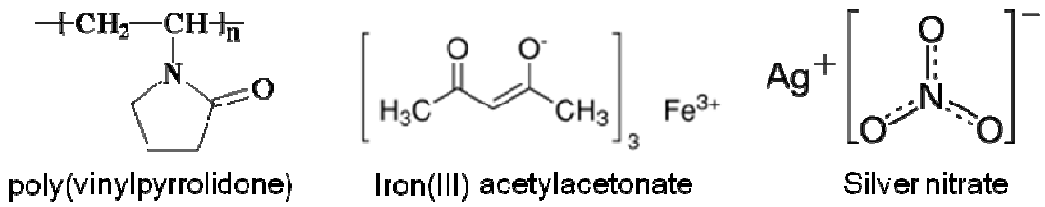

Scheme 3.4. Chemical compounds utilized for synthesis of silver nanowires

3.2. 3D Hybrid Templates Design

Porous alumina membranes with pore diameter of 100 nm, 250 nm and 60 μm thickness are purchased from Whatman (Anodisc 47). Inner surface of porous alumina membranes are modified with 0.2% aqueous solution of PEI (M_w = 55,000, Aldrich) by spin-coating (3,000 rpm, 30 sec) followed by rinsing with Nanopure water (18 MΩ cm). The surface of porous alumina membranes is modified with PEI, where columbic repulsions between positively-charged PEI and gold nanoparticles prevent the attachment of gold nanoparticles on the outer-surface of alumina membranes, which often cause the pore-blocking. The amine groups in the PEI are used to attach gold nanoparticles on the inner-walls of porous alumina membranes by partial replacement with the CTAB ligands on the gold nanoparticle surface during the filtration of gold nanoparticle solution. Gold nanoparticles solution is then passed through the modified membrane pores by vacuum suction.[118]

On the other hand, 0.2% aqueous solution of Poly (allylamine hydrochloride) (M_w = 70,000, Aldrich) are coated to immobilize silver nanoparticles. The top and bottom surface of porous alumina membranes are masked by stamping with polydimethylsiloxane (PDMS) coated with positively-charged polystyrene sulfonate (M_w = 70,000, Aldrich). Columbic repulsions between negatively-charged PSS and silver nanoparticles prevent the attachment of gold nanoparticles on the outer-surface of alumina membranes, which often cause the pore-blocking.[79] Silver nanoparticles solution is then passed through the modified membrane pores by vacuum suction.

Polyacrylonitrile (PAN) which is employed as a selective coating is dissolved in N,N-dimethylformide (DMF). Gold nanorods and nanoparticles solution are vacuum filtrated into the porous alumina membrane several times by vacuum suction to achieve uniform coating inside PAMs. After this step, one more coating of PAN by spin-cast (4000 rpm, 30 sec) is carried out.

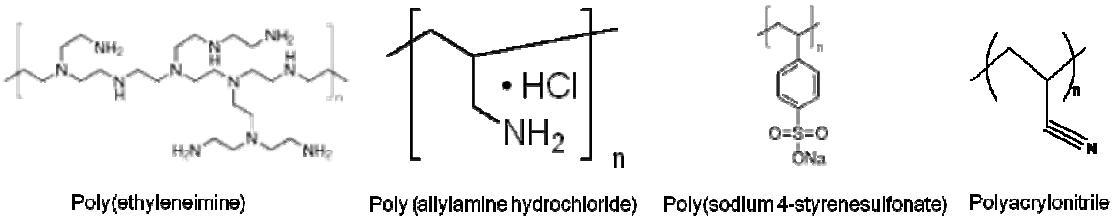

Scheme 3.5. Polymers utilized for 3D SERS-active templates

3.3. Transmission Electron Microscopy (TEM) and Scanning Electron Microscopy (SEM), Energy Dispersive X-ray Spectroscopy (EDS)

The shape and size of synthesized nanostructures such as gold, silver nanoparticles and gold nanorods are exploited precisely by transmission electron microscopy (TEM) (JEOL 100CX-2 electron microscope). The distribution of in situ reduced gold nanoparticles in polymer matrix is investigated by TEM. Scanning electron microscopy (SEM) (Hitachi-3400, LEO 1530) was used to investigate the assembled nanostructures. The morphology of fabricated polymeric/inorganic hybrid nanostructure was investigated by SEM. For SEM analysis, samples was mounted on silicon substrate, put on top of conductive carbon tape, and sputtered gold lightly with the operating voltage of 5-10 keV. Energy dispersive X-ray

spectrum (EDS) is conducted using INCA E2H 250 Xact from Oxford Instruments to confirm the presence of the metal nanostructures.

3.4. Raman Spectroscopy

Raman spectroscopy is vibrational spectroscopy which can provide chemical composition, structure of the material by monitoring the frequency shifts between excitation laser and scattered light.[80] Raman spectra of the known quantity of specific analyte molecules on organic/inorganic hybrid templates are collected. To obtain the limit of detection (LOD) of analytes, characteristic Raman bands of analyte molecules are tracked down. Holoprobe Raman microscope with back-scattered configuration is employed with excitation laser of diode laser (near IR) for organic/inorganic hybrid templates with Au nanoparticles and Au nanorods because the wavelength of near IR laser (785 nm) nearly overlaps the plasmon absorption of organic/inorganic hybrid template resulting in strong electromagnetic field. More than three points are averaged for the consistent spectra of each organic/inorganic hybrid template without accumulation.

For the organic/inorganic hybrid templates decorated with silver and gold nanoparticles, Raman measurements were performed using a WiTec confocal Raman microscope (Alpha 300R) with an Ar^+ ion laser (λ = 514 nm) with 1 mW of intensity of the excitation source according to usual procedure.[81] R6G from water was deposited on the SERS substrates and Raman spectra were collected. Each spectrum was collected with 10 seconds of exposure time and at least three exposures were averaged to ensure accurate spectra were recorded. Mapping images were acquired line by line with an Avalanche photodiode detector in single photon counting mode by fast imaging with a lateral resolution of approximately 250 nm and

a vertical resolution of about 1μm with a 100x objective lens. The 10 μm x 10 μm (x,y) mapping over the large area of the SERS substrate was conducted with a 50x objective lens.

3.5. UV-vis Spectroscopy

The optical properties of noble metal nanostructures originate from LSPR which depends on their size, shape and spatial distribution. Plasmon bands of various metal nanostructures are investigated by UV-vis spectroscopy.[2] To study optical property of organic/inorganic hybrid templates of nanocanal arrays decorated with gold nanoparticles and nanorods, UV-vis absorption spectra are measured by Shimadzu UV-2450 UV-vis spectrophotometer.

Because back-scattered configuration are employed for Raman measurement, measuring transmission spectrum for organic/inorganic hybrid template is important, which can be collected using optical microscope (Leica DM4000M) equipped with a Craig QDI 202 point-shot spectrophotometer. The optical response of the polymeric/inorganic hybrid nanostructure can be measured by UV-vis spectroscopy by monitoring peak position, intensity of plasmon bands. When hybrid nanostructures are exposed to external stimuli, the plasmon resonance spectra are collected by Leica DM4000M. Because the optical response is exposure time dependent, it is important to collect the spectra until the peak shift is saturating. To study the repeatability of and reversibility of the LSPR peak shifts, the sequence needs to be repeated multiple times.

3.6. Atomic Force Microscopy (AFM)

AFM scanning is conducted to show the size and aggregation of the silver nanoparticles on a Dimension 3000-Nanoscope IIIa microscope (Digital Instruments). AFM images were collected in the tapping mode according to the procedures adapted in our lab.[82,83] AFM images of at least several different areas were obtained and the representative image was selected. Silicon nitride tips were used with spring constants of around 50 Nm^{-1} and tip radii between 20~30 nm. AFM scanning was conducted with the rate of 1.0 Hz for surface areas of several microns across.

3.7. X-ray photoelectron spectroscopy (XPS)

XPS is performed on an M-PROBE Surface Science XPS spectrometer using charge neutralization. Spectra were collected from 0 - 1000 eV at 1eV steps at a spot size of 800 um and averaged over 15 scans. To analyze decomposed molecules of HMTD, we perform XPS of HMTD on gold nanoparticles and nanorods clusters with selective coating of PAN before and after laser irradiation (785 nm).

Chapter 4. Nanoporous Membranes with Mixed Nanoclusters for Raman-based Label-Free Monitoring of Peroxide Compounds

4.1. Introduction

The rapid detection of liquid explosives and hazardous chemicals is an urgent need because of the recent security threats and environmental issues. Trace level detection is challenging if the analyte molecules have no specific chemical functionalities, absence of significant light absorption in UV-vis region or strong fluorescence signal.[84] Although infrared and mass spectroscopy techniques have been employed for the detection, these methods are not feasible for in-field use because they are plagued by low sensitivity and slow response. Peroxide-based liquid explosives such as hexamethylenetriperoxidediamine (HMTD) have no color, flavor, tactile characteristics, or functionalities such as amino group or aromatic functional group, which have been used for numerous terrorist attacks. Electrochemical, liquid chromatography with electrospray ionization mass spectroscopy and atmospheric pressure chemical ionization mass spectroscopy,[85,86,87,88] liquid chromatography with fluorescence, and desorption electrospray ionization techniques have been investigated for the trace level detection of HMTD compounds.[84,85, 89 , 90] The critical drawback of chromatographic separation as a sensing application is the long sample preparation time, which makes it not suitable for quick screening and field test. Although the decomposition of a chemical species under laser irradiation depending on laser energy, laser power, and exposure duration is well-known approach it is rarely utilized for trace detection with "field-friendly" SERS technique.[91]

We designed a novel nanoporous SERS-active substrate based on porous PAMs[51,75] decorated with mixed nanoclusters, which demonstrate trace level monitoring of peroxide-based liquid explosive, HMTD (Figure 4.1).[53] The organic/inorganic hybrid templates suggested here are utilizing selective polymer nanocoating within cylindrical nanopores for the capturing of analyte molecules, maximizing surface area and hot spots with efficient light interaction inside nanochannels.[36,37] The mechanism of photolysis of peroxide groups which initiates peroxide bond cleavage generating radicals has been reported by rarely utilized for real-time peroxide monitoring with practically meaningful sensitivity.[92,93]

4.2. Experimental Detail

Polyacrylonitrile (PAN) which was employed as a selective coating on Porous alumina membranes with pore diameter of 250 nm and 60 μm thickness for adsorbing HMTD molecules. PAN was dissolved in N,N-dimethylformide (DMF) at 100 ºC. 0.2 % PAN in DMF solution was spin-cast (4000 rpm, 30 sec) on PAM and rinsed with DMF two times for gold nanorods attachment. Gold nano particles and nanorods solution was filtrated into the porous alumina membrane several times to achieve uniform coating inside PAMs. After this step, 0.1% of PAN in DMF was spin-cast (4000 rpm, 30 sec) one more time.

To collect Raman spectra of HMTD (Accustandard), a Holoprobe Raman microscope with back-scattered configuration using 10x objective lens (A diode laser with 785 nm wavelength) was used. 10μl of HMTD in acetonitrile with desired concentration was dropped and evaporated on 1×1 cm^2 area of the SERS substrate. For each sample, four points were collected with 20 sec acquisition time at different locations and averaged. The peak assignment of the Raman spectra obtained was performed by a computational library,

Advanced Chemistry Development (ACD). The analyte molecules (input to ACD) for assigning the vibrational bands included HMTD, PAN, and CTAB molecules and the possible decomposed compounds and peak positions were verified against standard Raman databases.[94,95]

4.3. Result and Discussion

4.3.1. SERS-active substrate with gold nanorods and nanoparticles

Gold nanorods and nanoparticles have been exploited with gold nanorods possessing several advantages over nanoparticles which can be utilized for sensing application.[96, 97] Longitudinal plasmon band of gold nanorods can be easily tuned by changing the aspect ratio to match the excitation laser for the maximum Raman enhancement.[98] In addition, gold nanorods can be instrumental for the realization of hot spots, since the sharp edges of the individual anorods can give rise to large electromagnetic enhancement. Mixed nanostructures such as gold nanorods combined with nanoparticles have been demonstrated to show even higher SERS enhancement compared to the nanoparticles alone.[99] For SERS applications, the use of ultrathin selective coating would be advantageous on the response time and the sensitivity because most of the adsorbed analytes inside the polymer layer are within SERS active range. It has been known that the local electromagnetic fields exponentially decay with increasing distance from the metal surface.[2] Thus precise control over the ultrathin polymer selective coating is investigated for the desired analytes.

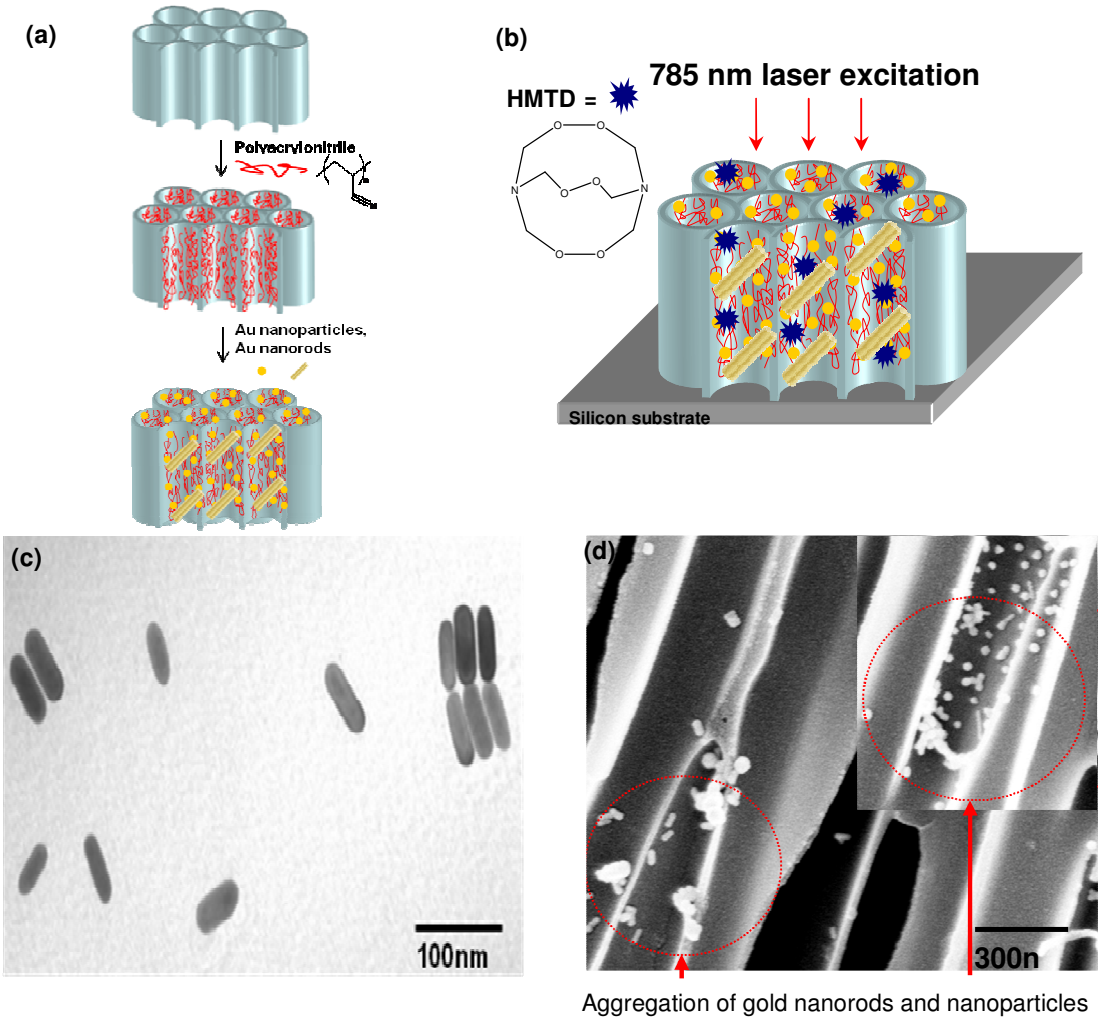

Figure 4.1. (a) Fabrication of 3D porous alumina membrane substrates and (b) chemical detection with Raman spectroscopy. (c) TEM image of gold nanorods synthesized in this study (d) SEM image of fractured porous alumina membrane with mixed gold nanorods and gold nanoparticles.

Gold nanoparticles (about 30 nm in diameter) capped with cetyltrimethylammonium bromide (CTAB) are synthesized by seed growth technique.[72] Gold nanorods are synthesized using seed-mediated growth technique and TEM image of them shows the presence of gold nanorods having aspect ratio of ~4 with the length of 80 ± 8 nm and the width of 19 ± 4 nm (Figure 4.1b). We utilized PAMs with pore diameter of about 250 nm and a thickness of 60

μm for uniform distribution of gold nanorods and particles. If we use PAMs with smaller pore size than that, the active surface area might increase and enhance SERS performance. However, due to the size of gold nanoparticles and nanorods, utilizing PAMs with smaller pore diameter can cause pore blocking during loading and degrade SERS performance. The rationale behind choosing PAMs with a thickness of 60 μm is that the PAMs with thickness smaller than 60 μm are extremely brittle and difficult to handle and do multiple processing steps for chemical modification. On the other hand, due to finite transmission of light in PAM (50% over 60 μm), thicker PAMs are not favorable.

The SEM image of the fractured PAMs loaded with mixed nanoparticles shows that both nanorods and nanoparticles are successfully immobilized on the polymer (PAN) coated side walls of PAMs (Figure 4.1c). We loaded about 32 μmol/cm^3 of mixed gold nanoparticles and gold nanorods into PAM for the best SERS performance as has been concluded in the previous studies, which utilized vacuum filtration method.[118, 100] As we have already demonstrated, further increase in nanoparticles concentration reduces membrane transparency and SERS efficiency.

4.3.2. Comparison of Various 3D Hybrid (organic/inorganic) Templates

Considering very different optical absorption properties of gold nanostructures, we prepared three types of PAMs loaded with various nanostructures: gold nanorods, nanoparticles, and their 1:1 mixtures (Figure 4.2a-c). Apparently, gold nanorods were highly distributed and aggregated in end-to-end orientation through the cylindrical pores of PAMs. In contrast, gold nanoparticles and mixed nanostructures formed clusters with very few (5-10) units in a single cluster. It is well known that the extinction spectrum of the gold anorods solution exhibits two characteristic peaks related to transverse (520 nm) and longitudinal (680 nm)

plasmon resonances (Figure 4.2a). PAM substrate with gold nanoparticles shows its UV-vis extinction peak at 520 nm (Figure 4.2b), whereas substrate with gold nanorods exhibits a peak at 520 nm and a relatively broad peak around 700 nm (Figure 4.2c). UV-vis extinction spectrum of organic/inorganic hybrid template with mixed gold nanorods and nanoparticles exhibits two characteristic peaks from gold nanorods and nanoparticles (Figure 4.2d). In the case of utilizing 785 nm laser as an excitation source, gold nanorods and mixed gold anorods-nanoparticles are expected to provide higher SERS enhancement because the longitudinal plasmon resonance of the nanorods and the coupled plasmon resonance of the aggregated nanoparticles overlaps with the wavelength of the excitation light.

Raman spectra (785 nm of wavelength, 20 mW of power) were obtained from PAMs loaded with various types of nanostructures after deposition of 100 ppm of HMTD solution. The Raman spectra for bare PAMs and PAMs loaded with gold nanoparticles or gold nanorods showed very low intensities (Figure 4.2d). In contrast, the overall intensity of Raman spectra (peak assignment are discussed later) from PAM substrates loaded with mixed gold nanorods and gold nanoparticles is an order of magnitude higher compared to the PAM loaded with gold nanoparticles alone or gold nanorods alone (Figure 4.2d). The enhanced SERS performance of the organic/inorganic hybrid template with mixed gold nanorods and gold nanoparticles might be related to two different effects. Firstly, the wavelength of near IR laser (785 nm) nearly overlaps the plasmon resonance (740 nm) of gold nanorods/nanoparticles SERS substrate resulting in strong electromagnetic field.[99] Secondly, it is known that the multi-shape, multi-size particle aggregates exhibit higher enhancement compared to uniform particle aggregates.[101] Aggregation of the nanoparticles and the nanorods results in “hot” interstices which host extremely large electromagnetic fields and hence large SERS enhancement.

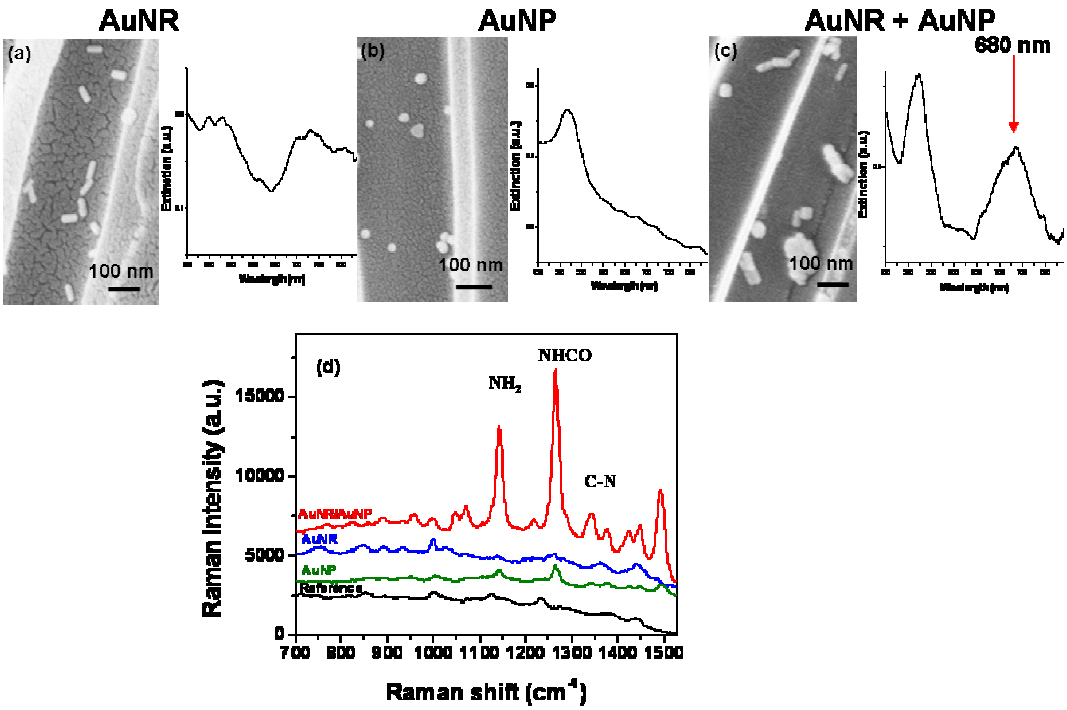

Figure 4.2. (a) SEM images and UV-vis extinction spectra of PAM with gold nanorods, (b) PAM with gold nanoparticles, and (c) PAM with mixed gold nanorods and gold nanoparticles. (d) Comparison of Raman spectra of HMTD obtained with PAM substrates with mixed gold nanorods and gold nanoparticles, gold nanorods, gold nanoparticles, and PAM without HMTD. [118]

For instance, Gunawidjaja et al. has demonstrated that the SERS enhancement from nanowires/nanoparticles hybrid structure (silver nanowires decorated with gold nanoparticles) is nearly two orders higher compared to that for the individual nanoparticles or the nanowires.[102] Even though organic/inorganic hybrid template with gold anorods alone has UV-vis extinction overlapping near 785 nm of wavelength (Figure 6c), the performance of the organic/inorganic hybrid template with gold nanoparticles is better than that for PAMs with gold nanorods alone, which can be explained by the enhancement effect due to the alignment of the aggregated gold nanorods and coupling within gold nanoparticle clusters (Figure 4.2). In fact, gold nanorods are distributed and aggregated in end-to-end orientation through the cylindrical pores of membrane, which is caused by the unidirectional flow of

solution in the course of vacuum filtration (Figure 4.2a). The aggregates of gold nanorods exhibit a red-shift and significant broadening of the longitudinal plasmon peak resulting in weak enhancement (Figure 6c).[10,103]

On the other hand, in the case of gold nanoparticle aggregates the coupled plasmon resonance (nearly 700 nm) is relatively weak but close to the excitation wavelength (785 nm) resulting in much higher SERS enhancement compared to the aggregated nanorods. Such aggregation of the gold nanoparticles is favorable for large SERS enhancement owing to the large capacitive fields in their interstices. In the case of mixed gold nanostructures, gold nanorods do not prefer to be oriented along the canal and form clusters with gold nanoparticles which exhibit red-shift (nearly 720 nm). As a result of this, the coupled plasmon resonances induce a large SERS enhancement well above that observed for individual nanoparticles and aggregates of gold nanoparticles utilized in our previous publications (Figure 6d). [118]

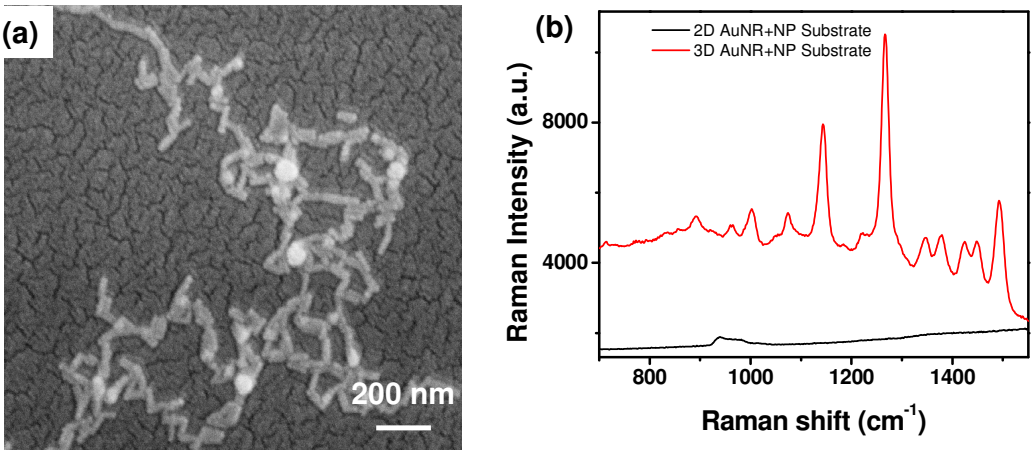

Figure 4.3. (a) SEM image of 2D SERS substrate consisted of gold nanoparticles and gold nanorods (b) Raman spectra of 100 ppm of HMTD on 2D and 3D substrates.

We also compared the 3D and 2D substrates with similar aggregates of gold nanorods and nanoparticles. SEM image shows gold nanorods and gold nanoparticles assembled on a PAN-coated silicon substrate (Figure 4.3a). As has been observed, the planar substrate

showed no significant Raman enhancement even with relatively high concentration of HMTD (100 ppm). This direct comparison underscores the favorable attributes (enhanced surface area, efficient light interaction, and high density of hot spots) of the 3D nanocanal array with mixed gold nanorods and nanoparticles (Figure 4.3b).

4.3.3. Selective Coating for PAMs to Control HMTD Adsorption

Proper selection of the modification routines and materials for PAM chemical modification are critically important for controlling HMTD adsorption from solution. Efficient dispersion of the molecules over the large area requires the modification of the alumina surface with selective coating. As known HMTD is a crystalline solid and it tends to crystallize during the process of solvent evaporation when cast from solution directly on oxide surface thus preventing fine distribution along cylindrical pores (Figure 4.4a).[104] Polyacrylonitrile (PAN) coating is observed to be a good selective coating which suppresses the crystallization and provides means for uniform HMTD adsorption. This is confirmed by simple drop and evaporation test of HMTD demonstrating uniform coverage without any crystallization and aggregation (Figure 4.4b). Thus PAN coating is employed as a selective coating for inner walls of pores in further studies. It is worth noting that gold nanorods and nanoparticles attached to the PAMs have been coated with additional PAN layer with the thickness of about 2 nm. The thickness of the PAN layer, employed here as a protective coating is sufficiently small to preserve the electromagnetic enhancement of the gold nanostructures.[105]

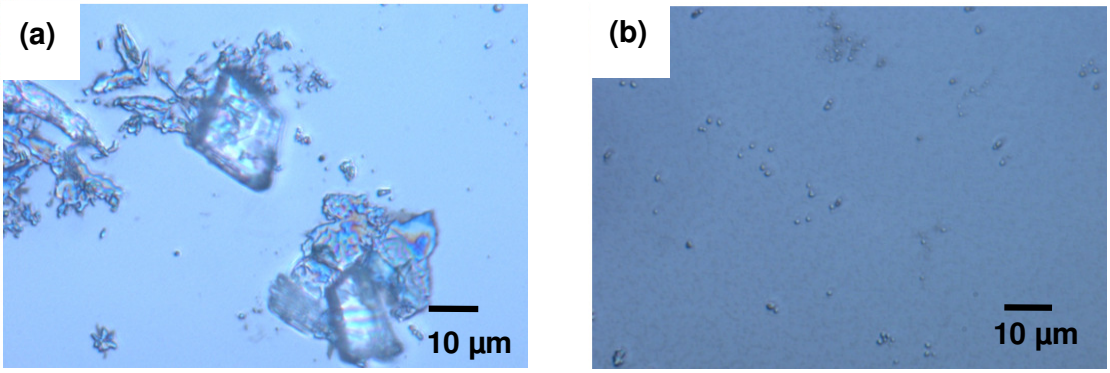

Figure 4.4. Bright field optical images of HMTD (a) on a silicon substrate and (b) on polyacrylonitrile coating.

We suggest that PAN coating is the most appropriate because polar bonds of HMTD molecules tend to withdraw electrons from the nitrogen atoms making C-N-C bonds more electron deficient enabling efficient interaction with electron donating cyanide groups of PAN.[106] HMTD exhibits high solubility in acetonitrile (δ=24.6 $MPa^{1/2}$), thus solubility parameters of HMTD and PAN (δ =25.3 $MPa^{1/2}$) should be very similar. The close values of solubility parameter indicates high partition coefficient between HMTD and PAN providing for easy solubility.

The uniformity of the thin polymer layers as the selective coating and glue layer through the channels of the PAM was confirmed by fluorescent microscope images. We spin coated PAMs with fluorescence labeled 0.2 % of Poly (allylamine hydrochloride (PAH) in water and observed the top, bottom, and cross section of the PAMs, which show almost uniform coating of the polymer layer through the channels of the PAMs (Figure 4.4a, b).

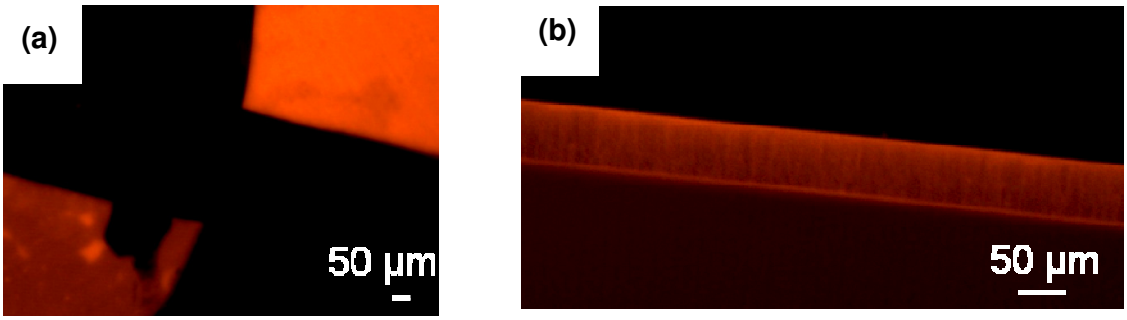

Figure 4.5. Fluorescent microscopy images of the PAMs coated with fluorescence labeled PAH, (a) top and bottom side, (b) cross section of the PAMs

4.3.4. Raman Peaks Assignment

Raman spectra of HMTD (Accustandard) were collected with a Holoprobe Raman microscope (Hololab series 5000 spectrometer, Kaiser Optical Systems) with back-scattered configuration using 10x objective lens. A diode laser with 785 nm wavelength was used as an excitation laser source. 10µl of HMTD in acetonitrile with desired concentration was dropped and evaporated on 1 × 1 cm^2 area of the organic/inorganic hybrid template. For each sample, four points were collected with 20 sec acquisition time at different locations (about 30 µm spot size) and averaged.

The presence of Raman peaks which cannot be assigned to intact HMTD molecules suggests the possibility of either strong interaction between HMTD and selective coating or laser-induced photocatalytic decomposition of HMTD or both (Figure 6d). Because strongly enhanced peaks (1143 cm^{-1}, 1266 cm^{-1}, and 1347 cm^{-1}) do not appear in Raman spectrum of bulk HMTD, we speculate that these drastically enhanced peaks originate from decomposed compounds of HMTD molecules. Thermal decomposition can be considered as the way to verify decomposed materials of HMTD. Indeed, T-jump/FT-IR spectroscopy has been

employed to analyze the thermally decomposed compounds of HMTD.[107] It was found that the decomposed materials are primarily comprised of CO gas (78 mol %), and small amounts of HCN, HNCO, and CH_4. While CO is gaseous product, other solid debris is considered as the major contribution of Raman peaks. As can be seen in Figure 6d, relatively strong peak at 1266 cm^{-1} might arise from the molecules containing HNCO group, and the peak at 1143 cm^{-1} arises from the NH_2 rock.[94,95] Multiple amine vibrations are present between 1310 cm^{-1} and 1360 cm^{-1}.[108,109]

We propose that the strong Raman bands observed here originate from the photodecomposition of HMTD molecules caused by laser-induced bond cleavage as shown in scheme 4.1.

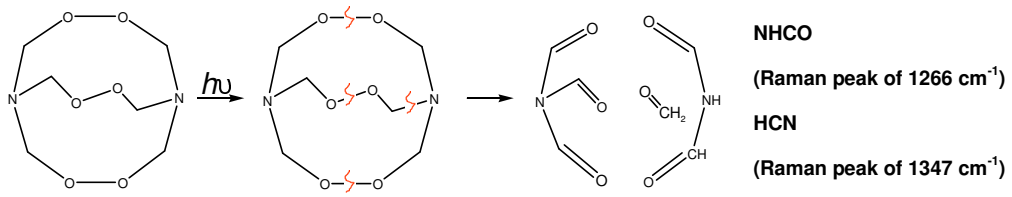

Scheme 4.1. Proposed path for photocatalytic decomposition of HMTD molecules.

Table 4.1. Parameters of various bonds in HTMD molecule.[110]

	Bond length (pm)	Bond energy (kJ/mol)
O-O	148	145
C-C	154	348
C-O	143	360
C-N	147	308
C≡N	116	891

Decomposed fragments can be suggested by considering the possible bond cleavage depending on the specific bond energy level.[107,110] The various bond energies for HMTD molecules (Table 4.1) shows that the lowest bond energy corresponds to O-O (peroxide) bond (145 kJ/mol).[107] Thus, we suggest that photocatalytic reaction due to laser illumination should first result in the cleavage of the peroxide bonds in HMTD, generating radicals (scheme 4.1.).[92,111,112,113] Another possible cleavage could occur on C-N bond (308 kJ/mol), resulting in compounds containing HNCO group, which causes the strong Raman band at 1266 cm^{-1}.[95]

To clarify the decomposed material of HMTD, we perform XPS of HMTD on gold nanoclusters with selective coating before and after laser irradiation (785 nm). The plot in Figure 4.5b shows the XPS spectrum from PAN+AuNP+PAN+HMTD sample and the same after laser irradiation. The XPS spectrum clearly showing the C 1s, O 1s, N 1s, Au 4d5 corresponding to chemical composition of the samples (Figure 4.5).[114] After laser illumination we observed significant increase in oxygen band which indicates intense oxidation processes. Of particular interest is the C 1s band (284.7 eV) of the HMTD after the laser irradiation.

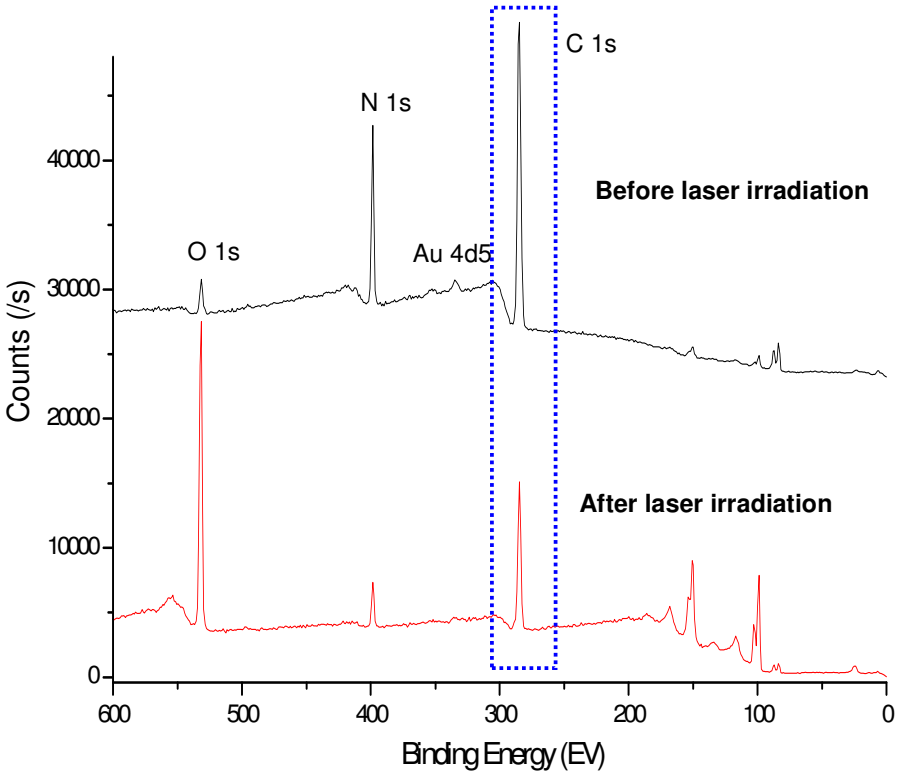

Figure 4.6. XPS spectra of HMTD before and after laser irradiation

After laser illumination, this band shows a weak shoulder at 287.2 eV as opposed to the band before laser irradiation which shows no signs of such shoulder (Figure 4.6a,b). The presence of additional contribution at 287.2 eV indicates the presence of C-NH, CH_2=O, and NH_2-C=O fragments (positions within 287-289 eV) that can only be generated by the O-O and C-N bond cleavage of HMTD molecules, which is the proposed path for the photocatalytic decomposition of HMTD molecule (Scheme 4.1).[114,115]

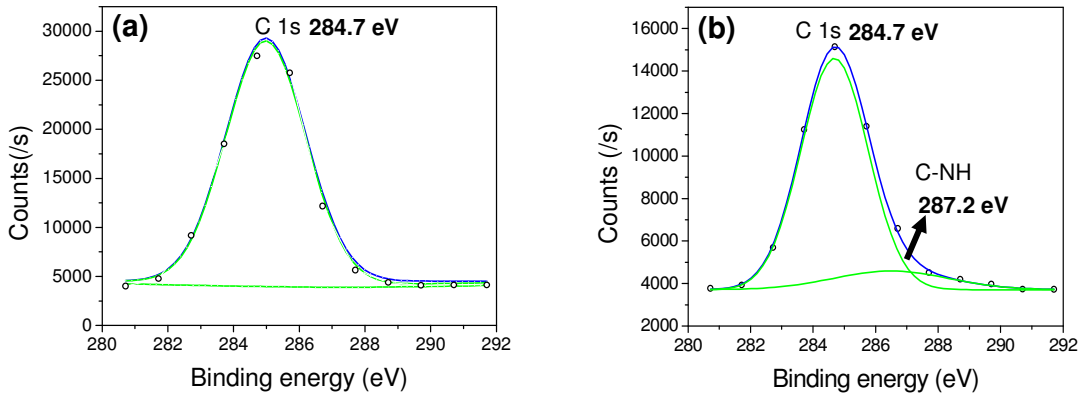

Figure 4.7. XPS spectra of C 1s peak deconvolution of HMTD and assigned bonds (a) before laser irradiation and (b) after laser irradiation

We suggest that the presence of gold nanoparticles and nanorods might augment the photo-initiated decomposition of the HMTD. Indeed, as known, gold nanoparticles exhibit significant photocatalytic activity under laser irradiation.[116] Specifically, the presence of gold nanoparticles causes the increase of quantum yield of photocatalytic decomposition process.[117] To confirm the photocatalytic decomposition of HMTD we monitored the variation of Raman intensity at 1266 cm^{-1} as a function of illumination time at different laser powers (Figure 4.7a). Raman spectra collected every 5 seconds at 10 mW of laser power showed that the intensity of the Raman peak monotonically increases over the first 40 sec followed by saturation. In contrast, when a higher laser power (20 mW) is used, Raman intensity at 1266 cm^{-1} exhibited faster initial increase followed by a decay indicating complete photodecomposition of HMTD fragments (Figure 4.7b). These Raman measurements indicate that HMTD molecules on the gold nanoparticle surfaces can be indeed photocatalytically decomposed by the laser irradiation as has been suggested in related studies.[91]

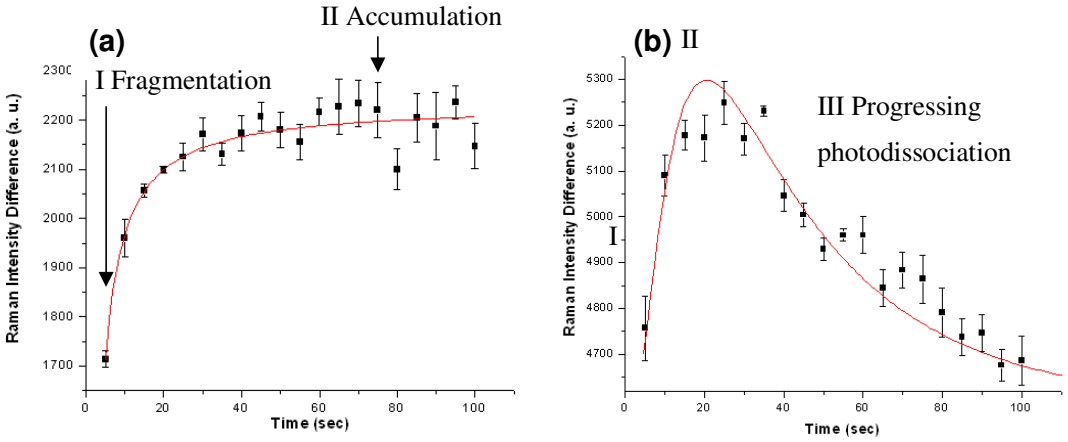

Figure 4.8. The intensity of Raman peak at 1266 cm^{-1} as a function of illumination time with laser power of (a) 10 mW and (b) 20 mW.

4.3.5 Monitoring of Trace Amounts of HMTD

To estimate SERS enhancement and the ultimate chemical sensing with the organic/inorganic hybrid templates, Raman spectra were collected and averaged over four different locations on a 1 cm^2 area of the organic/inorganic hybrid template (Figure 4.8a). Raman spectra showed all major features discussed above with the intensity of the main peak at 1266 cm^{-1} increasing with the increase of HMTD concentration. High resolution spectra in the range 1220-1300 cm^{-1} show a strong peak at 1266 cm^{-1} for HMTD concentrations down to 10 ppm and a relatively weak peak (SNR of ~2) for a concentration of 1 ppm. Interpolating from the SNR at 10 ppm and 1 ppm, we estimate the LOD to be ~3 ppm for a detectable signal to noise ratio of 3+ (Figure 4.8b). This concentration corresponds to about 2 pg of HMTD within the laser footprint (30 μm of diameter). This detectable amount is about three orders of magnitude lower than currently reported LOD, which is 1 ng as determined with mass spectroscopy.[84]

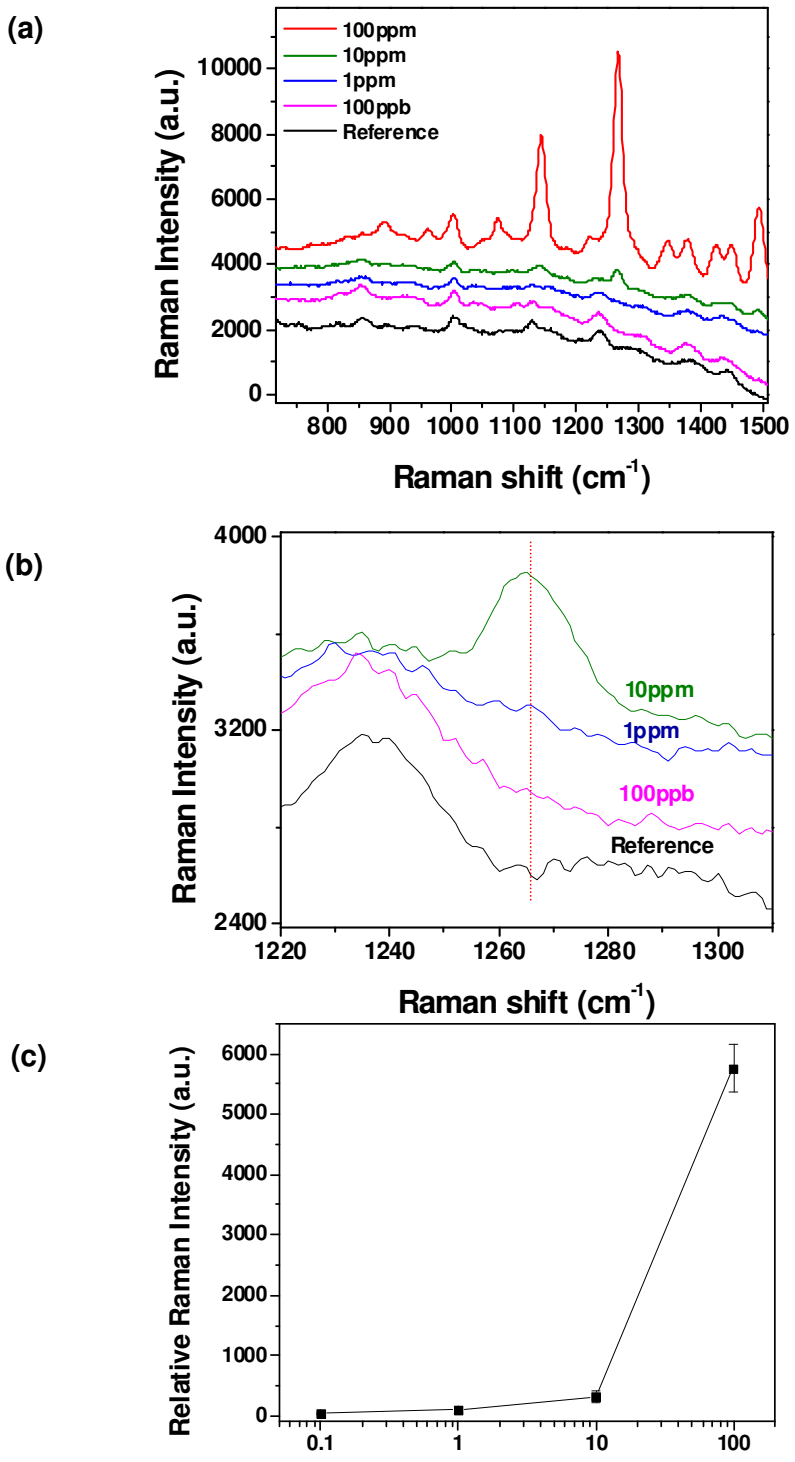

Figure 4.9. (a) Raman spectra of different concentrations of HMTD on SERS substrate coated; reference spectrum is for PAM without HMTD. (b) Raman spectra at 1266 cm-1 with different concentrations of HMTD. (c) Raman intensity at 1266 cm-1 vs. HMTD concentration.

4.4. Conclusions

We demonstrated a novel method for the fast detection of HMTD molecules utilizing photocatalytic decomposition of the molecules and analyzing the resulting chemical fragments using SERS. The SERS-active substrate were successfully fabricated by decorating inner walls of porous membranes with mixed gold nanorods-nanoparticles clusters, which provide "hot spots" with plasmon resonance close to the laser excitation due to the coupling effect. We showed that the 3D PAM substrates can give strongly enhanced Raman signal from the photodecomposed fragments of HMTD providing truly trace detection with sensitivity exceeding that of earlier reports by several orders of magnitude. Our previous study demonstrated organic/inorganic hybrid templates based on nanocanal arrays with Au nanoparticles monitoring the distinctive characteristic Raman bands of dinitrotoluene (DNT) molecules having trace level (10 fg) sensitivity.[118] Raman enhancement factor (EF= $I_{SERS}/I_{Ref}\times[reference]/[sample]$) is the critical values estimated the performance of SERS substrate. We achieved this unprecedented Raman enhancement factor estimated about 10^{10}-10^{12} for DNT, HMTD with our novel 3D SERS-active substrate which is exceeding the current EF compared to other recently reported 3D SERS substrate designs (10^6 - 10^8).[130]

We suggested that the design of robust and inexpensive organic/inorganic hybrid template can be utilized for other peroxide-based explosives or different chemical analytes with simple modification of selective coating and nanostructures. The novel design of organic/inorganic hybrid template combined with photo-dissociation detection approach introduced in this study is highly promising for monitoring of "invisible", unstable, or metastable chemical compounds.

Chapter 5. In Situ Growth of Silver Nanoparticles in Porous Membranes for Surface-Enhanced Raman Scattering

5.1. Introduction

SERS is considered to be one of the most powerful analytical techniques for the detection of chemical and biological analytes because of its high sensitivity, selectivity, rapid response, and prospective portability.[14] Raman enhancement occurs when molecules are adsorbed at the interstices between adjacent metal nanoparticles called hot spots (2-5 nm interparticle gaps) due to the strong electromagnetic field associated with the surface plasmon resonance of metal nanostructures.[8,16] This interparticle plasmon coupling is extremely important for the intense enhancement of the SERS signal from molecules adsorbed at the nanoparticle junctions, providing the capability for single molecule detection.[119] Therefore, the design of well-defined metal nanostructures to maximize the number of hot spots is the most critical aspect to consider in SERS sensor design.[120] To date, numerous studies have been reported on the design of 1D and 2D SERS substrates utilizing metallic and bimetallic nanostructure arrays by precisely controlling the size of nanoparticles and interparticle distances.[55,102,121,122,123,124,125,126,127]

For practical applications of SERS-active substrates, the sensitivity of planar metal structures remains modest due to the limited concentration of hot spots available within the laser-activated footprint. To overcome this obstacle, 3D SERS substrates with advantages including large surface area to maximize the number of hot spots and sites for adsorption of analyte molecules have been demonstrated to have high enhancement. For example, silver nanostructures in the form of nanowires, nanoshettes, and nanoplates have been suggested for

SERS substrates.[127,128,129] Recently, silver nanorod arrays have been designed as SERS substrates using oblique angle vapor deposition.[130] However, these and other random-organized surface structures show limited enhancement, limited mechanical strength, and cannot be easily adapted for microfluidic and stand alone designs. On the other hand, device-friendly and robust designs such as micro-optical fibers were combined with metal nanoparticles for efficient 3D SERS substrates.[39,131] Porous membranes with cylindrical nanopores infiltrated with metal nanoparticles have also been introduced as substrates with high enhancement which is much higher than conventional planar SERS substrates.[51] These substrates can be easily modified for SERS activity, readily reproduced, show excellent mechanical strength and flexibility, cost effective, and can be easily adapted to microfluidic-based and vapor-flow Raman-detection devices.

However, the critical challenge of using these porous membrane substrates or the long hollow microfibers for efficient SERS detection is the difficulty of filling nanosized cylindrical pores with large amount of metal nanoparticles without clogging these nanostructures with usual pore diameter within 100-200 nm. The limited mass transport throughout the continuous microscopic channels requires a channel diameter of several micrometers, which ultimately decreases their efficiency due to the low specific density of hot spots.[42,132] Even though these SERS substrates have shown decent sensitivities, the fabrication method itself is costly and requires multiple complicated steps.

The largest Raman enhancement occurs when the absorption band of the metallic nanostructures is located near the wavelength of the incident laser of the Raman detection setup being used.[71] By tuning the surface plasmon resonance of the nanoparticles (by variation in the shape, size, composition, and aggregation), very strong localized fields can be

achieved at a predetermined wavelength.[133,134] Because silver nanoparticles are considered to be an efficient plasmonic material, they have been widely used as a nanostructure assembly for SERS substrates despite their questionable long-term stability due to modest oxidation.[135] Recently, a well-ordered array of silver nanoparticles grown from gold seeds on a block copolymer template was demonstrated as a possible SERS substrate.[136] However, these and other planar SERS substrates possess a limited concentration of hot spots and some methods require additional plasma etching or other roughening steps.

Here, we have demonstrated the integration of silver nanoparticles by an in situ growth method from electroless-deposited seeds within well-defined PAMs. Thin PAMs with vertical cylindrical pores have already been utilized for the fabrication of 3D silver nanostructure arrays with controlled size and interparticle distance for SERS substrates.[35,137] Our previous study demonstrated PAMs decorated with gold nanoparticles which were fabricated as robust and facile SERS substrates utilizing polyelectrolytes to bind the gold nanoparticles by a vacuum infiltration method. [53]

Compared to this previous approach, the fabrication method introduced here excludes the adhesive polymer layer, which prevents possible overlap of the Raman bands of the polymer and analyte molecules. The in situ seed growth of silver nanoparticles from very fine electroless-deposited nanoseeds is simple, cost effective, and provides a uniform density of nanoparticles along the cylindrical nanopores. This is in contrast with the vacuum infiltration method, which frequently results in the deposition of larger nanoparticles predominantly in the proximity of the top of the PAM surface and with reduced concentration at the bottom of the membrane. The silver nanoparticle-decorated SERS substrates provided efficient interaction between the excitation light source and silver nanoparticle

aggregates dispersed on the inner walls of the PAM when the incident light passed through the cylindrical channel. As the light passes through the channels, multiple reflections can occur resulting in a higher probability of interactions with "hot spots" compared to planar SERS substrates resulting in uniform and efficient SERS properties throughout the entire thickness of the PAM structures.[36,37]

5.2. Experimental detail

Electroless deposition of silver seed nanoparticles inside PAMs: Silver nanoparticles were immobilized on the pore walls of PAMs with an average pore size of 243 ± 20 nm and a thickness of 60 μm by immersing the PAMs in an aqueous solution of $SnCl_2$ (0.02 M) and HCl (0.02 M) for 2 minutes depositing Sn^{2+} on the pore walls. The PAMs were rinsed in Nanopure water and subsequently in acetone and dried. Then the PAMs were immersed in a 0.02 M aqueous solution of $AgNO_3$ for 2 minutes to deposit silver seeds on the pore walls followed by a second washing step. The deposition of silver nanoparticle seeds was carried out three times to provide a high degree of particle coverage on the pore walls.

In situ silver nanoparticles growth: The PAMs were immersed in 1 ml of 10 mM $AgNO_3$ and 0.5 ml of 100 mM ascorbic acid. The PAMs were removed from the solution and rinsed with nanopure water after different time periods. The silver nanoparticles assembled inside the PAMs were characterized by SEM and the size of nanoparticles is determined by AFM height analysis.

5.3. Results and Discussion

5.3.1. Fabrication of 3D SERS substrate with silver nanoparticles and PAMs

Silver seeds were immobilized inside PAMs by electroless deposition as shown in Figure 5.1. Silver nanoparticles with very small sizes were uniformly immobilized along the interior walls of the pores of the PAM by a simple electroless deposition method.[138] The PAM was immersed in an aqueous mixture of $SnCl_2$ and HCl resulting in the deposition of Sn^{2+} on the pore walls. The PAM was then soaked in aqueous $AgNO_3$ solution to reduce silver seeds on the pore walls. This was completed via the reduction of silver on the surface of the pore walls using the following reduction reaction (1) from the salt solution which penetrates through all of the pores.[138]

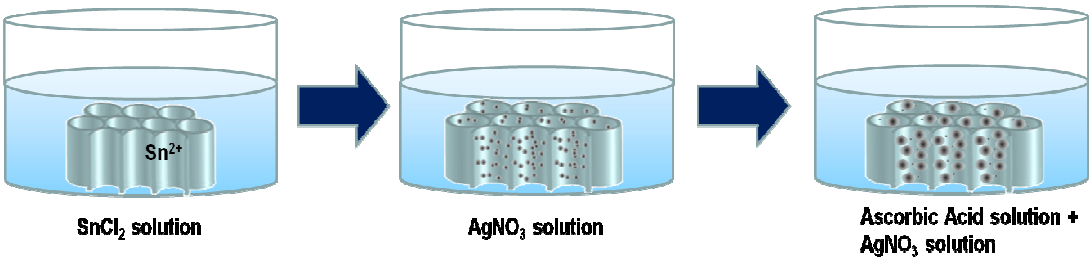

Figure 5.1. In situ growth of silver nanoparticles from electroless-deposited seeds in PAMs utilized in this study.

The silver seed deposition cycle was repeated three times to provide a high density of silver seed particles on the pore walls, which was required for the subsequent in situ growth of silver nanoparticles.

$$Sn^{2+}(aq) + 2\,Ag^{+} \rightarrow Sn^{4+}(aq) + 2\,Ag(s) \qquad 5.1.$$

In situ growth of larger silver nanoparticles was employed to complete the controlled assembly of properly-sized silver nanoparticles on the interior walls of the 3D SERS substrates.[139] Following the electroless deposition of silver seeds on the interior surfaces of

the pores of the PAM, large and highly concentrated silver nanoparticles were formed through a heterogeneous nucleation and growth mechanism.

First, to elucidate the nanostructured morphologies, AFM scanning was conducted to show the size and degree of aggregation of the seeds and corresponding silver nanoparticles formed by in situ growth from electroless-deposited seeds grown on model planar silicon substrate (Figure 5.2). The results of the cross-sectional analysis showed the average size of silver seeds to be about 7 ± 2 nm. When the substrate was exposed to the nanoparticle growth solution, larger silver nanoparticles can be formed with a diameter of several tens of a nanometer as illustrated in Figure 5.2(b) and can be controlled by the kinetics conditions (see below).

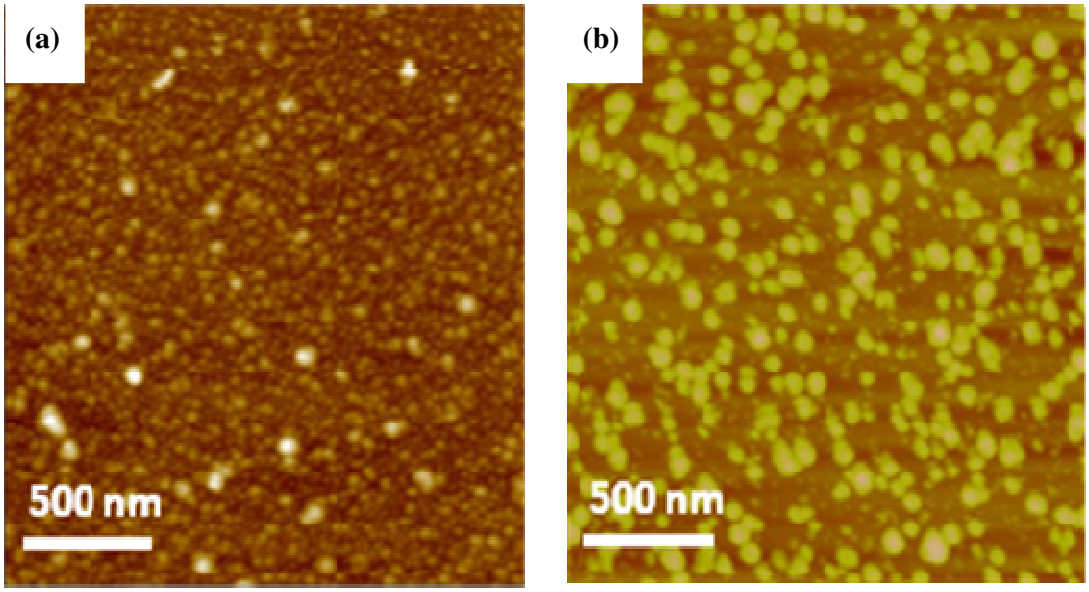

Figure 5.2. (a) AFM images of the electroless-deposited seeds (Z scale = 50 nm) and (b) the silver nanoparticles grown from the seeds (Z scale = 100 nm).

As known, the nucleation and growth process is dependent on several factors including the free energy of the different phases, the concentration of nuclei and growth species in solution, and the surface energy of the growing particles.[140] For homogeneous growth, the growth step is limited only by the diffusion of growing species in the growth media to the surface of the growing particle.[141] In this way, the preliminary seeded wall regions provide controlled growth of silver nanoparticles on the inner pore surface based on the concentration of growth species provided in the solution. Therefore, we investigated the actual size of the silver nanoparticles grown within the pores of the PAM. The size of the silver nanoparticles grown inside of PAM substrates was controlled by the time of particle growth at a fixed concentration of growth media.

The changes in morphologies were monitored by SEM to understand the kinetics of nanoparticle growth under confined pore conditions. The SEM images show the time-dependence of the in situ growth of silver nanoparticles from electroless-deposited seeds inside the PAM template following exposure to a growth solution (an aqueous mixture of $AgNO_3$ and ascorbic acid) (Figure 5.3 and Figure 5.4).[139] The top-view through the cylindrical pores as well as the internal view of pores on fractured PAMs are presented to show the distribution of silver nanoparticles in different parts of the membrane.

To measure the SERS activity of silver nanoparticles decorating the PAMs at various in situ growth times, an aqueous solution of 10^{-5} M Rhodamine 6G (R6G) was deposited on each SERS substrate (Figure 5.6). For Raman measurement, an excitation laser source of 514 nm was employed due to the plasmon absorption of the PAM substrates containing silver nanoparticles. These substrates are expected to provide strong SERS enhancement because

the coupled plasmon resonance of the aggregated silver nanoparticles nearly overlaps with the wavelength of the excitation laser.

As clear from these images, solution growth for 10 minutes generates fairly small nanoparticles with a diameter of 20 ± 5 nm silver nanoparticles (Figure 5.3(a), 5.4(a)). The EDS of the SERS substrate confirms the presence of silver nanoparticles inside the PAM substrates (Figure 5.5). It was observed that allowing more time for silver nanoparticle growth resulted in a gradual increase in the size of the nanoparticles formed inside the PAM mostly within the initial 30 minutes. 40 ± 10 nm silver nanoparticles were uniformly formed on the wall of PAM after 20 minutes of growth as shown in Figure 5.3(b), 5.4(b). Finally, 60 ± 10 nm silver nanoparticles were obtained after 30 minutes of growing in solution (Figure 5.3(c), 5.4(c)). At longer times, the size of nanoparticles increased beyond the useful limit for SERS and these larger (>70 nm) nanoparticles clogged the pores with the average diameter of about 240 nm.

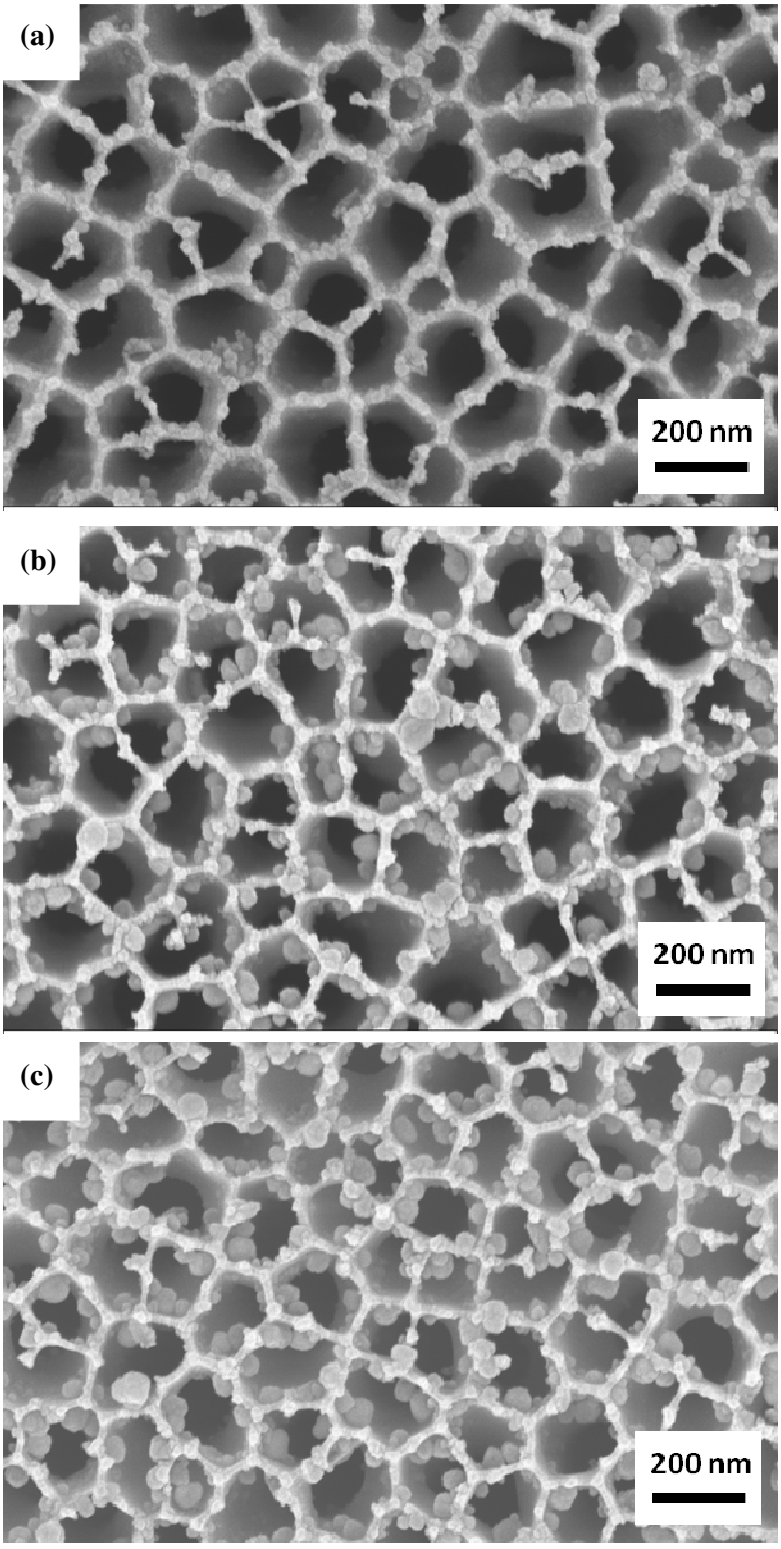

Figure 5.3. Top view SEM images of time dependent in situ growth of silver nanoparticles from electroless- deposited seeds in PAMs. (a) 10 min (b) 20 min, and (c) 30 min of growth time of silver nanoparticles from electroless-deposited silver seed in PAMs.

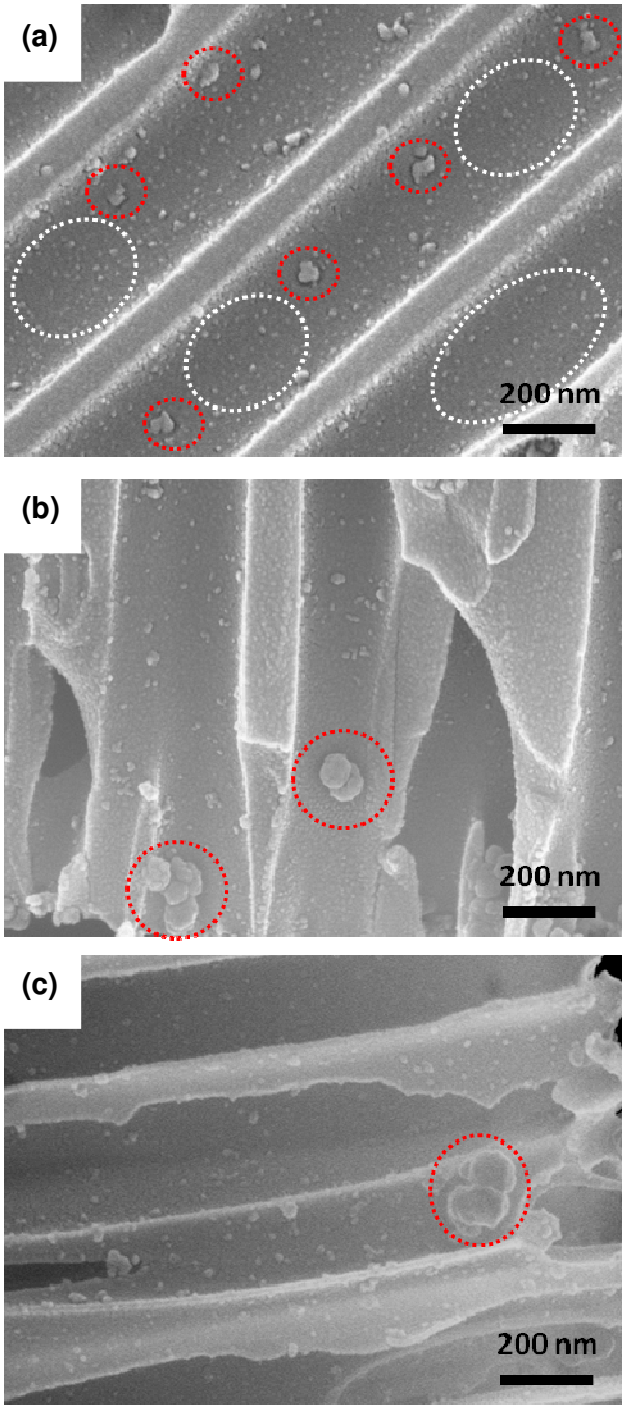

Figure 5.4. Cross-sectional SEM images of time-dependent in situ growth of silver nanoparticles from electroless- deposited seeds in PAMs. (a) 10 min (b) 20 min, and (c) 30 min of growth time of silver nanoparticles from electroless-deposited silver seed in PAMs. Electroless-deposited silver nuclei are marked with white ellipses and in situ grown silver nanoparticles are marked with red circles.

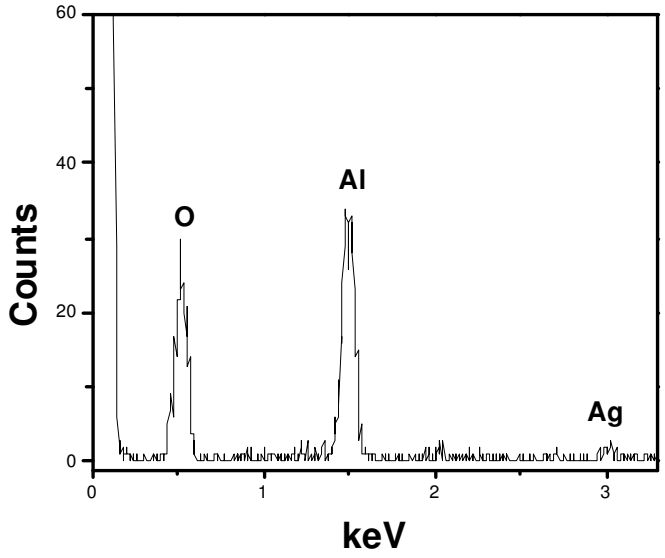

Figure 5.5. EDS spectrum of porous alumina membrane with grown silver nanoparticles.

5.3.2. Raman enhancement of 3D controlled assembly of silver nanoparticles

From the comparison of relative Raman intensities of each SERS substrate, the substrate containing silver nanoparticles grown for 25-30 minutes was observed to provide the largest SERS enhancement (Figure 5.6). Under these conditions, silver nanoparticles with diameters of 40-60 nm were grown inside PAM pores and utilized for further studies. The plasmon resonance properties of spherical metal nanoparticles are dependent on their size and level of aggregation, thus controlling the size of silver nanoparticle is critical for SERS enhancement because the enhancement effect is highly localized and decays rapidly as the interparticle distance increases.[7,142]

The aggregated silver nanoparticles of 40-60 nm on the SERS substrate were found to provide the optimum conditions for the largest SERS enhancement.

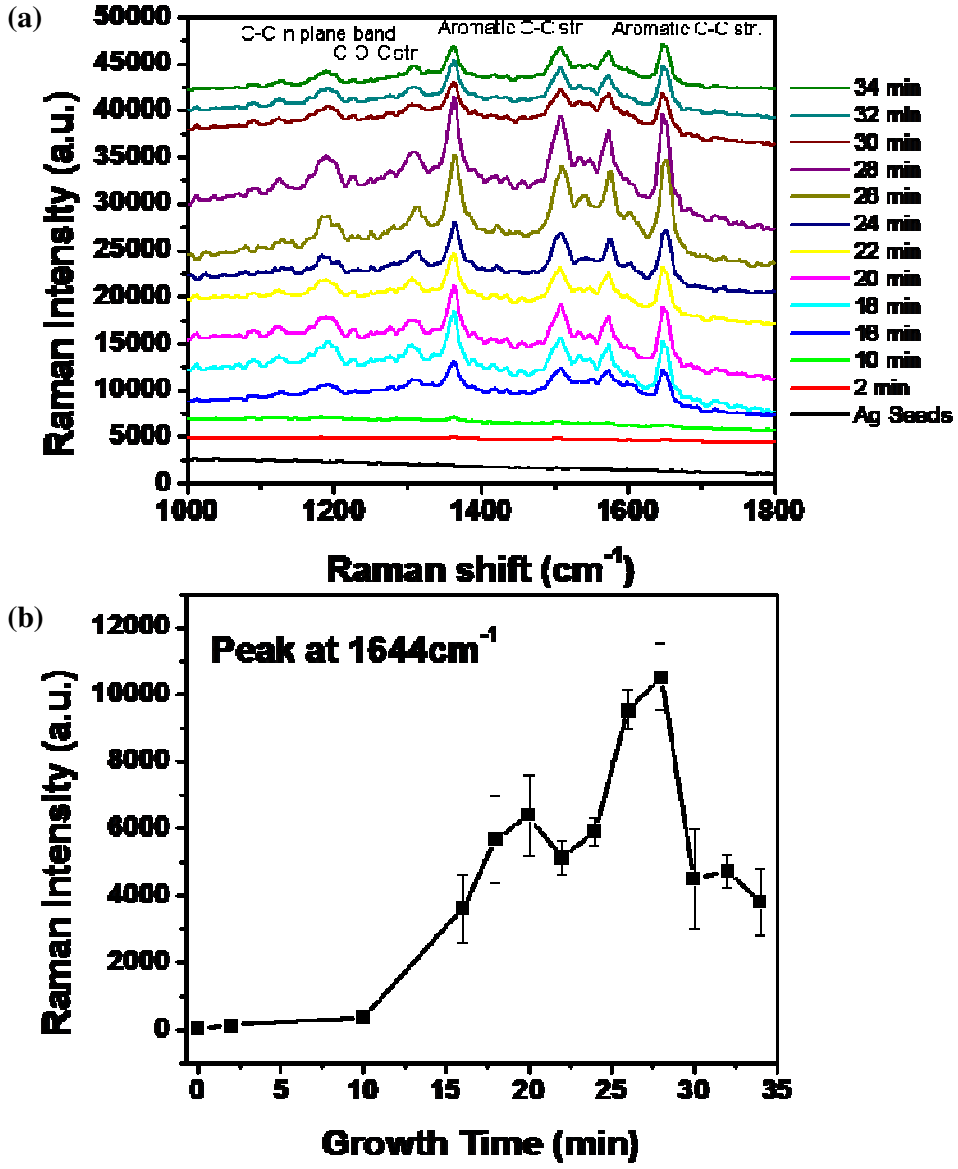

Figure 5.6. (a) Raman spectra of R6G on silver nanoparticles/PAM at various silver nanoparticle growing periods, (b) relative Raman intensity of 1644 cm^{-1} at different nanoparticle growth times.

5.3.3. Optical properties of PAMs with silver nanoparticles

Higher SERS enhancement can be achieved when the coupled plasmon resonance of the aggregated silver nanoparticles assembled in the PAMs overlaps with the wavelength of the excitation light.[99] Thus, UV-vis absorption spectra were collected from several different substrates fabricated with various nanoparticle growth times.

As shown in Figure 5.7(a, b), the growth of the silver nanoparticles resulted in a higher degree of aggregation of silver nanoparticles, which has been shown to cause a red shift of the plasmon band.[143,144,145] The UV-vis absorption spectrum of the SERS substrate which contained silver nanoparticles grown for about 28 minutes shows an absorption band around 514 nm, which is close to the wavelength of the incident light. This average size was selected because as has been shown for the absorption band of metallic nanostructures close to the wavelength of the exciting light, the largest Raman enhancement occurs.

As the silver nanoparticle size increased as discussed above, the plasmon band of the aggregated structures shifted closer toward the excitation wavelength, which corresponded to an increase of the measured SERS enhancement. When the silver nanoparticles were grown for more than 28 minutes, the UV-vis absorption spectra were red-shifted to wavelengths longer than that of the incident light (Figure 5.7a, b). Therefore, a decrease in the SERS enhancement should be expected under these conditions. As a result, this specific growth time under our fabrication conditions provides optimum nanoparticle densities, level of aggregation of nanoparticles, and plasmon band position for maximum SERS enhancement and thus was exploited for SERS studies.

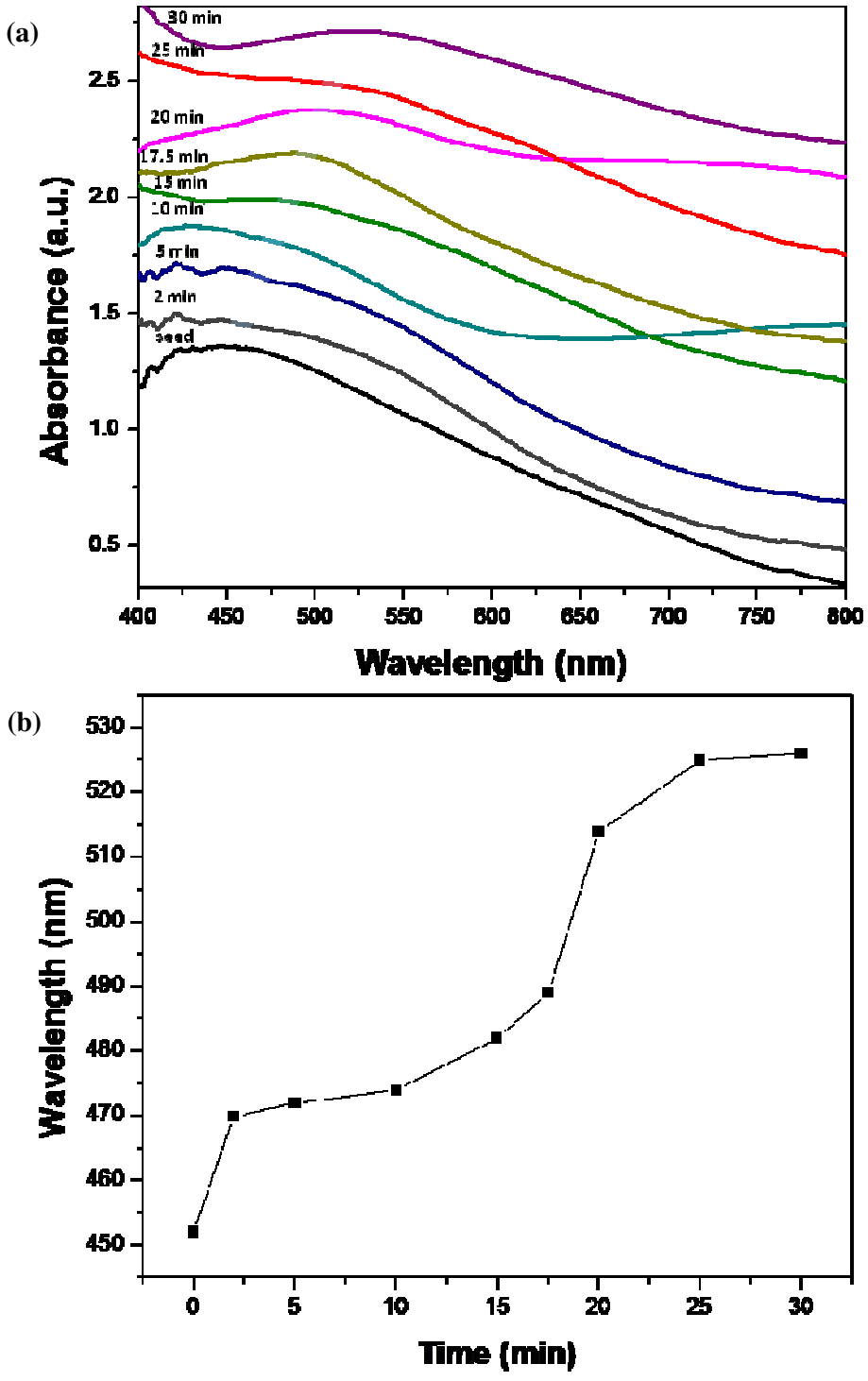

Figure 5.7. (a) Several representative UV-vis absorption spectra of *in situ* growth of silver nanoparticles from electroless deposited seeds in PAMs, (b) UV-vis absorption peaks of SERS substrates at different nanoparticle growth times.

Figure 5.8. shows the relationship between the surface plasmon band of the metal nanostructure and the wavelength of the excitation laser for maximum SERS. The maximum SERS occurs when the λ_{LSPR} of the metal nanostructures lies between the λ_{ex} (excitation wavelength) and λ_{vib} (particular vibrational band of the analyte molecule, in this case correlating to 1644 cm^{-1} for R6G and 1266 cm^{-1} for HMTD).

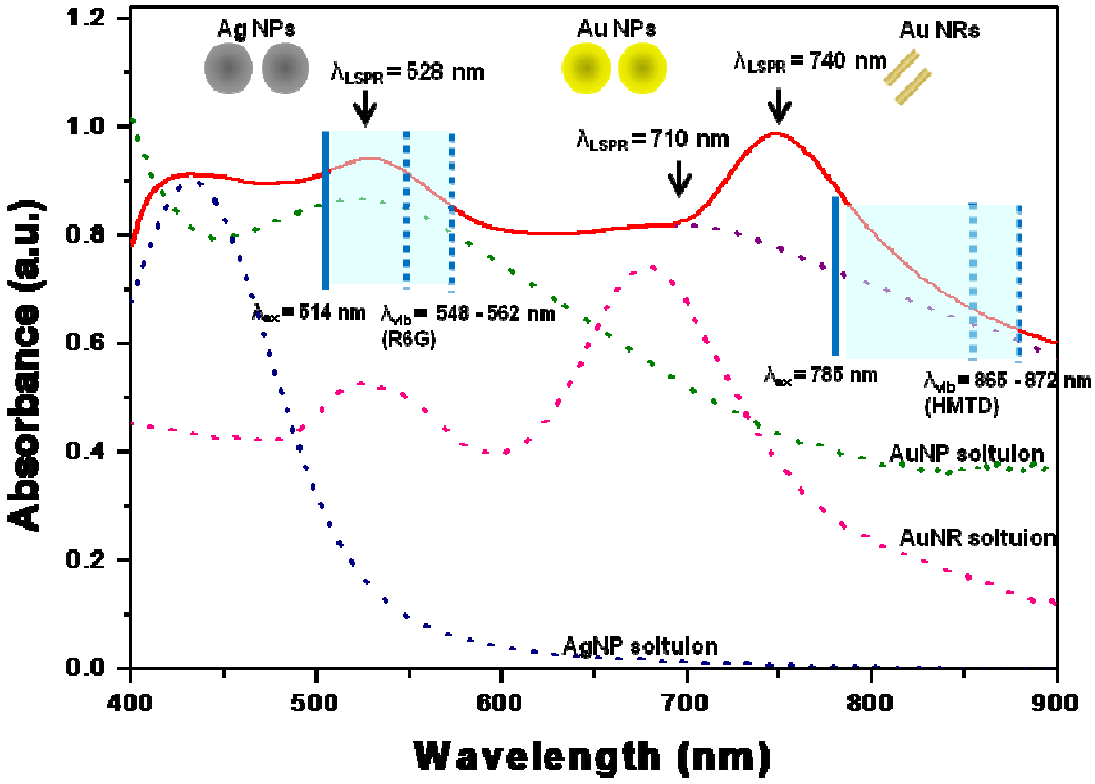

Figure 5.8. Representative UV-vis absorption data showing a shift in the absorbance of the silver, gold nanoparticles, gold nanorods following aggregation in PAMs. The blue lines indicate the spectral range which will allow for the highest intensity SERS spectrum of R6G using a 514 nm laser, HMTD using a 785 nm laser using equations 5.2 and 5.3.

$$\Delta\nu_{vac} = \nu_{vac} + \delta - \frac{1}{\lambda_{air}} \qquad 5.2.$$

$$\lambda_{LSPR} \approx \lambda_{ex} + \frac{\lambda_{vib} - \lambda_{ex}}{3} \qquad 5.3.$$

The vibrational wavelength of the analyte peak range (λ_{air}) can be calculated from equation 5.2, where $\Delta\nu_{vac}$ is the Raman peak location, ν_{vac} is the wavenumber of the excitation laser source, and δ is the correction factor. The correction factor is ignored in our calculations because it is on the same order (~5 cm^{-1}) of the error associated with the grating (600g/mm) of our Raman system and the correction factor does significantly contribute to the Raman peak location of the analyte.

We have adopted a useful expression (equation 5.3) which allows for the estimation of the necessary location for the plasmon resonance band peak (λ_{LSPR}) of the metallic nanostructures of the SERS substrate. This equation is based on previous experimental results of our group as well as literature values, which show that the λ_{LSPR} needs to be located approximately 1/3 of the distance between the excitation wavelength and the wavelength associated with the Raman peak of the analyte.[71] Therefore, silver nanoparticles assembled in PAM (λ_{LSPR} =528 nm) showed strong SERS enhancement from R6G molecules. Although assembled gold nanoparticles and nanorods in PAM showed their λ_{LSPR} at 740 nm, the resulting SERS enhancement from HMTD molecules was large enough because the plasmon resonance bands still nearly overlap with the λ_{ex} of 785 nm. This equation provides the necessary background information needed to intelligently guide experiments to achieve optimal SERS enhancement of each specific analyte.

5.3.4. SERS characteristics of PAMs with silver nanoparticles

To show the uniformity of the SERS phenomenon over a large area of the 3D assembled silver nanoparticles in the PAMs, Raman mapping of the SERS intensity was conducted using a well-known Raman analyte, Rhodamine 6G (R6G). [146] To conduct these measurements, the SERS substrates were immersed in an aqueous solution of 10^{-5} M R6G, rinsed thoroughly with Nanopure water, and SERS spectra of the substrates were collected. Characteristic Raman bands of R6G (1360, 1504, and 1644 cm^{-1}) from aromatic benzene rings were strongly enhanced by the silver nanoparticle PAM (Figure 5.6).[147] The intensity of Raman band at 1644 cm^{-1} was mapped all over the surface (x, y) and through the entire depth (z) of the PAM.

The 10 µm x 10 µm (x, y) mapping of the relative intensity of the 1644 cm^{-1} Raman band of R6G indicates that relatively uniform SERS enhancement occurs over the large area of the substrate with modest deviations in SERS intensity not exceeding ± 30% with a 1 second acquisition time and pixel size below 200 nm (Figure 5.8). It can be seen that there are brighter areas on the mapped surface as shown in Figure 5.9(a), indicating that the aggregation of several nanoparticles on the surface can cause a greater SERS enhancement in some areas. However, most of the mapped surface appears bright on the SERS substrate indicating that SERS enhancement occurs consistently over the entire large area.

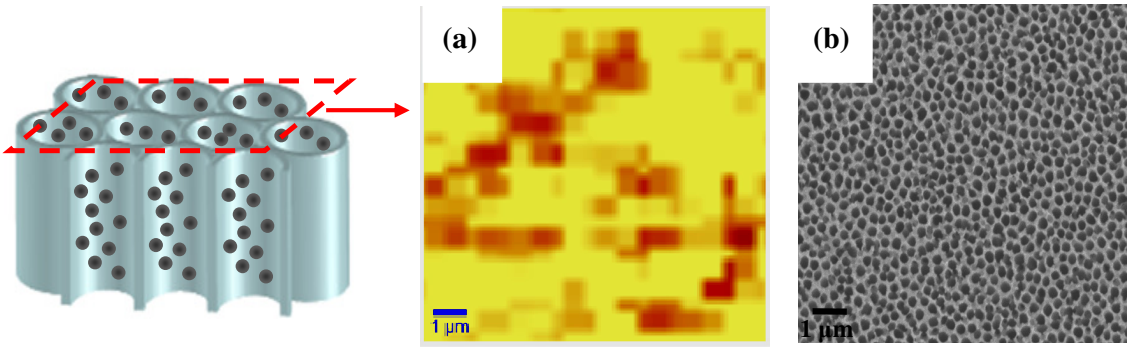

Figure 5.9. (a) Raman mapping of the 1644 cm^{-1} peak (R6G) in the lateral direction over a 10 µm x 10 µm area of the PAM and (b) corresponding SEM image. The range of relative Raman signal intensity, Z = 0~1400 a.u.

To observe the SERS intensity through the pores of the 3D assembled silver nanoparticles within the PAM substrate, Raman mapping in the (z) direction was conducted as well with a 0.5 second acquisition time (Figure 5.10). It is worth noting that both sides of the PAM were mapped because the commercial PAM utilized in this study has varying pore wall thickness (about 10 nm difference) on each side of the membrane (Figure 5.10). The largest SERS enhancement was observed in the first 20 µm in depth from the surface on both sides of the SERS substrate (Figure 5.10a, b). The Raman signal intensity of R6G from the SERS substrate fades after a depth of 20 µm from the surface. SERS intensity distribution was only slightly affected by the slight difference in the pore wall thickness (Figure 5.10). We suggest that this phenomenon can be attributed to the absorption of the incident laser light inside the PAM channel more than 20 µm in depth from the surface effectively decreasing the SERS enhancement through the channel.[118]

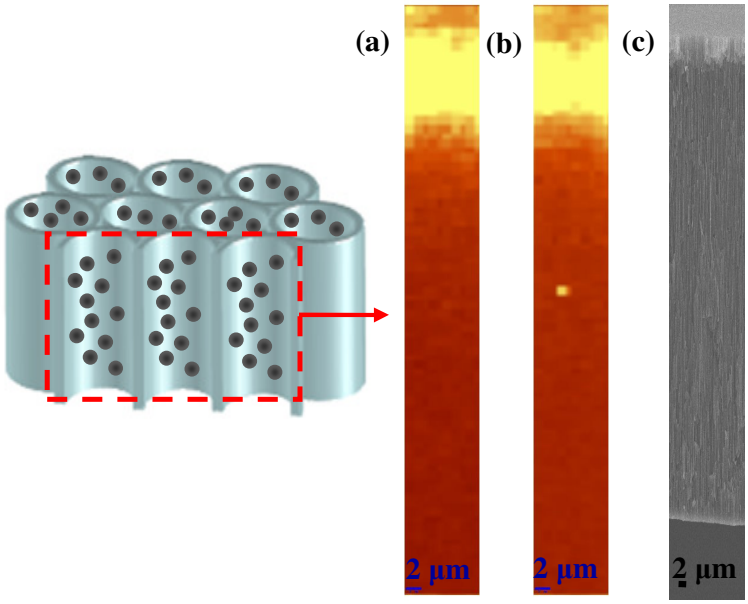

Figure 5.10. Raman mapping of the 1644 cm^{-1} peak in the Z-direction over a 10 µm x 80 µm area of PAMs. The range of relative Raman signal intensity, Z = 0~600 a.u.

To compare the Raman enhancement of the SERS substrate fabricated by the in situ growth of silver nanoparticles with a SERS substrate fabricated by the vacuum infiltration of silver nanoparticles combined with a polyelectrolyte binding layer,[51] we deposited the same volume of R6G solution (with 10^{-5} M concentration) on both SERS substrates and conducted comparative SERS measurements under identical conditions.

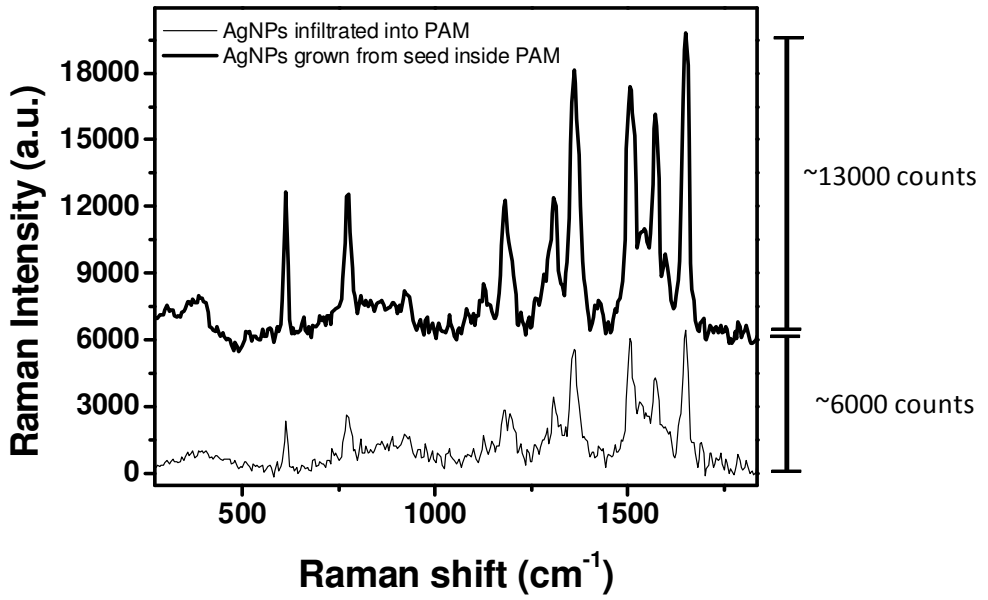

Figure 5.11. Raman spectra of R6G on PAM with *in situ* grown and conventional vacuum infiltrated silver nanoparticles.

As can be concluded from this direct comparison, the SERS substrate fabricated via the in situ growth of silver nanoparticles within the PAM showed almost twice as strong of Raman enhancement compared to the SERS substrate fabricated by vacuum infiltration (Figure 5.11). This significant increase indicates that the fabrication method of in situ growth introduced here can generate a more uniform silver nanoparticle distribution along the 3D channels of the PAMs resulting in increased SERS enhancement (Figure 5.11). The fabrication of large areas of SERS substrates by the in situ growth method is simpler and faster than by the vacuum infiltration method.[118] Also, SERS substrates fabricated by the in situ growth of silver nanoparticles do not include a polyelectrolyte binding layer, which can be better for sensing applications because it is not necessary to separate the Raman bands of the polyelectrolyte binding layer from those of the desired analyte.

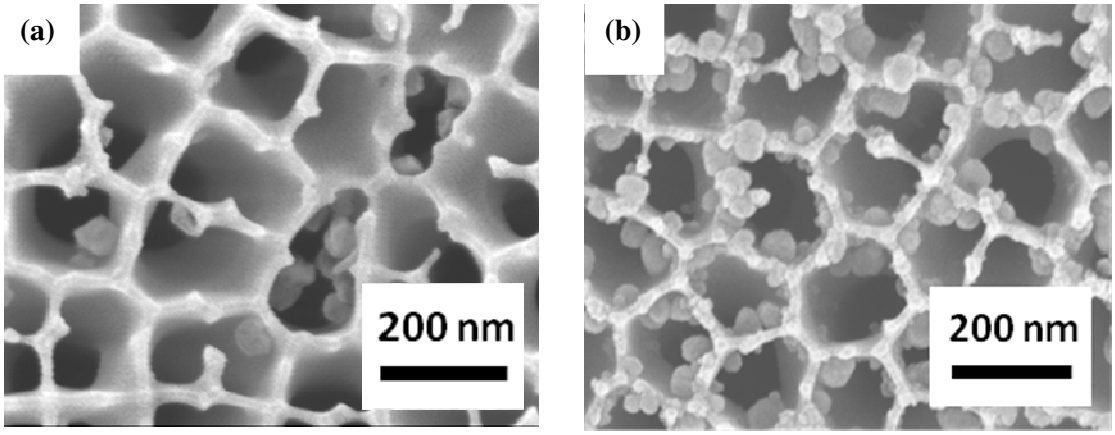

Figure 5.12. SEM images of (a) SERS substrate consisted of silver nanoparticles infiltrated into PAMs, (b) SERS substrate consisted of silver nanoparticles grown from electroless deposited seeds inside PAMs

Finally, we conducted preliminary observations of long-term stability of our SERS PAM structures and their prospective shelf-life under ambient laboratory conditions with more rigorous research for different storage conditions to be conducted in forthcoming studies. In this study, PAM substrates were stored in a sealed vial and their SERS properties were tested after different shelf times. This preliminary testing demonstrated that SERS activity of substrates is mostly preserved within two weeks after substrate preparation, which indicates slow oxidation of silver nanoparticles confined inside PAM nanopores.

To demonstrate our SERS substrate for actual hazardous chemical detection, we selected perchlorate as the analytes. "Perchlorate" is the salt derived from perchloric acid ($HClO_4$) used as an oxidizer in rocket fuel and explosives. The perchlorate ions (ClO_4^-) are adsorbed onto metal surfaces such as Ag, Cu surface resulting in the formation of Ag-ClO_4 and Cu–ClO_4.[148] Therefore, Ag nanoparticle clusters were directly employed for selective adsorption and detection of perchlorate. As shown in Figure 5.13, we could detect 10 ppb level of perchlorate. Even though this value of LOD is couple orders of magnitude higher than previous study which utilized mixture of nanoparticles and analytes, the previous

method requires additional waiting time until complete dry of nanoparticle solution, perchlorate can be directly applied onto the SERS substrate and analyzed.[149]

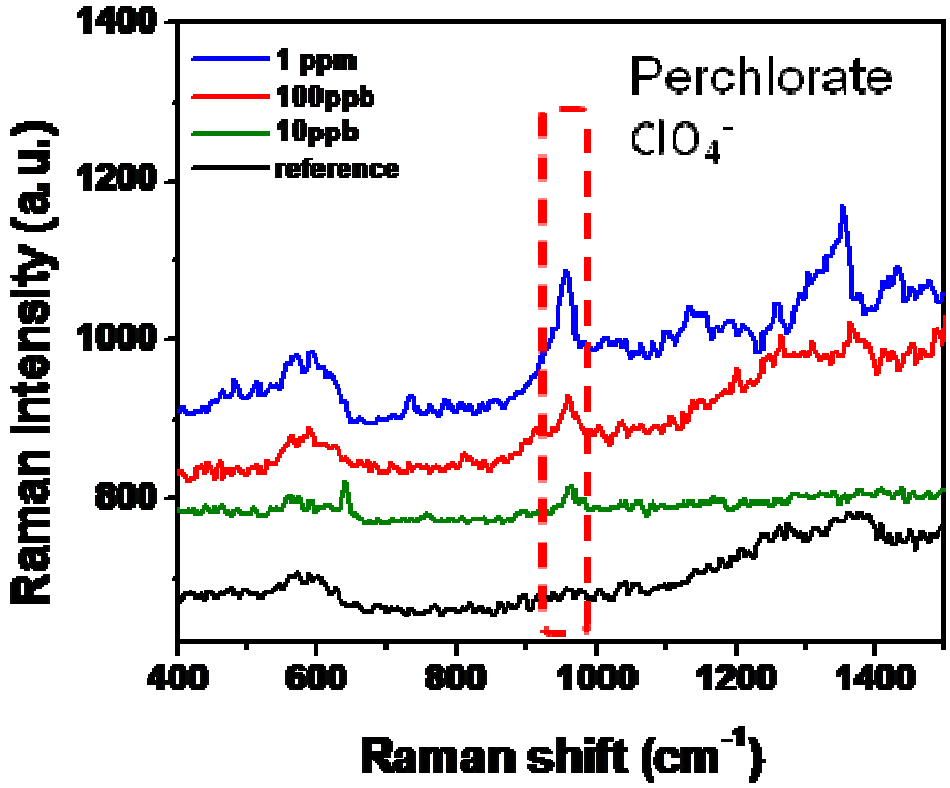

Figure 5.13. Raman spectra of different concentrations of perchlorates on SERS substrate, reference spectrum is for PAM without perchlorates.

5.4. Conclusions

In conclusion, we have demonstrated an efficient way to assemble silver nanoparticles within PAMs without clogging by taking advantage of uniformly-deposited silver seeds from the electroless deposition method for use as an efficient SERS substrate. The silver nanoparticle-decorated porous structures with high concentration and uniform distribution of

nanoparticles were fabricated by a simple and fast method, which provided uniformly-controlled size of silver nanoparticles over the large surface area of the interior pore walls of the PAMs. In situ grown silver nanoparticles were assembled to provide the optimal size of the nanoparticles necessary for large SERS enhancement. The SERS enhancement and optical properties of the silver nanoparticle-decorated PAMs can be controlled by growth conditions in the PAM nanopores. These silver nanoparticle-filled cylindrical pores can be utilized as promising SERS substrates by taking advantage of the efficient light interaction with uniformly-distributed nanoparticles along the interior walls of the PAMs. The SERS substrate can be utilized for the direct and fast detection of hazardous chemical such as perchlorate demonstrating 10 ppb level of LOD. Based on this study, 3D silver nanoparticles assembly with porous membrane can be promising for the trace level detection which can be integrated into microfluidic device.

Chapter 6. Addressable Raman Markers from Silver Nanowire Crossbars

6.1. Introduction

Several recent examples of label-free Raman markers from metallic/bimetallic nanostructures include silver nanowires and their bundles,[32,78,150] silver nanocubes and nanoplates, [127,151] rods with fabricated gaps,[152] nanodumbbells,[121] gold nanowire-gold nanoparticles,[153,154] crossed gold nanowires,[155] ZnO nanowire-silver nanoparticles hybrid nanotrees,[156,157] and silver-gold nanocobs.[102] Efficient SERS phenomena have been observed for crossed silver nanowires and for pre-fabricated bundles with localized nanojunctions. Moreover, intriguing polarization-dependent SERS phenomenon which can be utilized for waveguiding and controlled longitudinal surface plasmon localization have been demonstrated for silver nanowires decorated with multiple nanoparticles and their clusters.[102,158] However, examples of single nanoparticle-based hot spots with SERS appearance tuned by the polarization-dependent excitation conditions are rarely demonstrated.

Here, we report on remarkable properties of crossbars of silver nanowires partially decorated with spherical silver nanoparticles associated with optical turning on/off SERS hot spots mediated by polarization conditions at a nanojunction. Massive fabrication can be achieved via double-step transversal capillary transfer microprinting approach. Such addressable on/off behavior is controlled by the rotation of the polarization plane which excites transversal plasmon resonances and initiates selective excitation of SERS hot spots. We demonstrated the possibility of massive fabrication of such junctions by simple, double-step capillary transfer lithography [159 , 160] which might open a path for large-scale assay applications.

6.2. Experimental Section

Silver nanowires were synthesized according to the polyol method introduced by Xia *et al.* using silver nitrate as the precursor, poly(vinylpyrrolidone) (0.36M concentration and molecular weight, M_n = 1,300,000 g mol^{-1}), as the capping agent, and ethylene glycol as the solvent and reducing agent.[161] A solution (60 mL) of PVP in ethylene glycol was heated at 160 °C under constant stirring for 1 h. Next, a separate solution (30 mL) of silver nitrate in ethylene glycol ($AgNO_3$, 0.12 M) was prepared at room temperature with vigorous stirring. $Fe(acac)_3$ (50 μg) in ethylene glycol solution (0.5 mL) was added to the hot PVP solution, followed by dropwise addition of the homogeneous silver nitrate solution. The solution mixture was stirred for 1 h, or until the solution turned opaque gray.

The formation of silver nanowires could be easily confirmed from optical microscope with 20x or 50x objectives, which is best observed in the dark-field mode. The product is a mixture of silver nanowires and spherical nanoparticles. The silver nanowires were mostly isolated from spherical nanoparticles by multiple centrifugation (3,300 rpm) and re-dispersion in methanol. For the purpose of this experiment, the silver nanowires were only gone through twice centrifugation and re-dispersion cycle to maintain certain concentration of spherical silver nanoparticles, which gives silver nanowire/spherical nanoparticle mixture.

To prepare crossbar arrays of silver nanowires on silicon substrate, sacrificial polymer (PS) micropatterns (Janssen Chimica Mw = 250,000) was used as guided templates for the deposition of silver nanowires. We first drop-casted silver nanowire solution (1-3 mg/mL in methanol) onto the array of narrow channels composed of a sacrificial PS

micropattern (ridges with 3 μm periodicity and 1 μm height) to prepare parallel arrays of silver nanowires. The 1 μm thick sacrificial PS micropattern is deposited on silicon substrate by a polydimethylsiloxane (PDMS) stamp. After deposition of silver nanowires, the PS pattern was lifted off in toluene leaving patterned stripe arrays of silver nanowires. We repeated the process of PS micropatterns perpendicular to the first layer of silver nanowire arrays to prepare crossed arrays of silver nanowires.

Confocal Raman mapping of crossbar array of silver nanowires with the highest resolution (360 nm × 360 nm spot size, 1.7 mW) at peak of 1600 cm^{-1} is conducted at different polarization directions (0°, 45°, 90°, 135°,180°).[81] The relative intensity of specific Raman band at 1644 cm^{-1} from 10^{-5} M of Rhodamine 6 G was monitored and plotted at each 10^{o} of polarization orientation

6.3. Results and Discussion

6.3.1. Fabrication of silver nanowire crossbar assembly

The silver nanowires exploited in this study were obtained according to well-established procedure with optimization of chemical composition to obtain predominantly nanowires with a minor content of nanoparticles (see Experimental).[161] The resulting product was a mixture of silver nanowires and spherical nanoparticles. The silver nanowires were isolated from spherical nanoparticles by multiple centrifugation (3,000 rpm) and redispersion in methanol.

For the purpose of this experiment, the silver nanowires were only exposed to twice centrifugation and redispersion cycle to maintain certain concentration of spherical silver nanoparticles, which gives silver nanowires/spherical silver nanoparticles mixture.[162,163,164,165,166,167] These 5 μm long silver nanowires with a diameter of 120 nm, due to the synthetic procedure, are capped monolayer of polyvinyl pyrrolidone (PVP) as suggested earlier.[168] Indeed, a direct comparison of TEM (which visualizing only silver nanowires) and AFM (which visualize nanowires with shell) data shows that the upper limit of the PVP coating thickness could not exceed 5 nm (not shown).

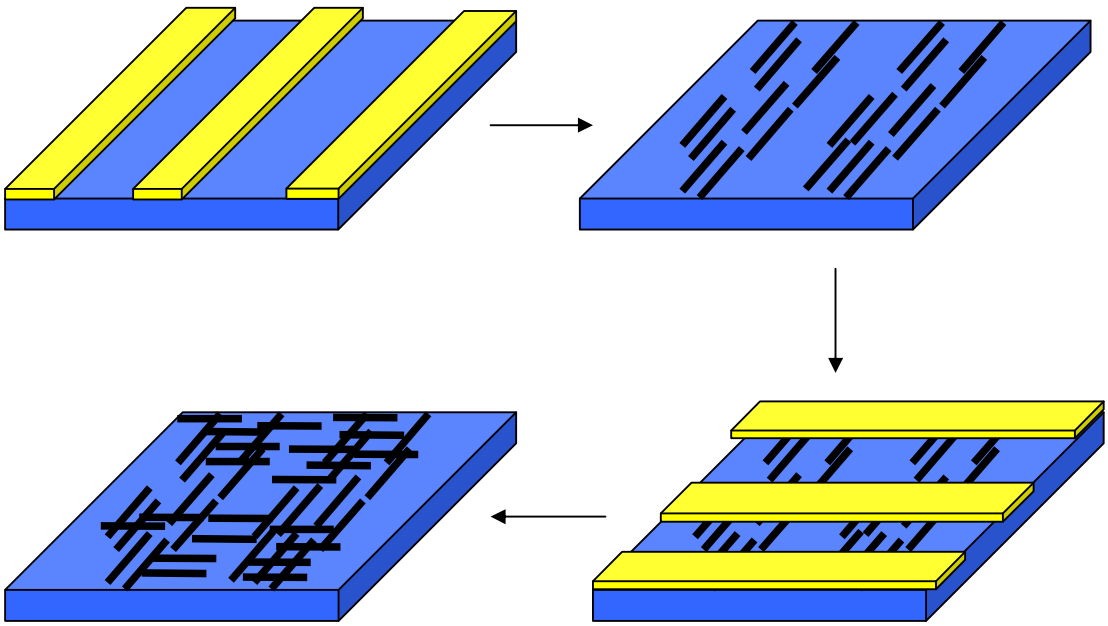

Figure 6.1. Fabrication of crossbar array of silver nanowires using sacrificial polymer micropatterns as guided templates in double-step transversal capillary transfer microprinting and orientation process.

We used sacrificial double-step microprinting approach with polymer micropatterns as guided templates for the deposition of silver nanowires to prepare crossbar arrays of silver nanowires on a silicon substrate (Figure 6.1). To yield a highly oriented array silver nanowire solution (1-3 mg/mL in methanol) was drop-casted onto the array of narrow channels composed of a sacrificial polystyrene (PS) micropattern (ridges with 3 μm periodicity and 1 μm height) resulting in parallel arrays of silver nanowires. The 1 μm thick sacrificial PS micropattern was deposited on the silicon substrate by a polydimethylsiloxane (PDMS) stamp. After deposition of silver nanowires, the PS pattern was lifted off by toluene leaving patterned stripe arrays of highly oriented silver nanowires (Figure 2a). We repeated the process of PS micropatterns perpendicular to the first layer of silver nanowire arrays to prepare crossed arrays of silver nanowires.[169]

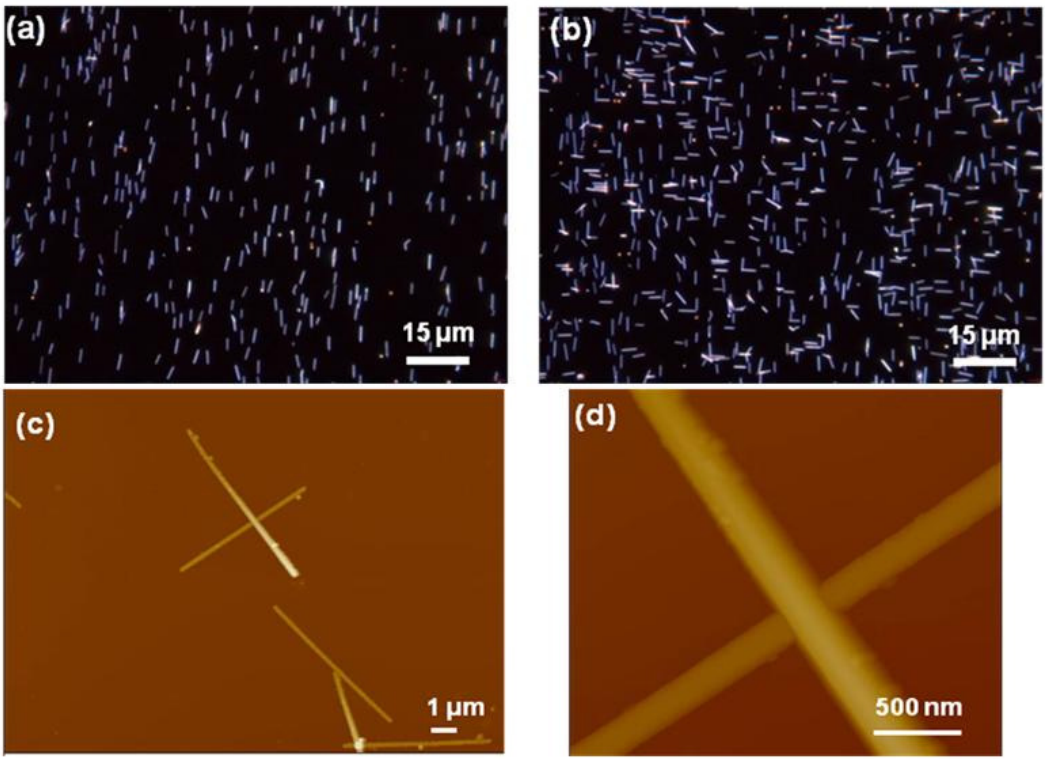

Figure 6.2. (a) Dark-field optical micrographs of uniformly oriented silver nanowires; (b) an array of orthogonal nanowires; (c,d) AFM images of individual silver nanowires and crossbars.

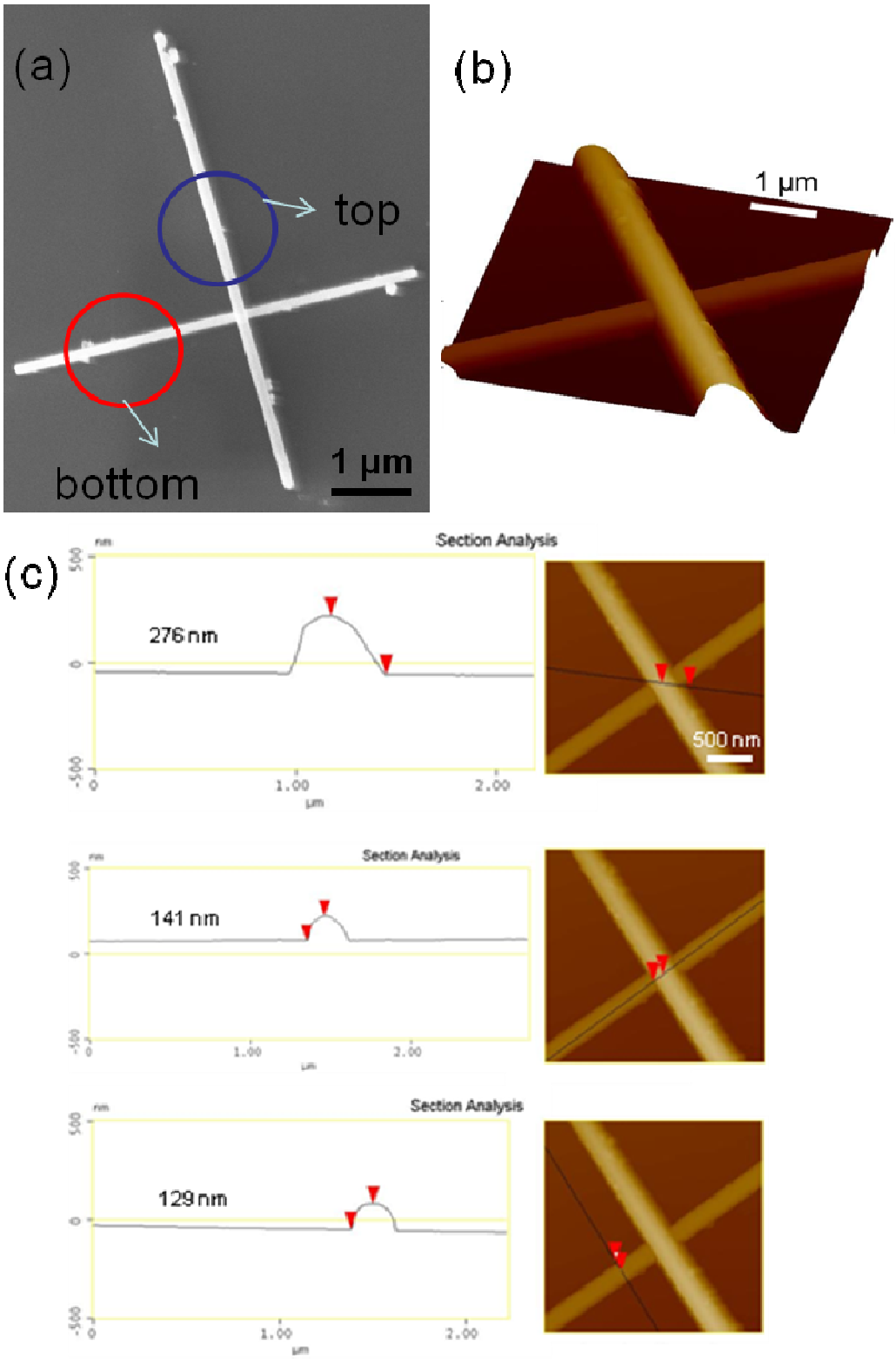

Figure 6.3. (a) SEM of a single silver nanowire crossbar with attached nanoparticles, (b) 3D AFM images of central junction of silver nanowire crossbar which allows to distinguish top and bottom nanowires with corresponding cross-sections (c).

By repeating this template-orientation procedure in an orthogonal direction, a massive silver nanowire array with orthogonally oriented silver nanowire pairs of L and T shapes as well as crossbars can be formed (Figure 6. 2b). Overall, more than 40% of all silver nanowires participate in the formations of junctions between perpendicular nanowires of different types.

Individual crossbars are composed of two perpendicular silver nanowires with one nanowire crossing another as visible from SEM and AFM images (Figures 6. 2, 3). Cross-sectional analysis of crossbars in the junction point shows that top and bottom nanowires are not significantly deformed after the formation of crossbars and stay within ±5% (Figure 3c). Therefore, PVP coating is not significantly deformed by slightly bend the top nanowire and allow access of external analytes to the central junction. Occasional silver nanoparticles attached to the silver nanowires can be also observed on corresponding SEM and AFM images (Figures 6. 2, 3).

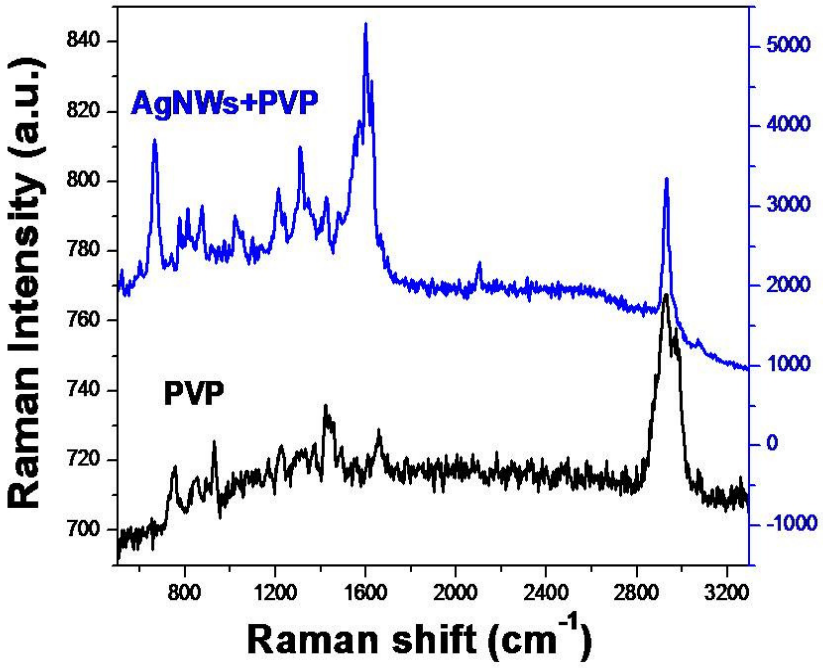

Figure 6.4. Raman spectra of bulk PVP material and silver nanowires coated with PVP.

6.3.2. SERS phenomena on silver nanowire crossbar

Raman spectra of bulk PVP, which is a coating material for silver nanowires, showed characteristics bands in 740 – 1650 cm^{-1} range corresponding to ring breathing vibrations and strong peak at 2925cm^{-1} which corresponds to CH_2 asymmetric stretching (Figure 6.4).[168] Raman spectra of PVP coated-silver nanowires show a strong peak at 232 cm^{-1} due to Ag-O stretching vibration. A strong peak at 1599 cm^{-1} showed up as a result of SERS (Figure 6.4).[170] This characteristic band with high intensity was utilized in this study for Raman micromapping.

6.3.3. SERS phenomena of silver nanowire crossbar with silver nanoparticles dependence on polarlization direction

Figure 6.5(a) displays an example of such measurements which include optical images of a selected nanowire crossbar. Optical images of the silver nanowire crossbars show the presence of nanoparticles located along the nanowires as well as in the vicinity of the crossbar. The corresponding SERS micromapping for this selected silver nanowire crossbar at different orientations of this crossbar in respect to the polarization direction (always horizontal) in shown in Figure 6.5(b). Raman scattering collected with high resolution (50 nm per pixel, λ = 514 nm) at this polarization shows the strongest central spot (1) which corresponds to the crossbar nanojunction (Figure 6. 5). This location represents the most intense “hot spot” caused by a coupled transversal plasmon resonances of bottom and top nanowires.

A characteristic pattern of other bright spots corresponds to the locations of silver nanoparticles along the vertical nanowires (three spots in the middle section (points 2,3, and 4)) (Figure 6.6). Low intensity spots are also associated with left and right (point 5) tips of the horizontal nanowire (Figure 6.6).

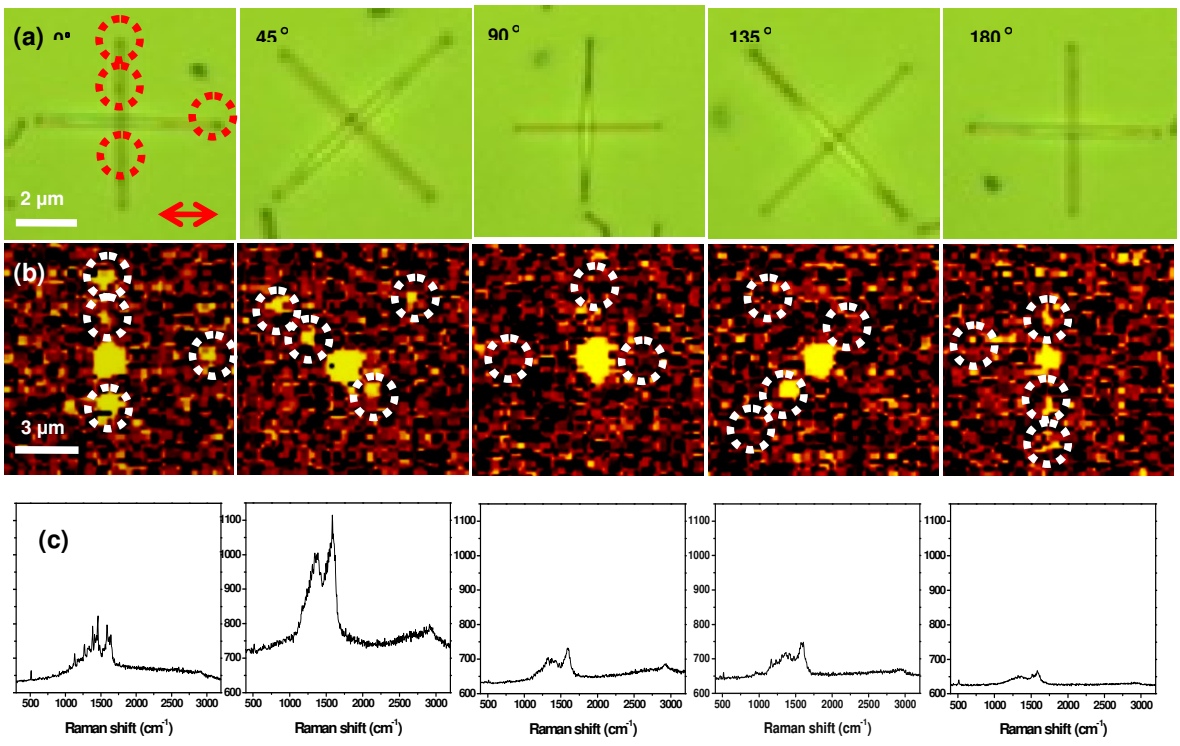

Figure 6.5. (a) Optical micrographs and (b) Raman micromapping of crossbars with different orientation (dashed circles indicating attached silver nanoparticles on silver nanowires and corresponding hot spots, polarization is horizontal for all images), (c) corresponding Raman spectra of central junction from images (b).

Rotation of the polarization plane in respect to the crossbar changes their scattering intensities dramatically (Figure 6b). Raman scattering shows the central brightest "hot spot" which corresponds to the junction of the nanowires at different polarization orientations with significant increase at 45^{o} polarization orientation (Figure 6b). The intensity of this hot spot changes somewhat at different polarization orientations due to background scattering and

fluorescence with overall intensity gradually decreasing due to continuous photo-initiated pyrolysis during long-time collection of images (from left to right in Figure 6c).[171,172,173] It is worth to note again that all images presented here are collected from a central junction (single pixel size of 50 nm) thus reflecting highly localized point excitation and not integrated Raman scattering averaged over large surface area.

In contrast to overall intensity, the shape of the double band within 1400-1600 cm^{-1} does not change much at different polarization orientations.[174] On the other hand, a characteristic cross-shaped pattern of localized hot spots at 0^{o} can be recognized at 45^{o} and partially at 135^{o} as well as 180^{o} although with lower intensities (Figure 6.5). However, the cross-shaped pattern disappears for the 90^{o} polarization orientation.

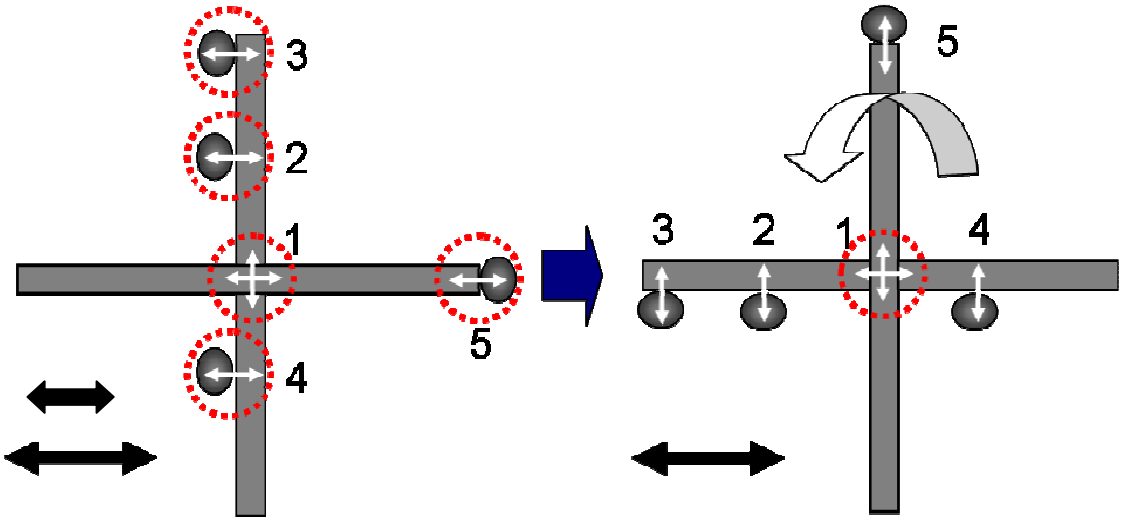

Figure 6.6. Schematic of the different directions of plasmon resonances of silver nanowires with attached nanoparticles at different orientations, polarization is horizontal.

The polarization-dependent appearance and disappearance of the different hot spots can be understood considering recent results on SERS behavior of one-dimensional structures. Indeed, it has been demonstrated that decorating silver nanowires with nanoparticles results

in highly localized plasmon resonances along the nanowires.[175] It has been also observed that the excitation of transversal plasmon resonances in decorated silver nanowires for polarization perpendicular to the long axis causes significant polarization-dependent SERS effect.[158]

In the case of the crossbars locally decorated with silver nanoparticles we can distinguish two very different polarization-dependent phenomena. Polarization-independent characteristics of the central hot spot with the highest intensity can be caused by complementary contributions of coupled orthogonal transversal plasmon resonances at different polarization orientations (Figure 6.6). If the hot spot is formed at nanoparticle-nanowire gap, strong polarization dependence should be observed with strongest Raman intensity observed if the direction of polarization is perpendicular to the nanowires long axis.[158] These differences should cause a peculiar polarization-dependent behavior of crossbars which is very different from the behavior of single nanowires and their bundles. Namely, this unique feature is an unchanged central hot spot at crossbar junction combined with strong polarization-dependent auxiliary hot spots along nanowires as illustrated in Figure 6.6. The pattern observed in experiment discussed here can be explained by lateral attachment of associated silver nanoparticles (points 2, 3, 4) to vertical nanowires and nanoparticle (point 5) attached to the nanowires tip (Figure 6.6). In this schematic, white arrows show different directions of localized transversal plasmon resonances between nanowires and nanoparticles as well as at junction at two different crossbar orientations which correspond to two situations with 0^{o} and 90^{o} polarizations as presented in Figure 6.6.

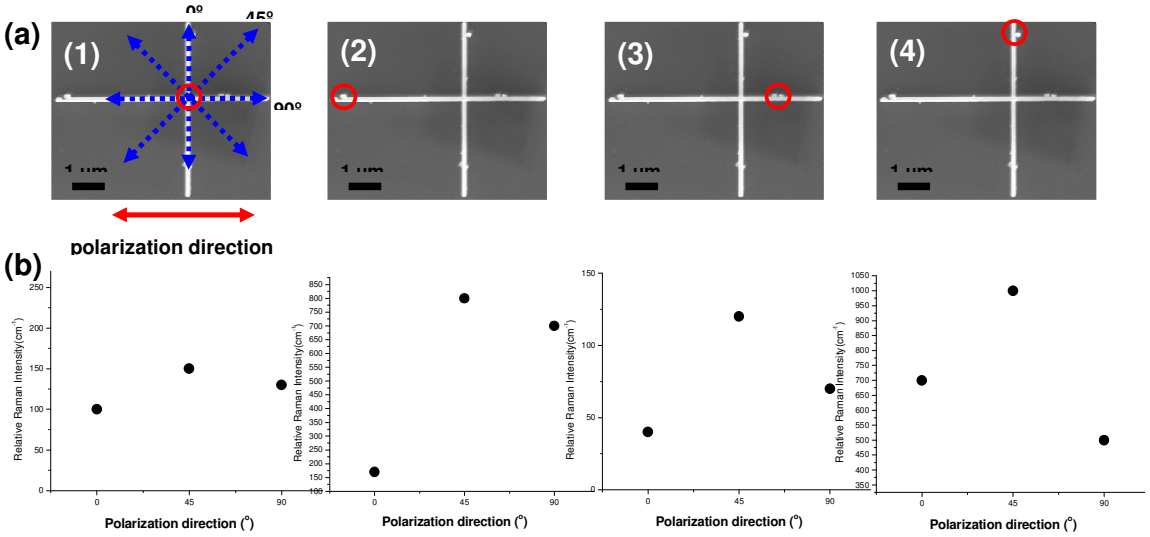

Figure 6.7. (a) Hot spots (circles) of silver nanowire crossbar with attached nanoparticles with different orientations (polarization is horizontal), circles indicate hot spots at different crossbar orientation and numbers correspond to selected points in (a); (b) relative Raman intensity of 1599 cm^{-1} at each hot spot (points 1-4 from (a)) of silver nanowire crossbars at different polarization directions.

We further demonstrate the polarization-dependent SERS results for other shape of crossbars of which horizontal nanowire is located on top of vertical nanowire in Figure 6.7. SEM images of the crossbars confirm the location of nanoparticles, which is exactly corresponding to the SERS hot spots as indicated in Figure 6.8 and illustrated in Raman micromapping in Figure 6.9. Each Raman spectra from the silver nanowire crossbar was demonstrated in Figure 9 and the red circles correspond to the different hot spots. Overall, these results reveal polarization-independent characteristics of the central hot spot caused by coupled transversal plasmon resonances of the bottom and top nanowires

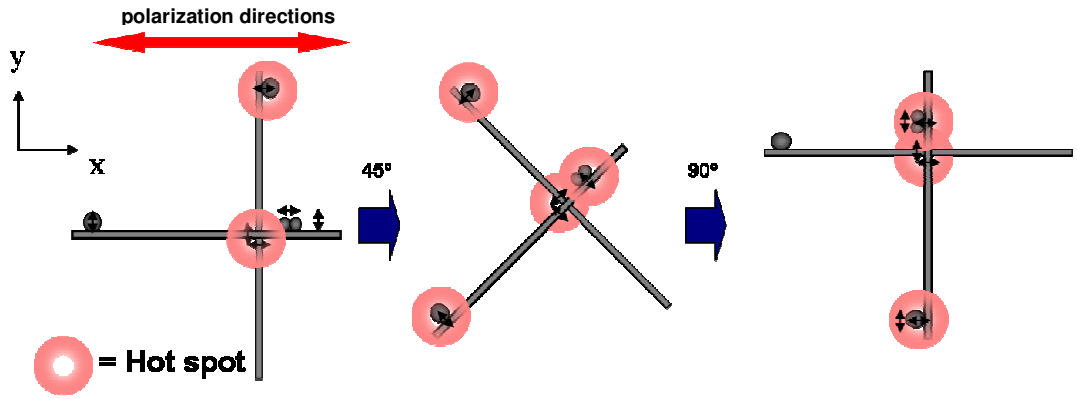

Figure 6.8. Schematic of hot spots (circles) of silver nanowire crossbar attached with nanoparticles at different crossbar orientations.

At different polarization directions, the relative Raman intensities at central junction of nanowire crossbar is maintained as the same intensity as shown in Figure 7a (point 1). On the other hand, the SERS at the junction of nanowire and spherical nanoparticles shows the polarization-dependent characteristics. At the hot spots marked as red circles in the SEM images Figure 6.7a (points 2,3), the relative Raman intensities from PVP coating at the junction between nanowire and nanoparticle are observed to be enhanced as the polarization direction is changed due to the coupling with the silver nanoparticles Figure 6.7(b). The stronger Raman intensities are also observed when the direction of polarization is perpendicular to the nanowires long axis. Lower Raman enhancement is observed in the case of the junction between attached nanoparticles and nanowire (Figure 6.7a (point 4)) and if the laser polarization direction is perpendicular to the nanoparticle-nanowire gap (Figure 6.7(b)). Schematic of hot spots (red circles) of silver nanowire crossbar with attached nanoparticles and nanoparticle dimmers also correlates with variable SERS intensities at different polarization directions (Figure 6. 8).

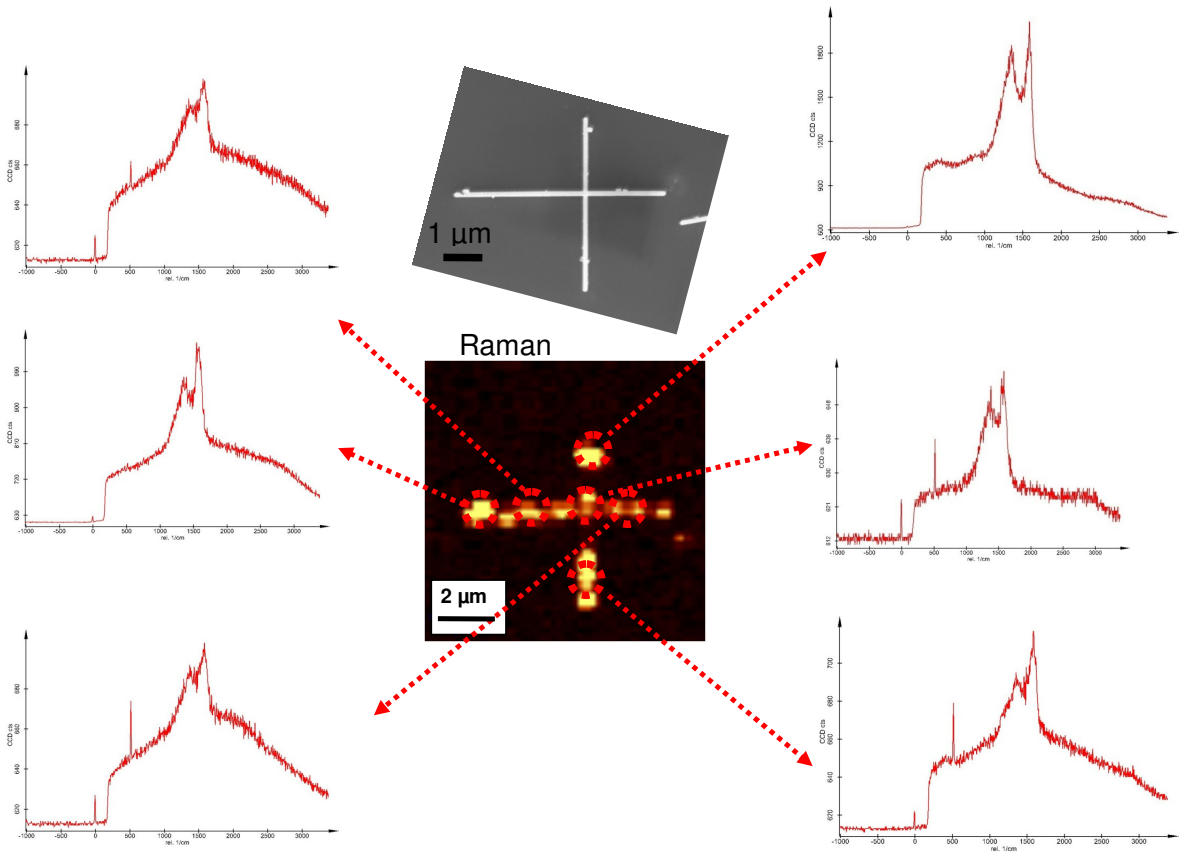

Figure 6.9. Raman spectra of crossbar of silver nanowires, red circles correspond to the different hot spots with corresponding Raman spectra shown in separate plots.

We exposed our silver nanowire crossbar with silver nanoparticles to well-known Raman analyte, Rhodamine 6G (R6G) to study SERS polarization dependence with higher angular resolution than that demonstrated for Raman mapping above. For these measurements, the silver nanowire crossbars with silver nanoparticles deposited on Si substrate were immersed in an aqueous solution of 10^{-5} M R6G, rinsed thoroughly with Nanopure water, and dried. SERS spectra from the silver nanowire crossbar junction and the silver nanowire-nanoparticle junction were collected with 1 second exposure time with 3 rounds of accumulations to assure high signal to noise ratio (Figure 10). Characteristic Raman bands of R6G (1360, 1504, and 1644 cm^{-1}) from aromatic benzene rings were strongly enhanced at the nanowire

crossbar junction and visible at SERS spectrum (Figure 10a). SEM image clearly shows the silver nanowire crossbar junction and the silver nanowire-nanoparticle junction which corresponds exactly to the spectra collected and analyzed (Figure 10, 11).

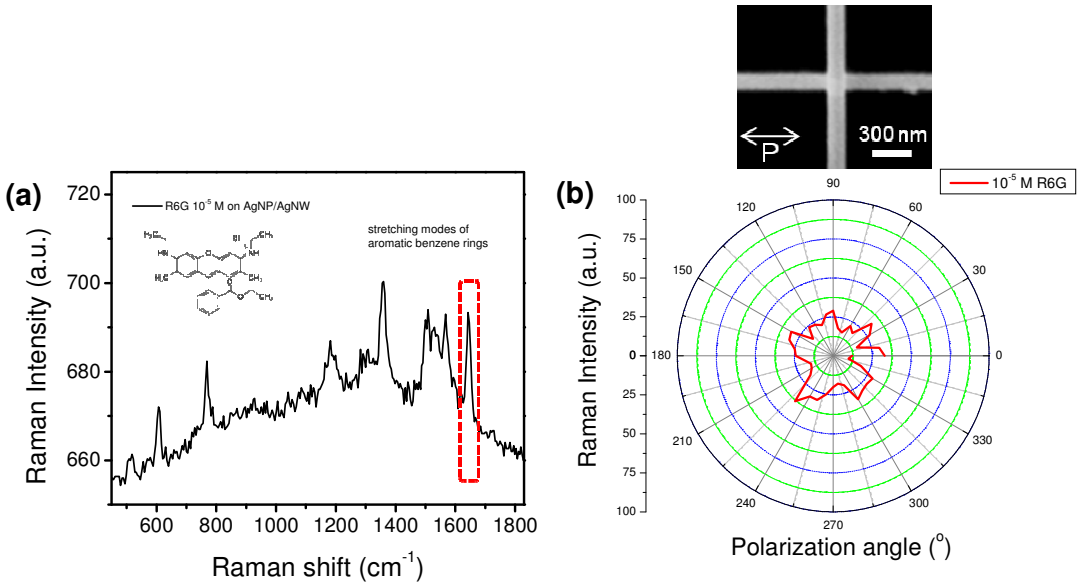

Figure 6.10. (a) Raman spectra of 10^{-5} M of R6G on silver nanowire crossbar junction, (b) the relative Raman intensity of 1644 cm^{-1} from the silver nanowire crossbar junction at different polarization directions; inset shows specific crossbar tested here at particular orientation (0^{o}).

The relative intensity of specific Raman band at 1644 cm^{-1} was monitored and plotted at each 10^{o} of polarization orientation as presented in polar diagrams in Figures 10b and 11b. As was observed, the relative Raman intensities of selected band at the central junction of nanowire crossbar maintained near constant intensity at different polarization directions within ± 30 % (Figure 10b). This modest and random variation confirms the fact that two crossing nanowires create coupling conditions that are polarization independent as was reported above from Raman mapping with lower angular resolution.

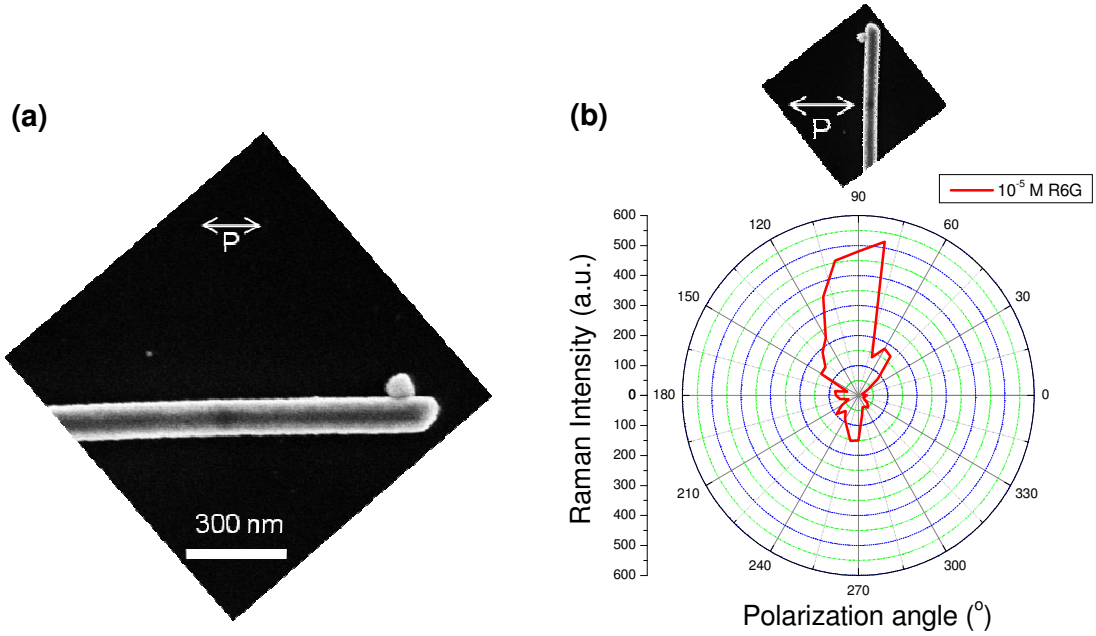

Figure 6.11. (a) High resolution SEM image of junction between silver nanoparticle and nanowire, (b) the relative Raman intensity of 1644 cm^{-1} from the silver nanowire-nanoparticle junctions at different polarization directions, insets show specific nanowire-nanoparticle end tested here at two particular orientations (90° and 0°).

However, for a single nanoparticle attached to the nanowire, a strong polarization dependency has been observed (Figure 11). As the polarization direction changes to parallel to the junction between silver nanoparticle and silver nanowire, the Raman intensity increases up to 15 times due to the coupling of nanostructures (Figure 11b).[165] As the polarization direction becomes close to the perpendicular to the junction of the nanoparticle and nanowire (see inset in Figure 11b), the relative Raman signal intensity decreases dramatically to close to background level. It is worth to note that the gradual decrease of the overall relative Raman intensity with measuring time reflects the gradual deterioration of organic molecules during the continuous exposure to laser illumination, a common phenomenon observed for similar nanostructures.[158] However, overall it is apparent that high angular resolution studies of polarization dependency confirm conclusion made above on dramatically different

polarization behaviors of central crossbar junction and specific hot spots formed by nanoparticle-nanowire junctions.

6.3. Conclusions

In conclusion, in this study we demonstrated that depending upon exact location and orientation of decorating nanoparticles, a variety of different rotational patterns with different on/off SERS intensities can be designed. While the relative Raman intensities from central junction of nanowire crossbar are maintained at different polarization directions, the SERS at the junction of nanowire and spherical nanoparticles shows the polarization-dependent characteristics. The stronger Raman enhancement is observed when the polarization direction is parallel to the gap between nanowire and nanoparticles, which is due to the coupling with nanoparticle. Overall, this approach provide means for the fabrication of arrays of hot spots which can be activated only at a certain polarization direction and suppressed at an orthogonal direction while keeping some hot spots activated under any condition.

Such an array with on-demand activation could be of interest for multifunctional assays for chemical and biological detections. Although the exact placement of nanoparticles is challenging we suggest that proper design of crossbars decorated with nanoparticles might be completed by selective micropatterning as will be a subject of future studies.

Chapter 7. Responsive hybrid nanotubes composed of block copolymer and gold nanoparticles

7.1 Introduction

One dimensional (1D) organic nanostructures such as rods, tubes, wires, and belts have been of intense interest due to their unique physical properties originating due to the confinement on characteristic length scale of the components (e.g. radius of gyration, single domain).[176,177,178,179] Fabrication of 1D organic nanotubes or nanorods structures has been achieved by a variety of methods such as template assisted,[180] self assembly in the liquid phase,[181] and electrospinning.[182] Among these fabrication methods utilizing templates has been widely investigated due to favorable traits such as easy control over the shape, size, and the diversity of materials that can be used.[57,183,184] Among various nanostructures polymer nanotubes and nanorods can be assembled by wetting, vacuum, and spin based infiltration of polymer melt or solution into nanocavity.[185] Recently, it has been reported that diblock copolymer nanorods are fabricated by infiltration of polymer melt into anodic alumina membrane template with high temperature (230°C) and investigated the topology of nanorods at different pH.[68] The responsive nanorods exhibited a change in the topology to mesoporous state upon exposure to acidic environment.

However, compared to the polymer nanorod structure, nanotube structure provides not only large surface-to-volume, but also the through channels along the long axis, applicable for microfluidic systems.[186] It has been demonstrated that the infiltration and subsequent solidification of a polymer into the porous template results in either hollow nanotubes or solid nanorods depending on the wetting behavior of the polymer with the walls of the template.[187]

The reversibility of topology, size and the optical signature of the composite nanotubes with external pH remain to be investigated.

7.2. Experimental detail

Block copolymer PS(102k)-b-PVP(97k) was purchased from Polymer Source Inc. Porous alumina membranes (PAMs) were purchased from Whatman (Anodisc 47) and the average pore size was 243 ± 5 nm with 60 μm total thickness. Nanotubes were formed by infiltration of 2 wt% PS-b-PVP in THF into PAMs three times using spin coating. Then nanotubes are exposed to tetrahydrofuran (THF) vapor for 24 hours. Nanotubes in PAMs were immersed in 0.75 wt % of tetrachloroauric acid (Aldrich) for 24 hours. Gold nanoparticles were selectively reduced in P2VP domain in aqueous reducing agent 0.15 wt % (sodium citrate) solution. Then nanotubes were released from PAM templates by dissolving in 40 wt % of KOH solution. Nanotubes were separated by sonication for 15 minutes and centrifuged (5000 rpm) then redispered in Nanopure water 5 times to remove residual KOH salt.

7.3. Results and Discussion

7.3.1. Fabrication of responsive hybrid nanotubes

We demonstrated the facile fabrication of hybrid 1D nanostructures comprised of pH responsive block copolymer, polystyrene-block-poly (2-vinylpyridine) (PS-b-P2VP) with encapsulated gold nanoparticles. We successfully fabricate microphase separated PS-b-P2VP nanotubes with larger surface-to-volume by solvent annealing under physical confinement (Figure 7.1).[186] In situ reduction of gold nanoparticles in P2VP domain was

used to decorate the inner wall and outer shell of the nanotubes. Such an approach results in uniform distribution of nanoparticles comparing to the conventional approach of mixing gold nanoparticles and block-copolymer. Furthermore, we demonstrate that the pH responsive nature of P2VP is translated to a reversible change in topology and optical properties of the block copolymer nanotubes.

As known, P2VP is a weak cationic polyelectrolyte exhibiting a coil to globule transition above pH 3.6.[60] PS (M_w = 102,000)-P2VP (M_w = 97,000) diblock copolymer (Poly Source^{TM}) utilized in this study can be dissolved in common solvent, tetrahydrofuran (THF), and form lamellar phase. Under the physical confinement in the nanopores of the anodic alumina membranes, PS-b-P2VP forms tubular structure along the channel with the lamellae parallel to the walls of porous alumina as is demonstrated by Russell et al.[188] Nanotubes with aspect ratio up to 20 (about 250 nm of diameter and ~5 μm of length) can be fabricated by spin assisted infiltration of PS-b-P2VP from THF solution followed by solvent annealing and complete dissolution of the alumina membrane.[183,189] It has been demonstrated that the infiltration and subsequent solidification of a polymer into the porous template results in either hollow nanotubes or solid nanorods depending on the wetting behavior of the polymer with the walls of the template.[187]

In fact, SEM images show PS-b-P2VP nanotubes fabricated in this study with diameter of 250 nm corresponding well to the pore diameter of the membrane (Figure 7.2a,b). The microphase separation of the PS and P2VP domains is clearly revealed by the cross sectional SEM images (Figure 7.2c).

For a polymer which readily spreads, the templating results in long nanotubes whereas in the case of limited spreading it results in short nanorods. PS-b-P2VP in THF exhibits high wettability to PAMs, thus resulting in block copolymer nanotubes. Comparing to the nanorod structures frequently demonstrated for these block-copolymers, nanotubes possess not only larger surface-to-volume ratio, but also the through channels along the long axis, applicable for microfluidic system.[186]

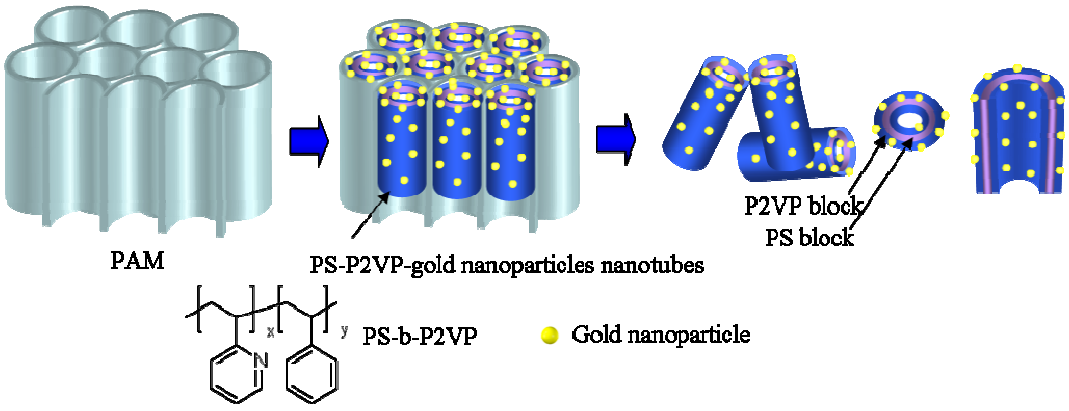

Figure 7.1. Fabrication process of PS-b-P2VP-gold nanoparticles nanotubes.

However, the confinement of the lamellar structures with discrete dimension of 30 nm per domain parallel to the walls of the pores results in small through pores. It is known that during the initial deposition, due to the fast solvent evaporation, the block copolymer freezes into fingerprint patterns when spin coated on flat substrate which can be annealed to achieve ordered microphase separation.[189,190,191,192] We employed solvent annealing in which, PS-b-P2VP nanotubes were exposed to THF vapor for 24 hours to enable ordered microphase separation.[189] Following the solvent annealing, the structure evolves in which, the P2VP domains with higher affinity to hydrophilic alumina wall occupy the inner wall and outer shell (30 nm each) with the PS domain (60 nm) located in between the P2VP domains (Figure 7.4a).

7.3.2. Responsive hybrid nanotubes

Gold nanoparticles were formed by selective reduction inside in P2VP domains of block-copolymer nanotubes by exposing them to the gold salt solution (tetrachloroauric acid) for 15 hours. $HAuCl_4^-$ ions bind to the protonated pyridine units of the P2VP resulting in pyridinium salt.[193,194] Subsequently nanotubes are washed in Nanopure water and are immersed into aqueous solution of reducing agent (sodium citrate) resulting in the formation of the gold nanoparticles in P2VP domains (Figures 7.2, 3).[195] Gold nanoparticles were found to grow uniformly on the inner wall and outer shell of nanotubes (Figure 7.2c). The presence of gold nanoparticles in the P2VP domains further supports the suggested structure, in which the P2VP domains form the inner wall and outer shell of the nanotubes with PS domain separating them. The EDS confirms the presence of gold nanoparticles in the nanotubes (Figure 13d).

High resolution TEM image shows that the gold nanoparticles (about 15 ± 2 nm in diameter) are uniformly distributed along the entire length of the nanotubes (Figure 7.3a,b).

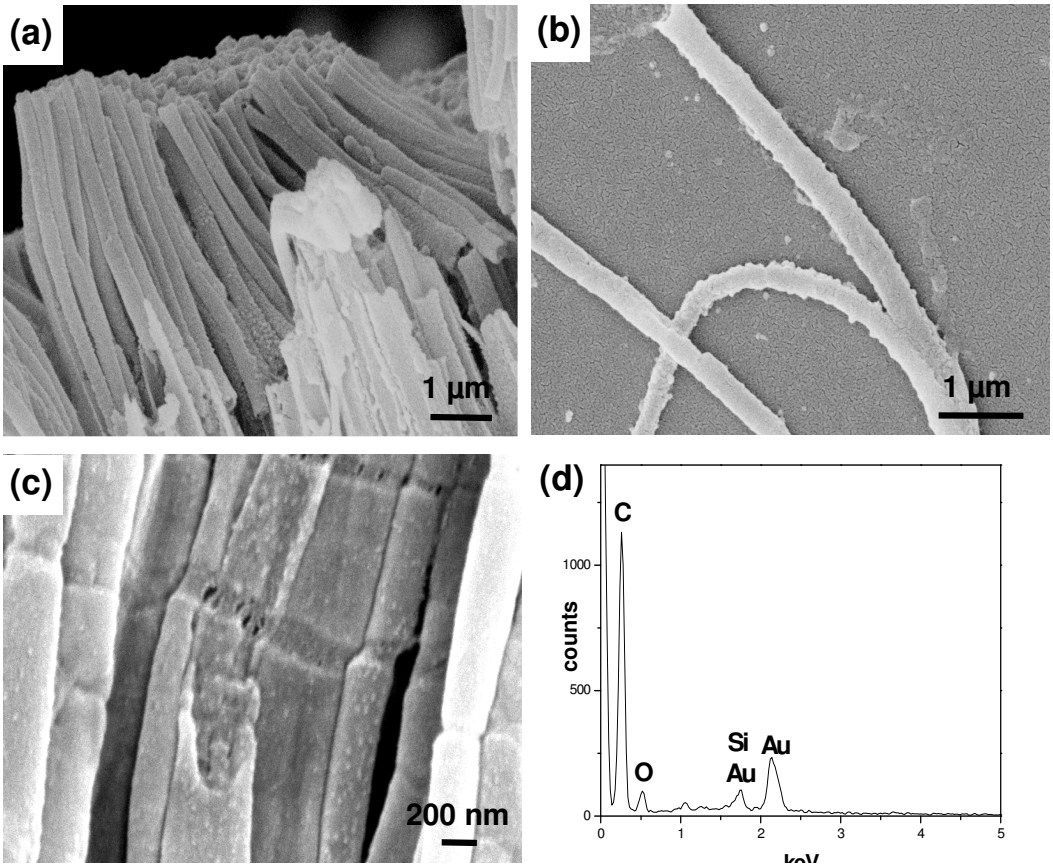

Figure 7.2. (a), (b) SEM images of PS-b-P2VP/gold nanoparticles hybrid nanotubes, (c) inner structure of nanotubes (d) EDS spectrum indicating the presence of Au in polymer nanotubes.

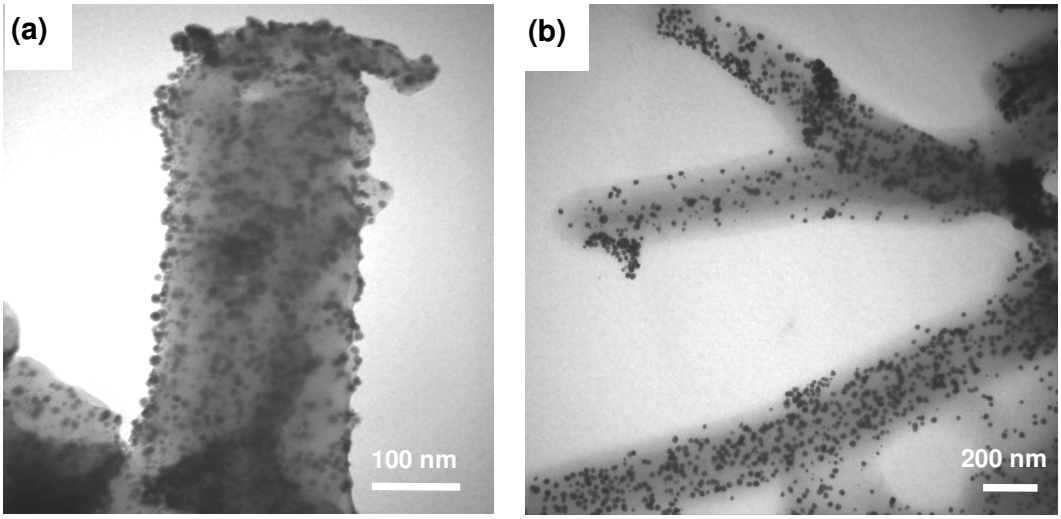

Figure 7.3. (a), (b) TEM images of PS-b-P2VP/gold nanoparticles hybrid nanotubes.

7.3.3. pH response of hybrid nanotubes

Due to their pH sensitive nature, P2VP domains swell upon exposure to pH below 3.6 due to protonation of nitrogen in pyridine group which causes electrostatic repulsion leading to swelling of the polymer chains.[68,196] This transformation leads to the dramatic change in the topology of nanotubes in response to the external pH (Figure 7.4a, b, c). We employed pH 2 (coil state) and pH7 (globule state) to study the morphology changes and optical response of PS-b-P2VP-gold nanoparticle nanotubes. In neutral state, one can observe the smooth surface of PS-b-P2VP nanotubes uniformly decorated with gold nanoparticles (Figure 7.4a). When PS-P2VP-gold nanotubes are exposed to pH2, inner wall and outer shells of the P2VP domains swell forming grainy structure (Figure 7.4b). Inset of Figure 7.4b shows the expanded nanotubes structure due to the swelling of P2VP domains. It has been demonstrated that P2VP exhibits a 100% volumetric swelling upon exposure to pH2.[196] Apparently, the mechanical integrity of nanotubes is preserved by the glassy PS block. Upon exposure of the PS-b-P2VP porous nanotubes to the neutral condition (pH 7 solution), the highly grainy morphology of nanotubes is apparently recovered to the initial smooth surface (Figure 7.4c).

Apart from the morphology rearrangement, the diameter of PS-b-P2VP nanotubes is altered upon exposure to pH2 (Figure 7.4a,b,c). The diameter of PS-b-P2VP nanotubes is 240 ± 5 nm after neutral solution but increases up to 300 ± 10 nm after swelling at pH 2. Assuming that the entire increase in the diameter (60 nm) results from the swelling of P2VP domains (120 nm), the linear swelling of the P2VP domains is estimated to be 50%. After exposure to neutral solution (pH 7), P2VP blocks are deprotonated and the nanotubes shrink back to the initial size.

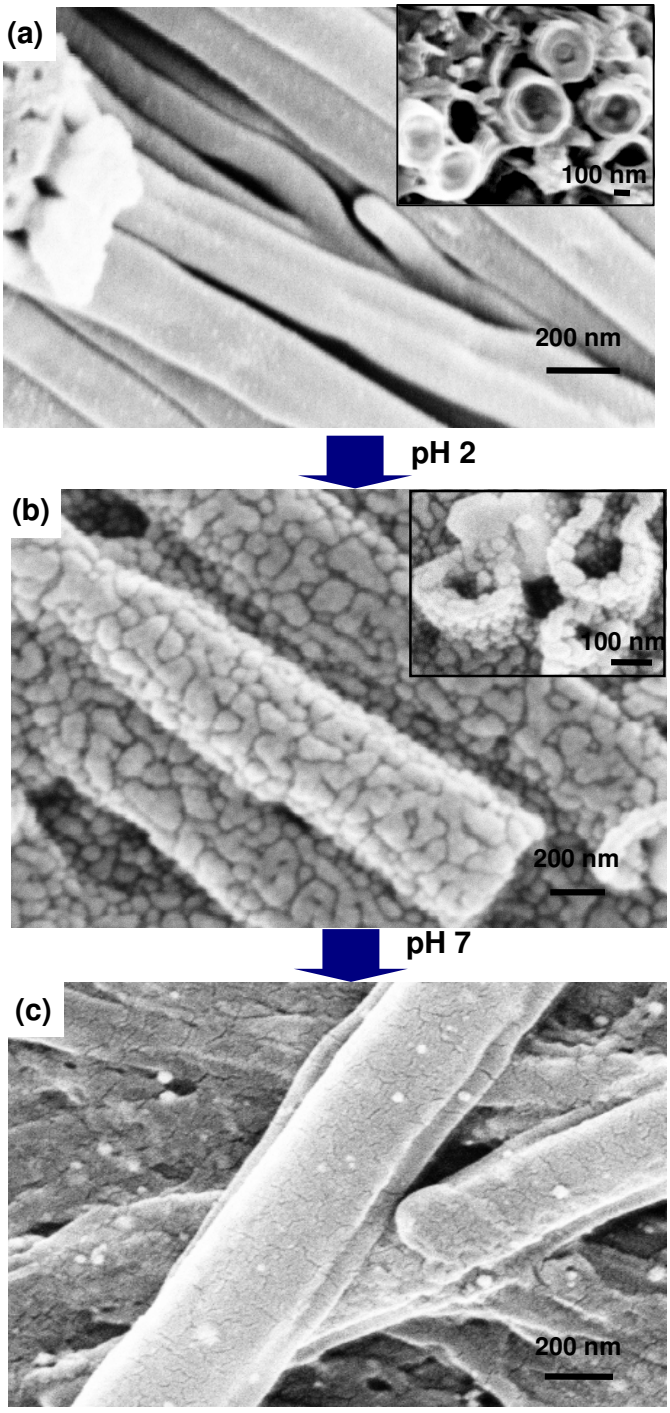

Figure 7.4. (a) SEM images of PS-b-P2VP/gold nanoparticles hybrid nanotubes, (b) after exposed to pH 2, and (c) exposed to pH 7.

The encapsulation of gold nanoparticles in PS-b-P2VP nanotubes results in an appearance of a strong absorption band at 540 nm due to the surface plasmon resonance of individual gold

nanoparticles (Figure 7.5a).[197] The morphological changes caused by exposure of PS-b-P2VP nanotubes to pH 2 resulted in a 23 nm red shift of the plasmon resonance of the encapsulated gold nanoparticles (Figure 7.5a). This is in strike contrast to previous studies of P2VP-gold nanoparticles thin films which observed a blue shift upon swelling of the P2VP domains.[62] The blue shift is associated to the increased separation between the gold nanoparticles uniformly dispersed in the planar films.

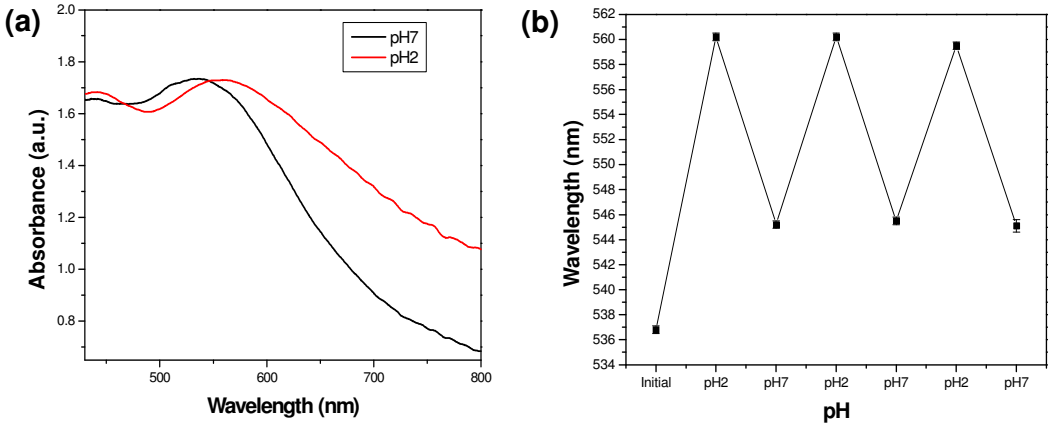

Figure 7.5. (a) UV-vis absorption spectra of PS-b-P2VP/gold nanoparticles hybrid nanotubes exposed topH7, and pH 2 solutions, (b) the reversibility of spectra at pH 7 and pH 2.

We suggest that, in the case of PS-P2VP nanotubes studied here, swelling of the P2VP blocks causes the aggregation of the gold nanoparticles at the outer surface. This aggregation increases coupling of plasmon resonances, resulting in the red shift.[144,145,197] Repeated exposure of nanotubes to neutral solution results in the gold nanoparticles rearrangement due to topology recovery resulting in a 15 nm blue shift of the plasmon peak. The data reported here is collected after exposure for 40 minutes to ensure the complete response. Therefore, subsequent cycling between pH2 and pH7 exposures results in an alternating red-blue shifts

of 15 nm (Figure 7.5). These optical responses are completely reversible for multiple times (Figure 7.5b).

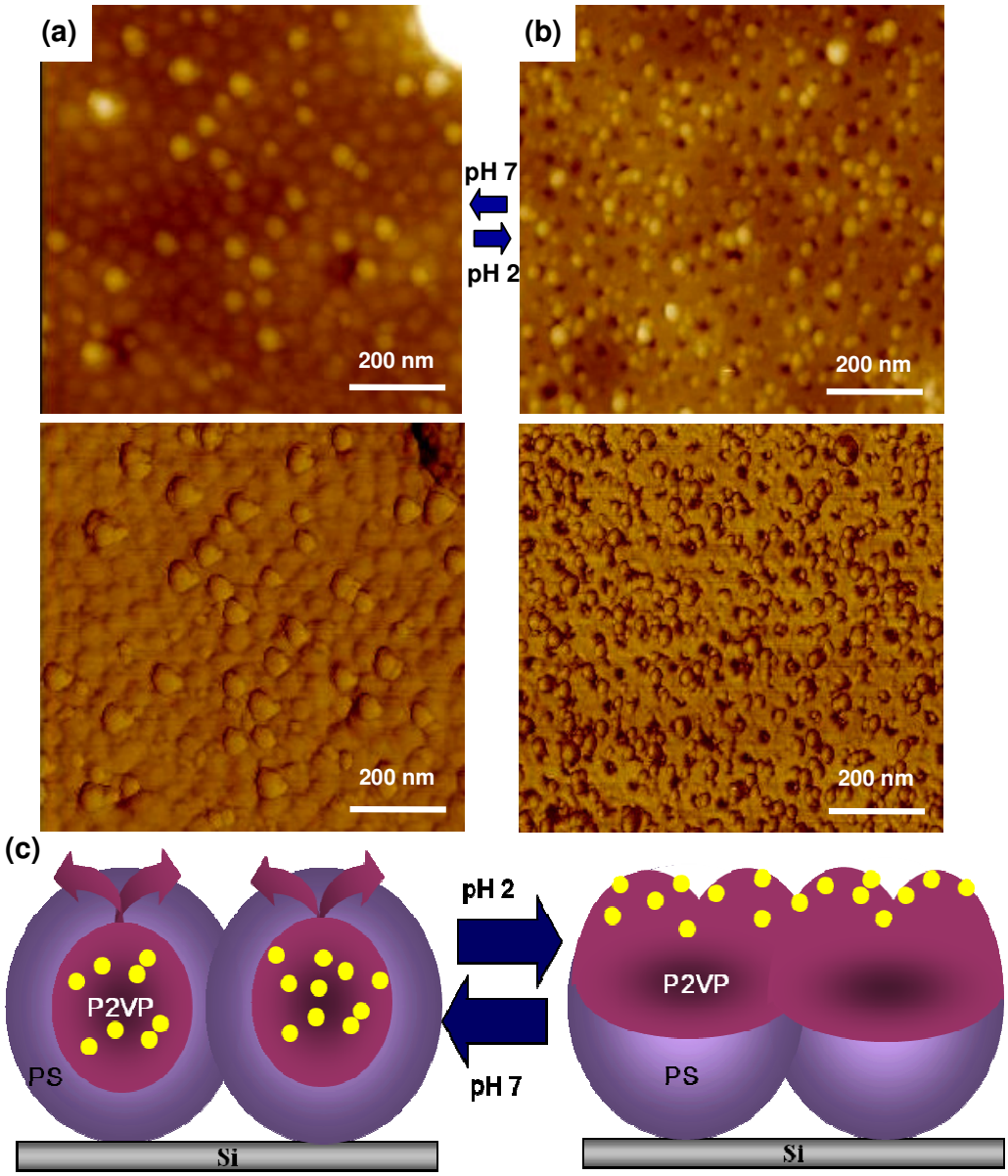

Figure 7.6. (a) AFM topographical (top) and phase (bottom) images of PS-b-P2VP micelle structure spin coated film on Si substrate with gold nanoparticles, (b) after exposed to pH 2. (c) Schematic of morphology changes of PS-b-P2VP-gold nanoparticles micelle structure under pH treatment.

For further understanding of the topology changes and gold nanoparticles rearrangement of PS-b-P2VP nanotubes with external pH, which causes plasmon resonance shift, we employed

PS-b-P2VP micelles. PS-b-P2VP dissolved in toluene, selective solvent for PS, forms micelles with P2VP core and PS shell. The micelle film is prepared by spin coating on a silicon substrate and gold nanoparticles were reduced by the same method described previously.

AFM images show the micelle structure of PS-b-P2VP thin film with gold nanoparticles in the P2VP domains (core of the micelle) (Figure 7.6a). The dimpled structure of PS-b-P2VP micelles after exposure to pH2 solution, and the presence of gold nanoparticles on the surface are clearly visible in Figure 7.6(b). Upon exposure to pH2 solution, P2VP cores with gold nanoparticles swell, resulting in dimpled structure of the micelle film and exposure of the gold nanoparticles to the surface as shown in schematic (Figure 7.6c).

7.4. Conclusions

In conclusion, we demonstrated the facile fabrication of pH responsive nanotubes composed of PS-b-P2VP-gold nanoparticle which exhibit a reversible change in the plasmon resonance position. The ordered phase separation of the block copolymer within the nanotube structure is formed by solvent annealing. In situ formation of gold nanoparticles in the P2VP domains allows decorating the inner and outer shell of the nanotubes. The uniformly assembled gold nanoparticles in PS-b-P2VP nanotube structures are clearly demonstrated by SEM and TEM analysis.

Due to the coil to globule transition above pH 3.6 of P2VP block, the PS-b-P2VP-gold nanoparticles nanotubes show reversible changes in topology, size (up to 25%), and collective plasmon resonance appearance. The morphological changes caused by exposure

of PS-b-P2VP nanotubes to pH 2 resulted in a 23 nm red shift of the plasmon resonance of the encapsulated gold nanoparticles because swelling of the P2VP blocks causes the aggregation of the gold nanoparticles at the outer surface increasing the coupling of plasmon resonances, resulting in the red shift. The exposure of nanotubes to neutral solution resulted in the gold nanoparticles rearrangement due to topology recovery resulting in a 15 nm blue shift of the plasmon peak. We suggest that the large surface-to-volume ratio of nanotubes and open through central pore maximizes their interaction with environment, thus enhancing their response to external stimuli which can be extremely beneficial in microfluidics and biosensing.

Chapter 8. General Summary and Directions

8.1. General Discussion

In this study, various novel organic/inorganic nanostructures were synthesized and assembled utilizing template-assisted techniques for the specific sensing applications. One of the important applications of the organic/inorganic hybrid nanostructures is plasmonic-based chemical sensors integrated with porous strcutrues. Due to the unique optical properties of noble metal nanostructures, gold nanoparticles, gold nanorods, silver nanoparticles, and silver nanowires, were all tested in our study. We demonstrated the design of 3D SERS-active substrates, on/off SERS property of nanowire crossbars, and LSPR-based nanotube structure combined with responsive polymer.

This research has suggested a novel nanostructure assembly strategy for the 3D SERS nanostructure arrays which can be one of the breakthroughs to overcome the limitations of traditional planar SERS substrate design. The typical SERS-active substrates designed from 1D, 2D metal nanostructures demonstrated SERS enhancement factors (EF) which are the critical values to estimate the performance of SERS substrates, as about 10^4-10^6 for Raman markers such as Rhodamine 6G (R6G) molecules (Figure 8.1). The trace level detection of liquid explosives and hazardous chemicals which have no specific chemical functionalities as SERS signature is still a challenge using the SERS substrates with these EFs. While the theoretical enhancement factor of 10^8-10^{10} has been also suggested using metal nanosphere arrays, these processes are not easy to reproduce as SERS-active substrates over large areas for practical sensing applications.[8,198,199,200]

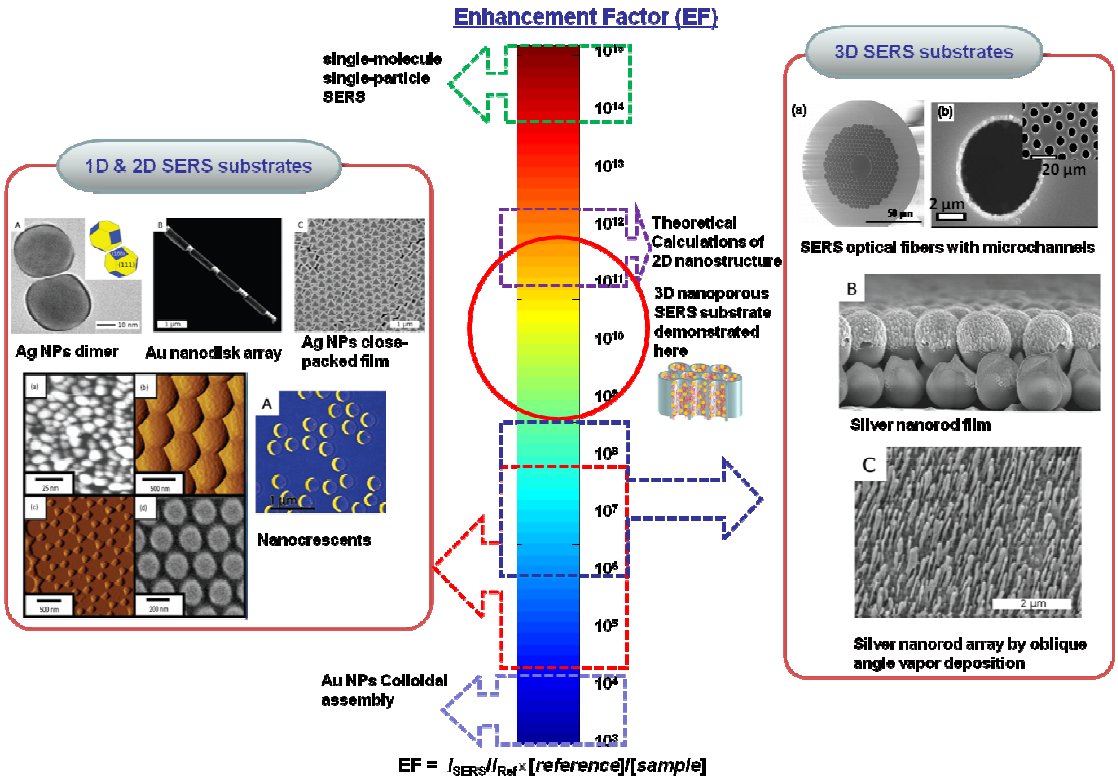

Figure 8.1. Various SERS-active substrate designs with corresponding Raman Enhancement Factor (EF) and the level explored in this study.

Most importantly, in this study, we achieved an unprecedented high Raman enhancement factor of 10^{10}-10^{12} with our novel 3D SERS-active substrate to exceed the current EF by factor of 10^{3}-10^{4}, which allows to detect a trace level of explosives compared to other recently reported 3D SERS substrate designs as shown in Figure 8.1 (10^{6} - 10^{8}).[130] These results are attributed to the large surface area, efficient light interaction, polymeric selective coatings, and a high density of hot spots of our novel 3D nanostructure arrays. Moreover, the developed nanostructure assembly techniques in this study are low-cost, uniform, large-scale process compared to any current 3D SERS-active substrate designs created by using expensive lithographic fabrication technique such as E-beam or vapor deposition method.

It is worth noting that our previous study has already showed the trace level (ppt level) of plastic explosives such as dinitrotoluene (DNT) and trinitrotoluene (TNT) utilizing 3D nanostructure assembles.[118] The significant progresses achieved here allowed the significant expansion of the application of 3D SERS templates toward complex chemical compounds such as "invisible" hazardous chemicals.

The novel SERS-active substrates developed here were successfully fabricated with cylindrical porous structures and mixed gold nanorod-nanoparticle clusters by the vacuum infiltration method combined with polymeric glue layers. The 3D SERS-active substrates provide hot spots with a plasmon resonance close to the laser excitation due to the plasmonic resonance coupling effect. Compared to the conventional 1D nanoparticle, nanodisk arrays, 2D nanoislands, and nanohole arrays all reported in literature, the 3D nanostructure assemblies introduced in this study showed strong SERS enhancement due to a much larger surface area, which maximizes hot spots but also the waveguide effect of the porous alumina membranes. With these substrates, trace level of detection of peroxide-based explosives such as HMTD was achieved. These compounds cannot be detected by traditional SERS because of the lack of their Raman active specific chemical functionalities making them practically "invisible" compounds. Raman signal from the photodecomposed fragments of HMTD provided a truly trace level of sensitivity down to a record value of 3 ppm exceeding that of earlier reports by several orders of magnitude. From the SERS intensity comparison of 3D assembled nanostructure with 2D planar nanostructure, 3D SERS-active substrate showed significantly stronger Raman enhancement than conventional 2D planar nanostructure from nanoparticles widely reported in literature.

We have also suggested and implemented an efficient, simple and fast way to assemble nanoparticles into 3D nanostructures by in situ growth of the nanoparticles inside the porous templates that allows to overcome clogging problems normally associated with the traditional vacuum infiltration method. Silver nanoparticles were grown within porous alumina membranes (PAMs) without clogging by taking advantage of uniformly-deposited, nano-sized silver seeds by the electroless deposition method for use as uniformly decorated SERS-active substrate. Comparing to the ordered 2D planar array of silver nanoparticles grown from gold seeds on a block copolymer template which possess a limited concentration of hot spots and some methods require additional plasma etching or other roughening steps, our method allows to assemble silver nanoparticles 3D template maximizing the density of hot spots and optimize the size of the silver nanoparticles by the control over the optimal growth time for largest SERS enhancement.

This study provided a clear understanding of the contribution of LSPR of assembled nanostructures and wavelength of incident light for maximum SERS enhancement, which can be a general guideline to achieve optimal SERS enhancement of each specific analyte (Figure 8.2). Here, we could estimate the necessary location for the plasmon resonance band peak (λ_{LSPR}) of the metallic nanostructures of the SERS substrate based on our experimental results as well as literature values. We analyzed the known suggestion that the λ_{LSPR} needs to be located approximately 1/3 of the distance between the excitation wavelength and the wavelength associated with the Raman peak of the analyte.[71] Thus, we generated a "universal" diagram for gold nanoparticle, silver nanoparticle, and god nanorods system (Figure 8.2). The silver nanoparticles assembled in PAM (λ_{LSPR} =528 nm) showed strong SERS enhancement from R6G molecules because λ_{LSPR} located is between λ_{vib} and λ_{ex}. Although assembled gold nanoparticles and nanorods in PAM showed their λ_{LSPR} at 740 nm,

the resulting SERS enhancement from HMTD molecules is large enough because the plasmon resonance bands still nearly overlap with the λ_{ex} of 785 nm.

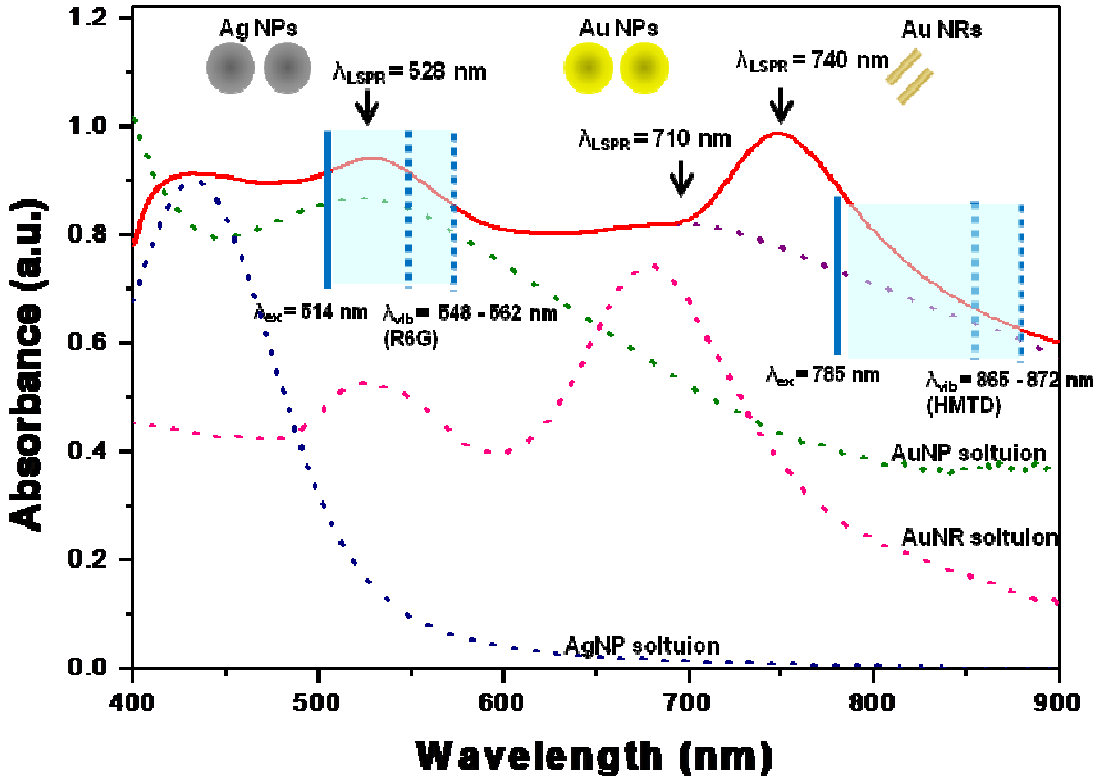

Figure 8.2. Representative UV-vis absorption data showing a shift in the absorbance of the silver, gold nanoparticles, gold nanorods following aggregation in PAMs. The blue lines indicate the spectral range which will allow for the highest intensity SERS spectrum of R6G using a 514 nm laser, HMTD using a 785 nm laser.

Moreover, we conducted the Raman mapping of 3D SERS-active substrates using confocal Raman microscope, which clearly demonstrated that large Raman enhancement occurs along the depth-direction. We also demonstrated an optimal size of nanoparticles in 3D assembly to maximize SERS properties by in situ growth of nanoparticles. We suggested the various polymeric selective coatings for each analyte and their thickness on metal nanostructure for maximum SERS effects. Furthermore, SERS-active substrates fabricated by the in situ electroless growth of silver nanoparticles excluded a polyelectrolyte as a binding layer, which

can be the optimal for SERS sensing applications because it is not necessary to separate the Raman bands of the polyelectrolyte binding layer from those of the desired analyte. By tuning the surface plasmon resonance of the nanostructures which depend on their shape, size, composition, and aggregation, very strongly localized fields can be achieved for the predetermined wavelength of the incident light. All these aspects discussed in this study contributed to the development of our novel design for the 3D SERS-active substrate.

Furthermore, assembly of silver nanowire crossbars structure with polarization dependent SERS phenomenon was introduced in this study. Fabrication of long-range ordered metal nanostructure arrays over large areas up to centimeter scale can be achieved utilizing capillary transfer lithography. A variety of different rotational patterns with different on/off SERS intensities can be designed depending on the exact location and orientation of decorated nanoparticles nearby nanowire crossbars. While the relative Raman intensities of PVP from a central junction of nanowire crossbar were maintained at different polarization directions, the SERS at the junction of nanowires and spherical nanoparticles shows the polarization-dependent characteristics. The stronger Raman enhancement was observed when the polarization direction is parallel to the gap between nanowire and nanoparticle due to the enhanced plasmon coupling of nanowire and nanoparticle. For the higher angular resolution than Raman mapping of the PVP on silver nanowire crossbars, Raman bands of R6G molecules on silver nanowire crossbar structure were monitored. While the modest and random variation of Raman intensities confirms the fact that two crossing nanowires create plasmon coupling conditions that are polarization-independent characteristics, the Raman intensity increased significantly up to 15 times as the polarization direction changes to parallel to the junction between silver nanoparticle and silver nanowire.

Overall, this approach provides means for the fabrication of arrays of SERS hot spots which can be activated only at a certain polarization direction and suppressed at an orthogonal direction while keeping some hot spots activated under any condition. Such addressable polarization-dependent on/off behavior of Raman activity at silver nanowire crossbars with Raman activity at silver nanoparticles controlled by the rotation of the polarization plane which excites transversal plasmon resonances and initiates selective excitation of selected SERS hot spots can be utilized for label-free Raman markers.

As an alternative approach for the template-assisted nanostructure design, PAM can be utilized for the fabrication of the nanotube structure. By integrating noble metal nanoparticles into the organic nanotube, the assembled nanostructure can be utilized for the plasmonic sensing applications. The facile fabrication of responsive polymer and metal nanoparticles hybrid nanostructures were achieved utilizing sacrificial porous template assisted methods. The pH responsive nanotubes composed of PS-P2VP block copolymer and gold nanoparticles exhibit a reversible change in the plasmon resonance position. The ordered phase separation of the block copolymer within the nanotube structure is formed by solvent annealing. In situ formation of gold nanoparticles in the P2VP domains allows decorating the inner and outer shell of the nanotubes. SEM and TEM analysis were conducted to show the uniformly assembled gold nanoparticles in PS-b-P2VP nanotube structures.

Due to the coil to globule transition above pH 3.6 of P2VP domain, the PS-b-P2VP-gold nanoparticles nanotubes show reversible changes in topology, size (up to 25%), and collective plasmon resonance appearance. The morphological changes caused by exposure of PS-b-P2VP nanotubes to the acidic environment resulted in the red shift of the plasmon

resonance of the encapsulated gold nanoparticles because swelling of the P2VP blocks causes the aggregation of the gold nanoparticles at the outer surface increasing the coupling of plasmon resonances, resulting in the red shift. The exposure of nanotubes to neutral solution resulted in the gold nanoparticles rearrangement due to topology recovery resulting in the blue shift of the plasmon peak. It is worth noting that the mechanical integrity of nanotubes is preserved by the glassy PS block upon the significant morphology changes of the PS-b-P2VP nanotubes We suggest that the large surface-to-volume ratio of nanotubes and open through central pore maximizes their interaction with environment, thus enhancing their response to external stimuli which can be extremely beneficial in microfluidics and biosensing.

8.2. Issues to be addressed and Future directions

The development presented in this study establish novel design paradigm for organic/inorganic nanostructure assemblies which can be utilized in plasmonic sensing applications. One of the major future applications of metal nanostructure assembly in 3D porous template could be the microfluidic system because in situ Raman measurement will be available by collecting the spectra from the adsorbed analytes on the substrates while the analytes in solution pass through the porous structure. Therefore, our design facilitates the effort to integrate the 3D porous SERS template into the microfluidic device.

The design of robust and cost-effective organic/inorganic hybrid 3D SERS template can be prospective for the trace-level detection of various liquid or vapor analytes with the simple modification of selective coatings and nanostructures. The method introduced in this study, 3D assembly of nanostructures via in situ nanoparticles growth inside the porous template,

can allow further facile fabrication of seed grown various nanostructures such as nanorods, nanoplates, or nanocubes under physical confinement for advanced SERS applications. The specific growth time under the fabrication conditions will provide optimum nanoparticle densities, level of aggregation of nanoparticles, and plasmon band position for maximum SERS enhancement. For the long-term stability of the PAMs with silver nanoparticles, the ultra thin layer of metal or polymer can be deposited by atomic layer deposition (ALD) or simple spin coating by preventing oxidation of the silver nanoparticles.

Based on 3D SERS template with gold or silver nanostructures, more complex bimetallic nanostructure can be also designed with the advantage utilization of the wide range of the incident laser source of Raman. When the gold nanostructure is integrated with silver nanostructure, UV-vis absorption spectra has been shown broadening of the plasmon band, which can be utilized for optimized resonances with wide range of wavelength of the incident light such as 514, 633, 785 nm lasers (commonly used in Raman studies). Integration silver nanostructure with gold can also improve the stability of the nanostructure which can prevent from the oxidation.

To understand the fundamental issues related to light transmission, absorption, waveguiding behavior, and electromagnetic field distribution of the metal nanostructures decorated on the sidewalls of PAMs, Finite Element Analysis (FEA), Density Functional Theory (DFT) should be employed further. The optical properties of assembled gold nanoparticles, gold nanorods, and silver nanoparticles inside PAM templates can be optimized by using assistance from the electromagnetic RF module of FEA which can be exploited to simulate the 3D distribution of inner electrical field distribution excited by the incident light under different conditions.

The massive fabrication of the addressable crossbar nanostructures can be important for exploiting the multifunctional on/off SERS markers for chemical and biological detection assays. We demonstrated the possibility of the massive fabrication of such junctions with nanowires which might open a path for large-scale assay applications. Although the exact positioning of the silver nanoparticles onto silver nanowires would require to be improved or need the advanced techniques, we suggest that proper design of nanowire-crossbars decorated with nanoparticles might be completed by selective micropatterning as will be a subject of future studies.

The organic/inorganic hybrid nanotube structures possess more possibilities of their interaction with changes in environmental conditions due to the large surface-to-volume ratio and open through pores. Therefore, the response of the nanotube structure to external stimuli can be enhanced and extremely beneficial in microfluidics and biosensing. The broadening material selection of the pH or temperature responsive block copolymer can improve the multifunctional nanotube LSPR sensors.

Overall, this research suggested several different organic/inorganic nanostructure assemblies by various template-assisted techniques for plasmonic-based chemical sensing applications. We have developed 3D nanostructure assembly taking advantage from an efficient bottom-up approach opening the next level of nanostructure assembly. Although topics addressed above need to be progressed further for the development of practical device applications and a fundamental understanding of the phenomena in nano-scale structures, these developed novel nanostructures show promise for designing much improved sensors for real time

monitoring of chemical warfare agents, toxic environmental pollutants, common chemicals, and biomolecules.

References

(1) Burda, C.; Chen, X.; Narayanan, R.; El-Sayed. M. A. *Chem. Rev.* **2005**, *105*, 1025.

(2) Stewart, M. E.; Anderton, C. R.; Thompson, L. B.; Maria, J.; Gray, S. K.; Rogers, J. A.; Nuzzo, R. G. *Chem. Rev.* **2008**, *108*, 494.

(3) Hu, M.; Chen, J.; Li, Z.-Y.; Au, L.; Hartland, G. V.; Li, X.; Marquez, M.; Xia, Y. *Chem. Soc. Rev.* **2006**, 11,1084.

(4) Ly, N.; Foley, K.; Tao, N. *Anal. Chem.* **2007**, *79*, 2546

(5) Homola, J. *Anal. Bioanal. Chem.* **2003**, *337*, 528.

(6) Huang, X.; Neretina, S.; El-Sayed, M. A. *Adv. Mater.* **2009**, *21*, 1.

(7) Kelly, K. L.; Coronado, E.; Zhao, L. L.; Schatz, G. C. *J. Phys. Chem. B* **2003**, *107*, 668.

(8) Ko, H.; Singamaneni, S.; Tsukruk, V. V. *Small* **2008**, *4*, 1576.

(9) Mirkin, C. A. L.; Robert, L.; Mucic, R. C.; Storhoff, J. J. *Nature* **1996**, *382*, 607.

(10) Willets, K. A.; Van Duyne, R. P. *Ann. Re*v. *Phys. Chem.* **2006**, *58*, 267.

(11) McFarland, A. D.; Van Duyne, R. P. *Nano Lett.* **2003**, *3*, 1057.

(12) Svedendahl, M.; Chen, S.; Dmitriev, A.; Ka¨ll, N. *Nano Lett.* **2009**, *9*, 4428.

(13) Jeanmarie, D. L.; Van Duyne, R. P. *J. Electroanal. Chem.* **1977**, *84*, 1.

(14) Nie, S.; Emory, S. R. *Science* **1997**, *275*, 1102.

(15) Raman, C. V.; Krishnan, K. S. *Nature* **1928**, *122*, 169.

(16) Kneipp, K. *Phys. Today* **2007**, *60*, 40.

(17) Campion, A.; Kambhampati, P. *Chem. Soc. Rev.* **1998**, *27*, 241.

(18) Baker, G. A.; Moore, D. S. *Anal. Bioanal. Chem.* **2005**, *382*, 1751.

(19) Singamaneni, S.; LeMieux, M. C.; Jiang, H.; Enlow, J. O.; Bunning, T. J.; Naik, R. R.; Tsukruk, V. V. *Adv. Mater.* **2007**, *19,* 4248.

(20) Alvarez-ros, M. C.; Sanchez-Sortes, S.; Francioso, O.; Garcia-Ramos, J. V. *Can. J. Anal. Sci. Spectrosc.* **2003**, *48*, 132.

(21) Spencer, K. M.; Sylvia, J. M.; Clauson, S. L.; Christensen, S. D. *Proc. SPIE Int. Soc. Opt. Eng.* **2004**, *5268*, 340.

(22) Bao, L.; Mahurin, S. M.; Haire, R. G.; Dai, S. *Anal. Chem.* **2003**, *75*, 6614.

(23) Bertone, J. F.; Cordeiro, K. L.; Sylvia, J. M.; Spencer, K. M. *Proc. SPIE-Int. Soc. Opt. Eng.* **2004**, *5403*, 387.

(24) Kneipp, K.; Wang, Y.; Dasari, R. R.; Feld, M. S.; Gilbert, B. D.; Janni, J.; Steinfeld, J. I. *Spectrochim. Acta A* **1995**, *51*, 2171.

(25) Moskovits, M. *Rev. Mod. Phys.* **1985**, *57*, 783.

(26) Schatz, G. C.; Young, M. A.; Van Duyne, R. P. *Appl. Phys.* **2006**, *103*, 19.

(27) Banholzer, M. J.; Millstone, J. E.; Qin, L. D.; Mirkin, C. A. *Chem. Soc. Rev.* **2008**, *37*, 885.

(28) Jiang, C.; Lio, W. Y.; Tsukruk, V. V. *Phys. Rev. Lett.* **2005**, *95*, 115503-4.

(29) Vo-Dinh, T. *Trends Anal. Chem.* **1998**, *17*, 557.

(30) Chan, S.; Kwon, S.; Koo, T. W.; Lee, L. P.; Berlin, A. A. *Adv. Mater.* **2003**, *15*, 1595.

(31) Williamson, T. L.; Guo, X.; Zukoski, A.; Sood, A.; Diaz, D. J.; Bohn, P. W. *J. Phys. Chem. B* **2005**, *109*, 20186.

(32) Lee, S. J.; Morrill, A. R.; Moskovits, M. *J. Am. Chem. Soc.* **2006**, *128*, 2200.

(33) Schierhorn, M.; Lee, S. J.; Boettcher, S. W.; Stucky, G. D.; Moskovits, M. *Adv. Mater.* **2006**, *18*, 2829.

(34) Duan, G.; Cai, W.; Luo, Y.; Li, Y.; Lei, Y. *Appl. Phys. Lett.* **2006**, *89*, 181918.

(35) Wang, H.-H.; Liu, C.-Y.; Wu, S.-B.; Liu, N.-W.; Peng, C.-Y.; Chan, T.-H.; Hsu, C.-F.; Wang, J.-K.; Wang, Y.-L. *Adv. Mater.* **2006**, *18*, 491.

(36) Saito, M.; Shibasaki, M.; Nakamura, S.; Miyagi, M. *Opt. Lett.* **1994**, *19*, 710.

(37) Lau, K. H. A.; Tan, S.; Tamada, K.; Sander, M.S.; Knoll, W. *J. Phys. Chem. B* **2004**, *108*, 10812.

(38) Garcia-Vidal, F. J.; Pendry, J. B. *Phys. Rev. Lett.* **1996**, 77, 1163.

(39) Amezcua-Correa, A.; Yang, J.; Finlayson, C. E.; Peacock, A. C.; Hayes, J. R.; Sazio, P. J. A.; Baumberg, J. J.; Howdle, S. M. *Adv. Funct. Mater.* **2007**, *17*, 2024.

(40) Han, Y.; Oo, M. K.; Zhu, Y.; Sukhishvili, S.; Xiao, L.; Demohan, M. S.; Jinc, W.; Du, H. *Proc. SPIE* **2007**, *6767*, 67670G.

(41) Velev, O. D.; Tessier, P. M.; Lenhoff, A. M.; Kaler, E. W. *Nature* **1999**, *401*, 548.

(42) Velev, O. D.; Kaler, E. W. *Adv. Mater.* **2000**, *12*, 531.

(43) Quinten, M.; Leitner, A.; Krenn, J. R.; Aussenegg, F. R. *Opt. Lett.* **1998**, *23*, 1331.

(44) Takahara, J.; Yamagishi, S.; Taki, H.; Morimoto, A.; Kobayashi, T. *Opt. Lett.* **1997**, *22*, 475.

(45) Jackson, J. B.; Halas, N. J. *Proc. Natl. Acad. Sci.* **2004**, *101*, 17930.

(46) Yoshida, K.-I.; Itoh, T.; Tamaru, H.; Biju, V.; Ishikawa, M.; Ozaki, Y. *Phys. Rev. B* **2010**, *81*, 115406.

(47) Vo-Dinh, T.; Dhawan, A.; Norton, S. J.; Khoury, C. G.; Wang, H.-N.; Misra, V.; Gerhold, M. D. *J. Phys. Chem. C* **2010**, *114,* 7480.

(48) Xu, H.; Aizpurua, J.; Ka¨ll, M.; Apell, P. *Phy. Rev. E* **2000**, *62*, 4318.

(49) Huschka, R.; Neumann, O.; Barhoumi, A.; Halas, N. J. *Nano Lett.* **2010**, *4*, 6169

(50) Lyvers, D. P.; Moon, J. M.; Kildishev, A. V.; Shalaev, V. M.; Wei, A. *ACS Nano* **2008**, *2*, 2569.

(51) Ko, H.; Tsukruk, V. V. *Small* **2008**, *4*, 1980.

(52) Chang, S.; Combs, Z. A.; Gupta, M.; Davis, R.; Tsukruk, V. V. *ACS Applied Materials and Interfaces* **2010**, in print, am-2010-00758k.

(53) Chang, S.; Ko, H.; Singamaneni, S.; Gunawidjaja, R.; Tsukruk, V. V. *Anal. Chem.*, **2009**, *81*, 5740.

(54) Talley, C. E.; Jackson, J. B.; Oubre, C.; Grady, N. K.; Hollars, C. W.; Lane, S. M.; Huser, T. R.; Nordlander, P.; Halas, N. J. *Nano Lett.* **2005**, *5*, 1569.

(55) Qin, L.; Zou, S.; Xue, C.; Atkinson, A.; Schatz, G. C.; Mirkin, C. A. *Proc. Natl. Acad. Sci. U. S. A.* **2006**, *103*, 13300.

(56) Liu, G. L.; Lu, Y.; Kim, J.; Doll, J. C.; Lee, L. P. *Adv. Mater.* **2005**, *17*, 2683.

(57) Russell, T. P. *Science* **2002**, *297*, 964.

(58) Huber, D. L.; Manginell, R. P.; Samara, M. A.; Kim, B. I.; Bunker, B. C. *Science* **2003**, *301*, 352.

(59) Luzinov, I.; Minko, S.; Tsukruk, V. V. *Prog. Polym. Sci.* **2004**, *29*, 635.

(60) Roiter, Y.; Minko, S. *J. Am. Chem. Soc.* **2005**, 127, 15688.

(61) Wang, L.; Topham, P. D.; Mykhaylyk, O. O.; Howse, J. R.; Bras, W.; Jones, R. A. L.; Ryan, A. J. *Adv. Mater.* **2007**, *19*, 3544.

(62) Tokarev, I.; Tokareva. I.; Minko, S. *Adv. Mater.* **2008**, *20*, 2730.

(63) Xu, H. X.; Xu, J.; Jiang, X.; Zhu, Z.; Rao, J.; Yin, J.; Wu, T.; Liu, H.; Liu, S. *Chem. Mater.* **2007**, *19,* 2489.

(64) Bates, F. S.; Fredrickson, G. H. *Phys. Today* **1999**, *52*, 32.

(65) Bates, F. S. *Science* **1991**, *251*, 898.

(66) Baltá-Calleja, F. J.; Roslaniec, Z. *Block copolymers*, CRC Press, **2000**.

(67) Bates, F. S.; Fredrickson, G. H. *Annu. Rev. Phys. Chem.***1990**, *41*, 525.

(68) Wang, Y.; Gosele, U.; Steinhart, M. *Nano Lett.* **2008**, *8*, 3548.

(69) Canada, M. J. A.; Medina, A. R.; Frank, J.; Lendl, B. *Analyst* **2002**, *127*, 1365.

(70) Spencer, K. M.; Sylvia, J. M.; Janni, J. A.; Klein, J. D. *Proc. of SPIE* **1999**, *3710*, 373.

(71) Haynes, C.L.; Van Duyne, R. P. *J. Phys. Chem. B* **2003**, *107,* 7426

(72) Kwon, K.; Lee, K. Y.; Lee, Y. W.; Kim, M.; Heo, J.; Ahn, S. J.; Han, S. W. *J. Phys. Chem. C* **2007**, *111*, 1161.

(73) Sato-Berrú, R.; Redón, R.; Vázquez-Olmos, A.; Saniger, J. M. *J. Raman Spectrosc.* **2009**, *40*, 376

(74) Gole, A.; Murphy, C. J. *Langmuir* **2008**, *24*, 266.

(75) Lee, K. S.; El-Sayed, M. A. *J. Phys. Chem. B* **2005**, *109,* 20331.

(76) Sun, Y.; Xia, Y. *Adv. Mater.* **2002**, *14*, 833.

(77) Aroca, R. F.; Goulet, P. J. G.; dos Santos, D. S.; Alvarez-Puebla, R. A.; Oliviera (J.r.), O. N. *Anal. Chem.* **2005**, *77*, 378.

(78) Tao, A.; Kim, F.; Hess, C.; Goldberger, J.; He, R.; Sun, Y.; Xia, Y.; Yang, P. *Nano Lett.* **2003**, *3*, 1229.

(79) Kim, Y. H.; Park, J.; Yoo, P. J.; Hammond, P. T. *Adv. Mater.* **2007**, 19, 4426.

(80) Gardiner, D. J. *Practical Raman spectroscopy* Springer-Verlag, 1989, New York.

(81) Singamaneni, S.; Gupta, M.; Yang, R.; Tomczak, M. M.; Naik, R. R.; Wang, Z. L.; Tsukruk, V. V. *ACS Nano* **2009**, *3*, 2593.

(82) Tsukruk, V. V. *Rubber Chem. Techn.* **1997**, *70*, 430.

(83) McConney, M. E.; Singamaneni, S.; Tsukruk, V. V. *Polym. Rev.,* **2010,** *50*, 235.

(84) Cotte-Rodríguez, I.; Chen, H.; Cooks, R. G. *Chem. Commun.* **2006**, *9*, 953.

(85) Widmer, L.; Watson, S.; Scholatter, K.; Crowon, A. *Analyst* **2002**, *127*, 1627.

(86) Zitrin, S.; Kraus S.; Glattstein, B. *Proc. Int. Symp. Anal. Detect. Explos.* **1983**, Quantico, VA, Fed. Bur. Invest., Washington, DC, 137.

(87) Evans, H. K.; Tulleners, F. A. J.; Sanchez B. L.; Rasmussen, C. A. *J. Forensic Sci.* **1986**, *31*, 1119.

(88) White, G. M. *J. Forensic Sci.* **1992**, *37*, 652.

(89) Bannister, W. W.; Chen, C.-C.; Curby, W. A.; Chen, E. B.; Damour, P. L.; Morales, A. US Patent; US 6406918 B1. **2002**.

(90) Schulte-Ladbeck, R.; Kolla, P.; Karst, U. *Anal. Chem.* **2003**, *75*, 731.

(91) Reichardt, C.;Schroeder, J.; Schwarzer, D. P. *Phys. Chem. Chem. Phys.* **2008**, *10*, 5218.

(92) Frost, G. J.; Ellison, G. B.; Vaida, V. *J. Phys. Chem. A* **1999**, *103*, 10169.

(93) Lunak, S.; Sedak, P. *J. Photochem. Photobiol. A: Chem.* **1992**, *68*, 1.

(94) Kuptsov, H.; Zhizhin G. N. *Handbook of Fourier-transform Raman and infrared spectra of polymers A.*, Elesvier 1998 Amsterdam.

(95) Lin-Vien, D.; Colthup, N. B.; Fateley, W. G.; Grasselli, J. G. *The Handbook of Infrared and Raman Characteristic Frequencies of Organic Molecules,* Academic press, INC. 1991 San Diego.

(96) Huang, X.; El-Sayed, I. H.; Qian, W.; El-Sayed, M. A. *Nano Lett.* **2007***, 7*, 1591.

(97) Kozlovskaya, V.; Kharlampieva, E.; Khanal, B. P.; Manna, P.; Zubarev, E. R.; Tsukruk, V. V. *Chem. Mater.* **2008**, *20*, 7474.

(98) Nikoobakht, B.; El-Sayed, M. A. *Chem. Mater.* **2003**, *15*, 1957.

(99) Nikoobakht, B.; El-Sayed, M. A. *J. Phys. Chem. A* **2003**, *107,* 3372.

(100) Xu, J.; Xia, J.; Wang, J.; Shinar, J.; Lin, Z. *Appl. Phys. Lett.* **2006**, *89*, 133110.

(101) Camden, J. P.; Dieringer, J. A.; Wang, Y.; Masiello, D. J.; Marks, L. D.; Schatz, G. C.; R. P. Van Duyne, *J. Am. Chem. Soc.* **2008**, *130*, 12616.

(102) Gunawidjaja, R.; Peleshanko, S.; Ko, H.; Tsukruk, V. V. *Adv. Mater.* **2008**, *20*, 1544.

(103) Sun, Z; Ni, W.; Yang, Z.; Kou, X.; Li, L.; Wang, J. *Small* **2008**, *4*, 1287.

(104) Schaefer, W. P.; Fourkas, J. T.; Tiemann, B. G. *J. Am. Chem. Soc.* **1985**, *107*, 2461.

(105) Pettinger, B.; Domke, K. F.; Zhang, D.; Schuster, R.; Ertl, G. *Phys. Rev. B* **2007**, *76*, 113409.

(106) Thery-Merland, F.; Methivier, C.; Pasquinet, E.; Hairault, L.; Pradier, C. M. *Sensor Actuat. B-Chem* **2006**, *114*, 223.

(107) Hiyoshi, R. I.; Nakamura, J.; Brill, T. B. *Prop. Explos. Pyrotech.* **2007**, *32*, 127.

(108) Peña-Quevedo, A. J.; Mina-Calmide, N.; Rodríguez, N.; Nieves, D.; Cody, R. B.; Hernández-Rivera, S. P. *Proc. of SPIE* **2006**, *6201*, 62012E.

(109) Peña-Quevedo, A. J.; Figueroa, J.; Rodríguez, N.; Nieves, D.; Hernández, N.; Rivera, R.; Mina, N.; Hernández-Rivera, S. P. *Proc. of SPIE* **2006**, *6201*, 62012D.

(110) Cottrell, T. L. *The Strengths of Chemical Bonds*, 2nd ed., Butterworths, 1958, London.

(111) Beltran-Heredia, J.; Torregrosa, J.; Dominguez, J. R.; Peres, J. A. *Ind. Eng. Chem. Res.* **2001**, *40,* 3104.

(112) Ling, P.; Boldyrev, A. I.; Simons, J.; Wight, C. A. *J. Am. Chem. Soc.* **1998**, *120,* 12327.

(113) Song, W.; Ravindran, V.; Pirbazari, M. *Chem. Eng. Sci.* **2008**, *63*, 3249.

(114) Okpalugo, T. I. T.; Papakonstantinou, P.; Murphy, H.; McLaughlin, J.; Brown, N. M. D. *Carbon* **2005**, *43*, 153.

(115) Moulder, J. F.; Stickle, W. F.; Sobol, P. E.; Bomben. K. D.; Ed. Chastain, J. *Handbook of X-ray photoelectron Spectroscopy*, Perkin-Elmer Corporation 1992, Eden Prairie, USA.

(116) Kama, P. V. *J. Phys. Chem. B* **2002**, *106,* 7729.

(117) Iliev, V; Tomova, D.; Bilyarska, L.; Tyuliev, G. *J. Mol. Catal. A: Chem.* **2007**, *263*, 32.

(118) Ko, H.; Chang, S.; Tsukruk, V. V. *ACS Nano* **2008**, *3,* 181.

(119) Dieringer, J. A.; Lettan, R. B., II; Scheidt, K. A.; Van Duyne, R. P. *J. Am. Chem. Soc.* **2007**, *129*, 16249.

(120) Thaxton, C. S.; Elghanian, R.; Thomas, A. D; Stoeva, S. I.; Lee, J. S.; Smith, N .D.; Schaeffer, A. J.; Klocker, H.; Horninger, W.; Bartsch, G.; Mirkin, C. A. *Proc. Natl. Acad. Sci. U.S.A.* **2009**, *106*, 18437.

(121) Lim, D.-K.; Jeon, K.-S.; Kim, H.-M.; Nam, J.-M.; Suh, Y. D. *Nat. Mater.* **2010**, *9*, 60.

(122) Hulteen, J. C.; Treichel, D. A.; Smith, M. T.; Duval, M. L.; Jensen, T. R.; Van Duyne, R. P.; *J. Phys. Chem. B* **1999**, *103*, 3854.

(123) Freeman, R. G.; Grabar, K. C.; Allison, K. J.; Bright, R. M.; Davis, J. A.; Guthrie, A. P.; Hommer, M. B.; Jackson, M. A.; Smith, P. C.; Walter, D. G. *Science **1995***, *267*, 1629.

(124) Wang, Z.; Pan, S.; Krauss, T. D.; Du, H.; Rothberg, L. J. *Proc. Natl. Acad. Sci. USA* **2003**, *100*, 8638.

(125) Gobin, A. M.; Lee, M. H.; Halas, N. J.; James, W. D.; Drezek, R. A.; West, J. L. *Nano Lett.* **2007**, *7*, 1929.

(126) Moskovits, M.; Suh, J. S. *J. Phys. Chem.* **1984**, *88*, 5526.

(127) Gunawidjaja, R.; Kharlampieva, E.; Choi, I.; Tsukruk, V. V. *Small* **2009**, *5*, 2460.

(128) Xu, P.; Mack, N. H.; Jeon, S.-H.; Doorn, S. K.; Han, X.; Wang, H. L. *Langmuir* **2010**, *26*, 8882.

(129) Xu, P.; Zhang, B.; Mack, N. H.; Doorn, S. K.; Han, X.; Wang, H. L. *J. Mater. Chem*., **2010**, 20, 7222.

(130) Driskell, J. D.; Shanmukh, S.; Liu, Y.; Chaney, S. B.; Tang, X.-J.; Zhao, Y.-P.; Dluhy, R. A. *J. Phys. Chem. C*, **2008**, *112*, 895.

(131) Han, Y.; Tan, S.; Pristinski, D.; Sukhishvili, S.; Du, H. *Adv. Mater.* **2010**, *22*, 2647.

(132) Velev, O. D.; Tessier, P. M.; Lenhoff, A. M.; Kaler, E. W. *Nature* **1999**, *401*, 548.

(133) Sundaramurthy, A.; Crozier, K. B.; Kino, G. S.; Fromm, D. P.; Schuck, P. J.; Moerner, W. E. *Phys. Rev. B* **2005**, *72*, 165409.

(134) Sweatlock, L. A.; Maier, S. A.; Atwater, H. A.; Penninkhof, J. J.; Polman, A. *Phys. Rev. B* **2005**, *71*, 235408.

(135) Zhao, J.; Pinchuk, A. O.; McMahon, J. M.; Li, S.; Ausman, L. K.; Atkinson, A. L. *Acc. Chem. Res. Phys.* **2008**, *41*, 1710.

(136) Sánchez-Iglesias, A.; Aldeanueva-Potel, P.; Ni, W.; Pérez-Juste, J.; Pastoriza-Santos, I.; Alvarez-Puebla, R. A.; Mbenkum, B. N.; Liz-Marzán, L. M. *Nano today* **2010**, *5*, 21.

(137) Qiu, T.; Zhang, W.; Lang, X.; Zhou, Y.; Cui, T.; Chu, P. K. *Small* **2009**, *5*, 2333.

(138) Lee, W.; Scholz,R.; Nielsch, K.; Gosele, U. *Angew. Chem. Int. Ed.* **2005**, *44*, 6050.

(139) Jana, N. R.; Gearheart, L.; Murphy, C. J. *Chem. Commun.* **2001**, *7*, 617.

(140) Finney, E. E.; Finke, R. G. *J. Colloid. Interf. Sci.* **2008**, *317*, 351.

(141) Cao, G. *Nanostructures and Nanomaterials: Synthesis, Properties, and Applications,* Imperial College Press, **2004**.

(142) Moskovits, M.; DiLella, D. P.; Maynard, K. *Langmuir* **1988**, *4*, 67.

(143) Jain, P.K.; El-Sayed, M. A. *Nano Lett.* **2007**, *7*, 2854.

(144) Rechberger, W.; Hohenau, A.; Leitner, A.; Krenn, J. R.; Lamprecht, B.; Aussenegg, F. R. *Opt. Commun.* **2003**, *220*, 137.

(145) Jain, P. K.; Huang, W.; El-Sayed, M. A. *Nano Lett.* **2007**, *7*, 2080.

(146) Hildebrandt, P.; Stockburger, M. *J. Phys. Chem.* **1984**, *88*, 5935

(147) Watanabe, H.: Hayazawa, N.; Inouye, Y.; Kawata, S. *J. Phys. Chem. B* **2005**, *109,* 5012

(148) Sant'Ana, A. C.; Alves, W. A.; Santos, R. H. A.; Ferreira, A. M. D.; Temperini, Marcia L. A. *Polyhedron* **2003**, *22*, 1673.

(149) Gu, B.; Ruan, C.; Wang, W. *Appl. Spectrosc.* **2009**, *63*, 98.

(150) Yoon, I.;Kang, T.; Choi, W.; Kim, J.; Yoo, Y.; Joo, S.-W.; Park, Q.-H.; Ihee, H.; Kim, B. *J. Am. Chem. Soc.* **2009**, *131*, 758.

(151) Mahmoud, M. A.; Tabor, C. E.; El-Sayed, M. A. *J. Phys. Chem. C* **2009**, *113*, 5493.

(152) Chen, X.; Jeon, Y.-M.; Jang, J.-W.; Qin, L.; Huo, F.; Wei, W.; Mirkin, C. A. *J. Am. Chem. Soc.* **2008**, *130*, 8166.

(153) Kang, T.; Yoo, S. M.; Yoon, I.; Lee, S. Y.; Kim B. *Nano Lett.* **2010**, *10*, 1189.

(154) Kang, T.; Yoon, I.; Kim, J.; Ihee, H.; Kim, B. *Chem. Eur. J.* **2010**, *16*, 1351.

(155) Yoon, H. P.; Maitani, M. M.; Cabarcos, O. M.; Cai, L.; Mayer, T. S.; Allara, D. L. *Nano Lett.* **2010**, *10*, 2897.

(156) Cheng, C.; Yan, B.; Wong, S. M.; Li, X.; Zhou, W.; Yu, T.; Shen, Z.; Yu, H.; Fan, H. J. *ACS Applied Materials and Interfaces* **2010**, *2*, 1824.

(157) Qi, H.; Alexson, D.; Glembocki, O.; Prokes, S. M. *Nanotechnology* **2010**, *21*, 215706.

(158) Lee, S. J.; Baik, J. M.; Moskovits, M. *Nano Lett.* **2008**, *8*, 3244.

(159) Ko, H.; Jiang, C.; Tsukruk, V. V. *Chem. Mater.* **2005**, *17*, 5489

(160) Weintraub, B; Chang, S.; Singamaneni, S.; Han, W. H.; Choi, Y. J.; Bae, J.; Kirkham, M.; Tsukruk, V. V.; Deng, Y. *Nanotechnology,* **2008**, *19*, 435302.

(161) Sun, Y. G.; Gates, B.; Mayers, B.; Xia, Y. *Nano Lett.* **2002**, *2*, 165.

(162) Gunawidjaja, R.; Jiang, C.; Peleshanko, S.; Ornatska, M.; Singamaneni, S.; Tsukruk, V. V. *Adv. Funct. Mater.* **2006**, *16*, 2024.

(163) Fang, Y.; Wei, H.; Hao, F.; Nordlander, P.; Xu, H. *Nano Lett.* **2009**, *9*, 2049.

(164) Hutchison, J. A.; Centeno, S. P.; Odaka, H.; Fukumura, H.; Hofkens, J.; Uji-I, H. *Nano Lett.* **2009**, *9*, 995.

(165) Wei, H.; Hao, F.; Huang, Y.; Wang, W.; Nordlander; Xu, H. *Nano Lett.* **2008**, *8*, 2497.

(166) Jiang, C.; Tsukruk, V. V. *Soft Matter.* **2005**, *1*, 334.

(167) Gole, A.; Murphy, C. J. *Langmuir* **2005**, *21*,10756.

(168) Gao, Y.; Jiang, P.; Liu, D. F.; Yuan, H. J.; Yan, X. Q.; Zhou, Z. P.; Wang, J. X.; Song, L.; Liu, L. F.; Zhou, W. Y.; Wang, G.; Wang, C. Y.; Xie, S. S.; Zhang, J. M.; Shen, D. Y. *J. Phys. Chem. B*, **2004**, *108*, 12877.

(169) Ko, H.; Tsukruk, V. V. *Nano Lett.* **2006**, *6*, 1443.

(170) Borodko, Y.; Habas, S. E.; Koebel, M.; Yang, P.; Frei, H.; Somorjai, G. A. *J. Phys. Chem. B* **2006**, *110*, 23052.

(171) Ferrari, A. C.; Robertson, *J. Phys. Rev. B* **2000**, *61*, 14095.

(172) Schwan, J.; Ulich, S.; Batori, V.; Ehrhardt, H.; Silva, S. R. P. *J. Appl. Phys.* **1996**, *80*, 440.

(173) Ferrari, A. C.; Robertson, *J. Phil. Trans. R.Soc. Lond. A* **2004**, *362*, 2477.

(174) Aroca, R. Surface-Enhanced Vibrational Speoctroscopy John Wiley & Sons, Chischester, **2006**.

(175) Tran, M. L.; Centeno, S. P.; Hutchison, J. A.; Engelkamp, H.; Liang, D.; Tendeloo, G. V.; Sels, B. F.; Hofkens, J.; Uji-I, H. *J. Am. Chem. Soc.* **2008**, *130*, 17240.

(176) Kriha, O.; Zhao, L.; Pippel, E.; Gösele, U.; Wehrspohn, R. B.; Wendorff, J. H.; Steinhart, M.; Greiner, A. *Adv. Funct. Mater.* **2007**, *17*, 1327.

(177) Gao, Y.; Li, X.; Gong, J.; Fan, B.; Su, Z.; Qu, L. *J. Phys. Chem. C* **2008**, *112*, 8215.

(178) Briseno, A. L.; Mannsfeld, S. C. B.; Lu, X.; Xiong, Y.; Jenekhe, S. A.; Bao, Z.; Xia, Y. *Nano Lett.* **2007**, *7*, 668.

(179) Sofos, M.; Goldberger, J.; Stone, D. A.; Allen, J. E.; Ma, Q.; Herman, D. J.; Tsai, W.-W.; Lauhon, L . J.; Stupp, S. I. *Nat. Mater.* **2008**, *8*, 68.

(180) Martin, C. R. *Science* **1994**, *266*, 1961.

(181) Wang, Z.; Medforth, C. J.; Shelnutt, J. A. *J. Am. Chem. Soc.* **2004**, *126*, 15954.

(182) Song, T.; Zhang, Y.; Zhou, T.; Lim, C. T.; Ramakrishna, S.; Liu, B. *Chem. Phys. Lett.* **2005**, *415*, 317.

(183) Steinhart, M.; Wendorff, J. H.; Greiner, A.; Wehrspohn, R. B.; Nielsch, K.; Schilling, J.; Choi, J.; Gösele, U. *Science* **2002**, *296*, 1997.

(184) Lu, Q.; Gao, F.; Komarneni, S. Mallouk, T. E. *J. Am. Chem. Soc.* **2004**, *126*, 8650.

(185) Martin, J.; Mijangos, C. *Langmuir* **2009**, *25*, 1181.

(186) Lee, S.; Muller, A. M.; Al-Kaysi, R.; Bardeen, C. J. *Nano Lett.* **2006**, *6*, 1420.

(187) Zhang. M.; Dobriyal, P.; Chen, J.-T.; Russell, T. P.; Olmo, J.; Merry, A. *Nano Lett.* **2006**, *6*, 1075.

(188) Xiang, H.; Shin, K.; Kim, T.; Moon, S.; McCarthy, T. J.; Russell, T. P. *Macromolecules* **2004**, *37*, 5660.

(189) Kim. S. H.; Misner, M. J.; Russell, T. P. *Adv. Mater.* **2008**, *20*, 4851.

(190) Kim, S. H.; Misner, M. J.; Xu, T.; Kimura, M.; Russell, T. P. *Adv. Mater.* **2004**, *16*, 226.

(191) Mansky, P.; Liu, Y.; Huang, E.; Russell, T. P.; Hawker, C. *Science* **1997**, *275*, 1458.

(192) Son, J. G.; Bulliard, X.; Kang, H.; Nealey, P. F.; Char, K. *Adv. Mater.* **2008**, *20*, 3643.

(193) Antonietti, M.; Wenz, E.; Bronstein, L.; Seregina, M. *Adv. Mater.* **1995**, *7*, 1000.

(194) Spatz, J. P.; Mo¨ssmer, S.; Hartmann, C.; Mo¨ller, M.; Herzog, T.; Krieger, M.; Boyen, H.-G.; Ziemann, P.; Kabius, B. *Langmuir*, **2000**, *16*, 407.

(195) Glass, R.; Möller, M.; Spatz, J. P. *Nanotechnology* **2003**, *14*, 1153.

(196) Fernndez-Nieves, A.; Fernndez-Barbero, A.; Vincent, B.; de las Nieves, F. J. *Macromolecules* **2000**, *33*, 2114.

(197) Jiang, C.; Markutsya, S.; Tsukruk, V. V. *Langmuir* **2004**, *20,* 882.

(198) McFarland, A. D. ; Young, M. A. ; Dieringer, J. A. ; Van Duyne, R. P. *J. Phys. Chem. B* **2005**, *109*, 11279.

(199) Jackson, J. B.; Halas, N. J. *Proc. Natl. Acad. Sci. USA* **2004**, *101*, 17930.

(200) Wang, J.; Yang, L.; Boriskina, S.; Yan, B.; Reinhard, B. M. *Anal. Chem.***2011**, DOI: 10.1021/ac103123r

Sehoon Chang's Publications and Conference Presentations

Relevant current refereed publications

1. **Chang, S.**; Ko, H.; Gunawidjaja, R.; Tsukruk, V. V. Addressable Raman Markers from Silver Nanowire Crossbars, *J. Phys. Chem. C.* **2011**, DOI: 10.1021/la104787w.
2. **Chang, S.**; Combs, Z. A.; Gupta, M. K.; Davis, R.; Tsukruk, V. V. Controlled 3D Assembly of Silver Nanoparticle Array via In Situ Growth from Electroless Deposited Seed for Surface-Enhanced Raman Scattering, *ACS Appl. Mater. and Interfaces* **2010**, *2*, 3333-3339.
3. **Chang, S.**; Singamaneni, S.; Kharlampieva, E.; Young, S. L.; Tsukruk, V. V. Responsive Hybrid Nanotubes composed of Block Copolymer and Gold Nanoparticles, *Macromolecules* **2009**, *42*, 5781-5785. *(Cover story)*

4. **Chang, S.**; Ko, H.; Singamaneni, S.; Gunawijaja, R.; Tsukruk, V. V. Hybrid Nanoporous Template for Trace Level SERS Detection of Peroxide-based Explosive, *Anal. Chem.* **2009**, *81*, 5740-5748. *(Highlighted at ACS web page)*
5. Ko, H.; **Chang, S.**; Tsukruk, V. V. Molecular Level SERS Detection of Non-resonant Organic Molecules, *ACS Nano* **2009**, *3*, 181-188.

The other related publications

1. Gupta, M. K.; **Chang, S.**; Singamaneni, S.; Drummy, L. F.; Gunawidjaja, R.; Naik R. R.; Tsukruk, V. V. pH Triggered SERS via Modulated Plasmonic Coupling in Individual Bimetallic Nanocobs, *Small* **2011**, in print.

2. Combs, Z. A.; **Chang, S.**; Clark, T.; Singamaneni, S.; Anderson, K. D.; Tsukruk, V. V. Label-free Raman mapping of surface distribution of protein A and IgG biomolecules, *Langmuir* **2011**, *27*, 3198-3205.
3. Singamaneni, S.; Bertoldi, K.; **Chang, S.**; Jang, J.-H.; Thomas, E. L.; Boyce, M.; Tsukruk, V. V. Instabilities and Pattern Transformation in Periodic, Porous Elastoplastic Solid Coatings, *ACS Appl. Mater. and Interfaces* **2009**, *1*, 42-47.
4. Kozlovskaya, V.; Kharlampieva, E.; **Chang, S.**; Mulhbauer, R.; Tsukruk, V. V. pH-Responsive Layered Hydrogel Microcapsules as Gold Nanoreactors, *Chem. Mater.* **2009**, *21*, 2158-2167.
5. Singamaneni, S.; Bertoldi, K.; **Chang, S.**; Jang, J.-H.; Thomas, E. L.; Boyce, M.; Tsukruk, V. V. Bifurcated Mechanical Behavior of Deformed Periodic Porous Solids, *Adv. Funct. Mater.* **2009**, *19*, 1426-1436.
6. Singamaneni, S.; **Chang, S.**; Jang, J.-H.; Davis, W.; Thomas, E. L.; Tsukruk, V. V. Mechanical Properties of 2D and 3D Polymer Microstructures Fabricated by Interference Lithography, *Phys. Chem. Chem. Phys.* **2008**, *10*, 4093-4105. *(Cover story)*

7. Weintraub, B.; **Chang, S.**; Singamaneni, S.; Han, W. H.; Choi, Y. J.; Bae, J.; Kirkham, M.; Tsukruk, V. V.; Deng, Y. Density-Controlled, Solution-Based Growth of ZnO Nanorod Arrays for Enhanced Field Emission, *Nanotechnology* **2008**, *19*, 435302-1-6.

Conference Presentations

1. **Chang, S.**, Combs, Z. A., Gupta, M. K., Davis, R., Tsukruk, V. V. In Situ Growth of Silver Nanoparticles in Porous Membranes for Surface-Enhanced Raman Scattering, **2011** Material Research Society Spring Meeting, San Francisco *(Poster presentation)*
2. **Chang, S.**, Combs, Z. A., Kodiyath, R., Tsukruk, V. V. 3D Porous Substrates for Label-free SERS Detection of Hazardous Chemical Analytes, **2011** Georgia Tech Research and Innovation Conference, Atlanta *(Poster presentation)*
3. **Chang, S.**; Singamaneni, S.; Ko, H.; Tsukruk, V. V. Nanoporous Substrate with Mixed Nanoclusters for Surface Enhanced Raman Scattering, **2010** Material Research Society Spring Meeting, San Francisco *(Oral presentation)*
4. **Chang, S.**; Singamaneni, S.; Kharlampieva, E.; Young, S. L.; Tsukruk, V. V. Responsive Hybrid Nanotubes Composed of Block Copolymer and Gold Nanoparticles, **2010** Material Research Society Spring Meeting, San Francisco *(Oral presentation)*
5. **Chang**, **S.**, Singamaneni, S., Ko, H., Tsukruk, V. V. Nanoporous Substrate with Mixed Nanoclusters for Surface Enhanced Raman Scattering, **2010** Georgia Tech Research and Innovation Conference, Atlanta *(Poster presentation)*
6. **Chang, S.**; Ko, H.; Singamaneni, S.; Gunawijaja, R.; Tsukruk, V. V. Hybrid Nanoporous Structure with Gold Nanoparticles and Nanorod for Surface Enhanced Raman Scattering, **2009** American Physics Society March Meeting, Pittsburgh *(Oral presentation)*
7. **Chang, S.**; Singamaneni, S.; Kharlampieva, E.; Young, S. L.; Tsukruk, V. V. Responsive Block Copolymer and Gold Nanoparticles Hybrid Nanotubes, **2009** American Physics Society March Meeting, Pittsburgh *(Poster presentation)*
8. **Chang**, **S.;** Singamaneni, S.; Tsukruk, V. V. Responsive Block Copolymer and Gold Nanoparticles Hybrid Nanotubes, **2009** Materials Science and Engineering Graduate Research Symposium, Georgia Tech., *(Oral presentation, 2nd place awarded)*
9. **Chang, S.**; Singamaneni, S.; McConney, M. E.; LeMieux, M. C.; Jiang, H.; Enlow, J. O.; Naik, R. R.; Bunning, T. J.; Tsukruk, V. V. Ultra thin plasma polymer as novel material platform for sensor coatings, **2007** Nano Materials for Defense Applications Symposium, San Diego *(Poster presentation)*

VITA

SEHOON CHANG

Sehoon Chang was born in Seoul, South Korea on April 28, 1980 to Hun Chang and Kyongok Moon. He and his brother, Junghoon Chang, grew up in Apgujungdong, Gangnamgu. He attended Apgujung elementary school, Sinsa middle school, and Hyundai high school. He received a Bachelor of Science in Chemical Engineering from Hanyang University in 2006. He served in the military as a Korean Augmentation Troops to the United States Army (KATUSA) soldier. He was an exchange student in Chemical Engineering at the University of Texas, Austin from fall 2005 to spring 2006. He pursued a Ph.D. in Materials Science and Engineering at Georgia Institute of Technology under the guidance of Prof. Vladimir V. Tsukruk. Kyeore Lee (daughter of Hwanghoon Lee and Sookhee Han) and Sehoon Chang were married on January 7, 2011 in Seoul. After graduation, Sehoon will be a Postdoctoral Associate in the Department of Materials Science and Engineering at Massachusetts Institute of Technology.